Metamaterials for Acoustic Sensing

by

Chu Ma

Submitted to the Department of Mechanical Engineering
in partial fulfillment of the requirements for the degree of

Doctor of Philosophy

at the

MASSACHUSETTS INSTITUTE OF TECHNOLOGY

June 2019

© Massachusetts Institute of Technology 2019. All rights reserved.

Signature redacted

Author .....
Department of Mechanical Engineering
May 17, 2019

Signature redacted

Certified by .....
Nicholas X. Fang
Professor
Thesis Supervisor

Signature redacted

Accepted by .....
Nicolas Hadjiconstantinou
Professor

MASSACHUSETTS INSTITUTE OF TECHNOLOGY
JUN 13 2019
LIBRARIES

ARCHIVES

Metamaterials for Acoustic Sensing

by

Chu Ma

Submitted to the Department of Mechanical Engineering
on May 17, 2019, in partial fulfillment of the
requirements for the degree of
Doctor of Philosophy

Abstract

Acoustic sensing has played an important role in engineering and daily life, especially in biomedical imaging and in the recently developed field of the Internet of Things. Acoustic metamaterials are man-made materials composed of subwavelength unit cells, and can be viewed as macroscopically homogenized media with effective material properties non-existing in nature. Acoustic metamaterials provide new opportunities for solving the challenges in acoustic sensing. This thesis is about exploring new acoustic metamaterials and their applications in acoustic sensing.

The first part of the thesis is about new acoustic metamaterials. In this part, two types of phase shifters are designed. When the frequency of the incident wave changes, one type of them has constant time delay and the other has constant phase shift. New acoustic metasurfaces are designed based on the phase shifters, including acoustic binary phase grating that can realize highly efficient wave steering with much less complex structure compared to previous metasurfaces, and acoustic flat lenses with different steering angles and focusing locations for waves having different frequencies. Besides the phase shifters for phase modulation, tunable amplitude modulation is also proposed and experimentally demonstrated by creating 1D channels in a hydrogel sheet. When the channels are filled with different materials and with different filling ratios, the acoustic properties can be tuned by orders of magnitudes over broad frequency ranges.

The second part of the thesis is about new acoustic sensing methods and systems. First, an acoustic imaging system that can expand the evanescent wave travel distance and improve imaging resolution in far-field is proposed based on the binary phase gratings and additional filter layers. Subwavelength imaging and edge detection for 1D slit objects is demonstrated experimentally with 3D printed prototypes. Second, a system that can select the direction of acoustic transmission is designed and experimentally demonstrated based on the combination of two acoustic binary phase gratings. The double-grating structure is shown to select the direction and the frequency at the same time. By stacking multiple double-grating structures that are configured for different frequencies, the system for broadband direction selection is proposed.

Thesis Supervisor: Nicholas X. Fang
Title: Professor

Acknowledgments

I would like to thank Prof. Fang for his guidance and unwavering support all the way through my PhD. He is the one who inspired me with research ideas, guided me though difficulties, and encouraged and helped me in every step towards academia.

I would like to thank Prof. George Barbastathis, and Prof. Xuanhe Zhao. Their research expertise helped expand my research to broader scopes. I am grateful for their support and suggestions during my thesis committee meetings and thesis preparation.

I would like to thank group members in Prof. Fang's group, Dr. Seok Kim, Dr. Shahrzad Ghaffari Mosanenzadeh, Zheng Jie Tan, Xinhao Li, Huifeng Du, Turga Ganapathy, Dr. Ali Ramazani, Dr. Jun Xu, Dr. Bin Zheng, Dr. Chang Liu, Ms. Chevalley Duhart, and many others, for tremendous help in experiments, for our fruitful discussion of research, for helping me rehearse my talks, and many other things during those six years.

I would like to thank collaborators in Prof. Xuanhe Zhao's group. I learned a lot from each of them in a new field of research. They all offered great help during our collaboration.

I would like to thank all the staff members at MIT for making MIT such a wonderful place to work and live.

I would like to thank my family and friends. Thank my parents for their understanding of me being so far away from them and their support whenever I need it. Thank my friends for the meals and parties we had together. Many of us will attend commencement together, which will be another great memory.

Special thanks to my husband, for being many roles in my life: husband, friend, mentor, photographer, driver, chef, and so on. I want to thank him for his unconditional support for me, and I am looking forward to our journey together in the future.

I also want to thank the funding sources for research: MURI ONR, MITEI/ExxonMobil, and KAUST.

Contents

List of Figures

List of Tables

Chapter 1

Introduction

1.1 Background and motivation

Humans have developed various sensors and sensing technologies to greatly expand our bio capabilities to interact with the environment. For example the microscopes, telescopes, radars, sonars, etc. The length scale of interest ranges from as small as molecules and cells to as large as the planet and the universe. Among all the sensing technologies, acoustic sensing has played an unique and important role.

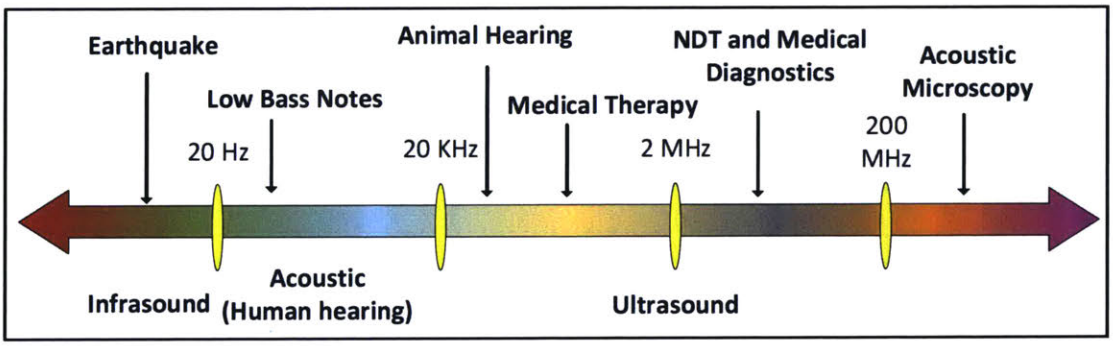

Figure 1-1: Frequency ranges and applications of acoustic wave.

Acoustic wave propagates through the mechanical vibration of particles/structures, and can propagate into structures without cutting and breaking, so the acoustic sensing technologies are usually non invasive and non radiative [2]. The frequency of

acoustic wave ranges from below 20Hz to above 200MHz. Each frequency range corresponds to an important area of application (Fig. 1-1). The infrasound range is used to detect and predict the earthquakes. The human hearing range is from 20Hz to 20KHz, this range is mainly explored by audio industry. Ultrasound range above 20KHz is mainly used by medical diagnosis and therapy and nondestructive testing. The ultrahigh ranges above 200MHz are applied to acoustic microscopy.

Particularly, ultrasound is one of the most important diagnostic imaging methods, allowing non-invasive, non-radiative and real-time imaging with resolutions in sub-millimeter range [3, 4, 5, 6]. Ultrasound has also demonstrated great potential in manipulating cells remotely [7, 8] or destroying tissues [9, 10] in a non-invasive manner, which will lead to breakthroughs in the fields of tumor treatment [11], drug delivery [12], excitation of neurons [13], etc. Besides biomedical field, acoustic sensors can support the rapid development of the Internet of Things with non-contact and non-destructive sensing and diagnosis [14]. Comparing to conventional electronic and mechanic sensors, acoustic sensors have great advantages in overcoming environmental obstacles, integration with human speaking and hearing capabilities, low cost of deployment, and so on. On top of those advantages, acoustic wave is the only effective option for wireless sensing and communications in deep ocean [15]. Thus, acoustics will be critical for the Internet of Things development both on-land and under water.

A typical setup for acoustic sensing system is shown in Fig. 1-2.The system tries to image the scattering objects inside the background matrix (bio tissue or other structures). An acoustic probe generates incident wave and collects reflected wave. The incident wave will propagate into the structure and get reflected when meeting scattering objects. The image of the scattering objects can be reconstructed from the reflected waves.

As a field of long history and high importance, there are still various challenges that need to be addressed in acoustic sensing. Due to the relatively low working frequency range compared with other imaging or sensing techniques, the imaging resolution and information bandwidth of acoustic techniques are limited. The distortion of acoustic beams at interfaces of various media and the absorption during propaga-

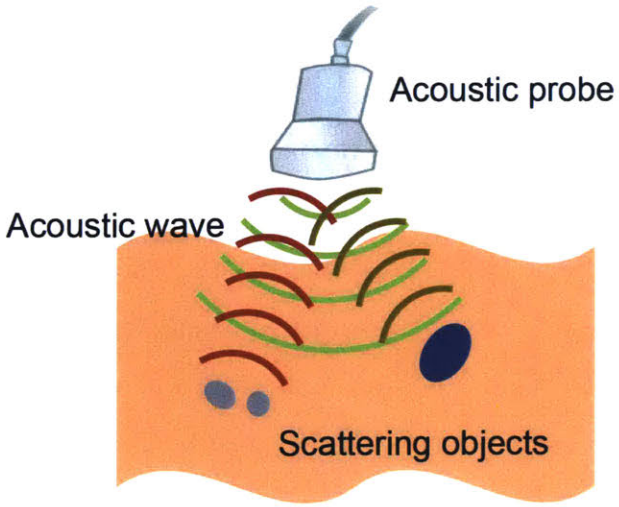

Figure 1-2: A typical setup for acoustic sensing system.

tion will introduce signal overlapping and reduce the signal to noise ratio, making it more complicated to recover the original image or information computationally from the measured data. The reflection of signals from different directions may also overlap with each other and cause the decrease of signal to noise ratio. In a sensor-rich environment, information security and privacy would be another issue. Furthermore, the currently existing synthesized materials used for acoustic techniques have the disadvantages of limited bandwidth, large energy dissipation, difficulty in real-time manipulation, high fabrication complexity and cost, and so on.

Over the last three decades, the emergence of acoustic metamaterials has provided us with new, powerful materials to solve the existing challenges in acoustic sensing, as well as to enable various novel effects, such as subwavelength imaging, negative refraction, invisible cloaking and one-way sound transport [16, 17, 18, 19, 20]. Metamaterials are formed by unit cells with deep subwavelength sizes. Macroscopically, the metamaterials can be viewed as homogenized materials with exotic properties that do not exist in nature. The first acoustic metamaterials is designed in year 2000 [21]. It is composed of locally resonant building blocks formed by solid spheres coated with soft silicone rubber. The building blocks are then embedded in a hard

matrix material. In a spring-mass model [21, 22] developed for the coated spheres, the solid sphere acts like the mass, and the soft silicone rubber acts like a spring that allows relative motions between the mass and the rigid matrix. Near the resonance frequency, the dynamic mass density ρ of the block turn negative. The refractive index n of a material can be expressed as $n^2 = \rho/\kappa$, where κ is the bulk modulus. If ρ becomes negative, then n will be complex. The imaginary part of n induces loss for wave propagation. The system will have bandgap because of the loss near the resonance frequency. This is the first demonstration of exotic acoustic material properties with acoustic metamaterials. Later, negative mass density is also realized by decorated membrane resonators [23, 24]. The negative bulk modulus is realized with soft rubber spheres suspended in water [25], subwavelength Helmholtz resonator arrays [26], or an array of side openings on a tube [23]. Negative index materials are materials that demonstrate both negative density and negative bulk modulus at the same time, which can be constructed by a waveguide with an array of membranes inside the channels and side openings [27], soft rubber spheres suspended in water [28], coupled decorated membrane resonators [29], or space-coilling structures [30].

Acoustic metamaterials are the basis for achieving various novel functionalities, such as phase/amplitude engineering and acoustic metasurfaces [31, 32, 33, 34, 35, 36, 37], super-resolution imaging [38, 39, 40, 41, 42, 43, 44, 45, 46, 47, 48, 49, 50], impedance matching [51, 52, 53], transformation acoustics and invisibility cloaking [54, 55], sound absorption [34, 56, 57, 58], as well as parity-time symmetry metamaterials that extend the parameter values to complex domain [59, 60, 61] in order to realize functions such as uni-directional transparency, nonreciprocal propagation, and so on.

According to Huygens-Fresnel principal [62], each point on a wavefront acts as a source for the wave distribution beyond the wavefront. By designing the phase/amplitude distribution at the emitting plane, arbitrary field distribution in space can be realized. Before the emergence of acoustic metamaterials, phase/amplitude engineering is achieved by dynamically modulated acoustic transducer arrays, and applied to generating complex acoustic beams such as self-bending beams with arbitrary tra-

jectory [63], acoustic vortex beams for improving underwater communication data rate [64], potential distribution for trapping and levitation of particles [65]. The large number of transducers and the complex electronic circuits for controlling the transducers limit the broader applications of the phase/amplitude modulation. Acoustic metasurfaces [31, 32, 33, 34, 35, 36, 37] are proposed to solve this problem. They are composed of passive phase and amplitude modulators with subwavelength thicknesses. Each unit cell on the metasurface is designed to generate a phase shift or amplitude modulation. Different unit cells are then arranged in a 2D plane to generate the designed phase or amplitude gradient. Researchers developed different ways to realize phase and/or amplitude modulation. For example, the coiled waveguide channels can generate larger phase delay compared to the straight channels with the same thickness [33, 66]. By changing the length of the channels, the phase delay can be tuned to cover the range of 0 to 2π. Another hybrid structure composed with a straight channel and Helmholtz resonator side branches is proposed to generate designed phase shift [67, 68]. In the mentioned two metasurface realizations, only the phase is modulated. Later, the independent modulation of phase and amplitude is achieved with lossy acoustic metasurfaces [69]. Bianisotropy is also added to metasurface unit cells to realize scattering-free manipulation of acoustic wavefronts [70]. The different types of acoustic metasurfaces are applied to the construction of anomalous reflection and refraction that obey the generalized Snell's law [32, 33, 71], self-bending beams and vortex beams [67, 68], holograms [69, 72, 73] and so on.

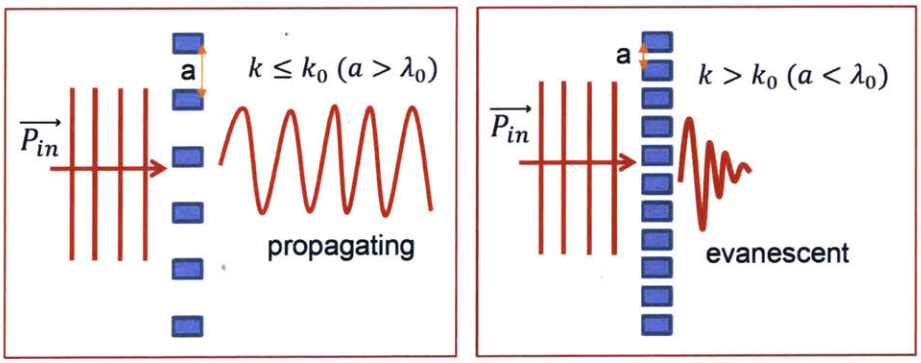

Figure 1-3: Illustration for diffraction limit.

Similar to other imaging techniques, acoustic imaging also suffers from the diffraction limit [74]. The high spatial frequency information will decay as leaving the object, thus cannot be detected by a detector at far-field. As shown in Fig. 1-3, assume we have an object that is periodic with period a. Large a means low resolution, and small a means high resolution. Acoustic wave is incident on the object and gets scattered. The incident wave is $P_{in} = P_0 e^{j(\vec{k_0}\cdot\vec{r}+\omega t+\phi)}$, where $k_0^2 = (2\pi/a)^2 + \gamma^2$, and γ is the wave vector in the wave propagation direction. If the period of the object is larger than wavelength λ of the incident wave, then the scattered wave is propagating wave and can be captured by detector at distance away. If the period is smaller than wavelength, the scattered wave is evanescent and will decay as it leaves the object. A detector at distance away won't be able to capture those evanescent wave that carries the higher spatial resolution information. As a result, in diffraction limited imaging systems, we will obtain blurred images with only the low spatial resolution information.

In order to overcome diffraction limit, the evanescent waves needs to be collected by the detector before they are decayed. The near-field scanning technique [75] is one of the earliest techniques for acoustic subwavelength imaging. Measurements have to be made in close proximity (fractions of wavelength) to objects in order to capture the evanescent components. This greatly limits its application. In the past decade, acoustic metamaterial based lenses have demonstrated the potential in subwavelength imaging. There are in general two categories of approaches. The first category is superlenses, which amplifies the evanescent waves and then capturing them in the near field. The second category is the far-field techniques, including hyperlenses and time-reversal techniques.

Superlenses amplify the evanescent waves inside the lenses and then captures them in the near field. John Pendry brought up the idea of perfect lenses, which is the first study of superlenses [38]. Evanescent wave can be amplified inside negative index materials (NIM). Before and after the NIM, the evanescent wave will decay. If the refractive index inside the NIM is -1 and that outside is 1, and the wave path length inside the NIM is the same as that outside the NIM, then subwavelength

images can be restored perfectly after passing through the NIM. Superlenses based on NIMs are then demonstrated in acoustics [41, 40, 42]. The NIMs are realized with deep subwavelength resonator arrays. Later, researchers show that negative refractive index is not necessary for superlenses. The evanescent wave can be amplified at the interfaces of positive and negative density materials, while the bulk modulus remains positive [42, 43, 44]. Fabry-Perot resonances induce flat dispersions over a wide range of wave vectors, so that the materials that can excite fabry-Perot resonance can support the propagating of previously evanescent waves [45]. Trapped resonance inside acoustic waveguides can also support the propagation of evanescent waves and improve the resolution of imaging to subwavelength regime [46]. Superlenses are mostly formed by densely packed subwavelength structures such as tubes, resonators, membranes, etc. The thermal viscous loss largely limits their broader application.

If the evanescent wave can be converted to propagating wave and propagate in free-space or empty waveguide, the propagation distance will be much less limited by thermal viscous loss. This motivates the second category o fsubwavelength imaging techniques using metamaterials. Hyperlenses [47, 49] use cylindrical-shaped anisotropic metamaterials to couple and gradually compress large subwavelength wave vectors to small propagating wave vectors. At the exit of a hyperlens, image size is larger than wavelength and can be detected in the far-field. However, due to the geometric shape, higher spatial resolution of hyperlenses is at the cost of smaller field of view. The time reversal technique [50, 76, 77] uses random subwavelength scattering arrays to convert evanescent waves to propagating waves in the near field. In combination with time reversal mirror in the far-field, acoustic subwavelength focusing is realized. However, time reversal imaging is not a direct projection based technique. It requires a complex recording/playback system and the image needs to be formed at the same location as the object. Those requirements reduce the flexibility for applications.

Overall speaking, there are some remaining challenges to overcome before applying acoustic metamaterials to real-world applications in biomedical imaging, non-destructive testing, acoustic communication, etc. One of the challenges is the narrow working frequency bandwidth due to the resonance nature of the system. At the

same time, the resonating structure will also induce large thermal viscous loss, which is another challenges that limits the signal to noise ratio of the systems utilizing acoustic metamaterials. Another challenge is that most of the currently existing acoustic metamaterials are fixed once fabricated, thus cannot adapt to the fast changing environment in real time. In terms of fabrication, current 3D printing techniques offer great flexibility that enables experimental testing of acoustic metamaterials. However, The trade-offs between resolution, sample size, and speed speed limits the applications in higher frequency regime (above a few MHz). What's more, for underwater applications, it is difficult to realize impedance matching or large impedance contrast that is needed in designing underwater acoustic metamaterials.

1.2 Thesis organization

This thesis describes our efforts on developing acoustic metamaterials and addressing various challenges in acoustic sensing problems with the developed metamaterials. Besides the current chapter which is a brief introduction of the background of acoustic sensing and motivation of our work, Chapter 2 and Chapter 3 introduces the design of new acoustic metamaterials based on different phase/amplitude modulation methods. Chapter 4, Chapter 5 and Chapter 6 presents the design of new acoustic sensing methods and systems based on acoustic metamaterials.

Chapter 2 describes two different types of acoustic phase shifters, and metasurface designs based on them. The first type of phase shifters is formed by curved waveguide channels that generate larger phase delay than the straight channels occupying the same size in the wave propagation direction. The time delay after passing through the waveguide channel is a constant as the frequency changes, which means the phase shift is a function of frequency. Most of the previously designed phase shifters belong to this type. Based on this type of acoustic phase shifters, a new design of metasurface, called acoustic binary phase grating, is introduced. In each period of the metasurface, there are only two values of discrete phase shift, π and 0. The binary phase grating demonstrates highly tunable and efficient steering for waves of a large range of incident

angles with much simpler structure compared to previous metasurfaces. Theoretical calculation, simulation, and experimental measurement of the transmission properties of the binary phase grating will be presented for the binary phase grating.

The second type of phase shifter has the properties that the phase shift does not change with frequency in a broad frequency band. The phase shift is generated by the differential phase of two components. We first designed a broadband $\pi/4$ phase shifter. One component is a straight waveguide channel, the other component is a waveguide channel with a Helmholtz resonator side branch. The phase and amplitude responses are calculated based on its effective circuit model. By cascading different numbers of $\pi/4$ phase shifters, broadband phase shift units that can cover 0 to 2π phase range is simulated in COMSOL and further proves the validity of the design. Two potential applications of those designed broadband phase shifters in metasurfaces are proposed. One of them is a broadband energy divider, whose ratio of reflected and transmitted energy can be controlled broadbandly by our phase shifters. Another application is the design of flat acoustic lenses. Different spatial arrangement of phase shifters can generate different phase gradient. One type of flat lens can separate different frequency components in the incident plane wave to different directions after passing the lens. Other type of flat lens can focus different frequency components in the incident plane wave into different points.

Chapter 3 presents the design of hydrogel-based acoustic metamaterials with unprecedented tunable acoustic properties over broadband frequencies, in collaboration with Prof. Xuanhe Zhao's group at MIT. We call the proposed metamaterial meta-gel. The meta-gel consists of patterned channels in a tough hydrogel matrix, where air, water or liquid metal can be purged through the channels to tune the meta-gel's acoustic transmission over air-water-solid ranges and broadband frequencies on demand. We show that the acoustic properties of the meta-gel can be tuned by varying the volume ratio of the channels, properties and ratio of the different filler materials with combined experiments, theory and simulations. The meta-gel enables novel functions such as adjustable imaging regions of ultrasound, demonstrating tangible applications in underwater acoustics and medical imaging.

Chapter 4 demonstrates the design and experimental realization of an acoustic far-field subwavelength imaging system [78]. The resolution of acoustic imaging suffers from diffraction limit due to the loss of evanescent field that carries subwavelength information. Most of the current methods for overcoming the diffraction limit in acoustics still operate in the near-field of the object. Our system is based on wave vector filtering and conversion with a transmitter at the near-field and a spatially symmetrical receiver at the far-field. The transmitter/receiver is formed by the combination of a filter layer and a grating layer. The filter layer is composed arrays of Helmholtz resonators, and the grating layer is composed of the acoustic binary phase gratings presented in Chapter 2. By tuning geometric parameters of the transmitting/receiving pair, different spatial frequency bands can be separated and projected to the far-field. Furthermore, far-field imaging and edge detection of subwavelength objects are experimentally demonstrated. The proposed system brings new possibilities for far-field subwavelength wave manipulation, which can be further applied to medical imaging, nondestructive testing, and acoustic communication.

Chapter 5 proposes an alternative way for realizing the filter layer designed in Chapter 4. A slab of isotropic materials with slow sound speed compared to the surrounding medium is proposed to demonstrate subwavelength spatial filtering and enhancement. The theoretical expression of transmission coefficient for different incident spatial frequency is derived directly from the acoustic wave equation. The influence of different parameters on the transmission coefficient, such as the refractive index, thickness and loss factor of the slab, and the surrounding media (water or air) is studied systematically. Furthermore, the imaging resolution enhancement for a 2D object with subwavelength details is demonstrated with numerical simulation in COMSOL.

Chapter 6 introduces a new way to realize direction-selective acoustic transmission based on the acoustic binary phase gratings presented in Chapter 2. The combination of two gratings with different grating periods can select waves in only a narrow range of directions to pass through. The selected direction can be tuned by changing the grating period. The direction selection behavior is experimentally observed with 3D

printed phase gratings for two different directions. Further more, simulation shows that the combination of two gratings not only selects the direction, it also selects the frequency. The structure occupies a localized region in the direction-frequency space. By stacking multiple layers of the double-grating combinations working at different frequencies, broadband direction selection is demonstrated in simulation.

Chapter 2

Acoustic metasurfaces based on phase shifters

2.1 Introduction

Controlling the flow of waves and guiding them to directions and locations of interest has long been a popular area of research. Potential applications include imaging, communication, energy harvesting, etc. Among the solutions for wave controlling problems, metamaterials demonstrate promising performance by achieving effective material properties that does not exist in nature with engineered subwavelength resonating structures in both electromagnetics [79] and acoustics [17, 18]. As the 2D realizations of metamaterials, metasurfaces utilize the Huygens principle to discretize the surface into subwavelength unit cells, each having designed phase and/or amplitude responses [80, 81, 82, 83, 84]. In acoustics, most commonly explored metasurfaces are phase gradient metasurfaces [32, 33, 69, 70, 71, 85]. They are composed of phase shifters that can generate discrete values of phase shifts in the range of $[0, 2\pi]$. Those phase shifters are arranged in the surface to form the designed phase gradient for wavefront manipulation [67, 86, 87], acoustic absorption [34, 56, 88], cloaking [89, 90], hologram [73], etc.

In the previous acoustic metasurface designs, the resolution of spatial discretization is usually larger than five unit cells per period in order to form smooth phase

gradient. Such dense arrangement of unit cells limits the lateral resolution of the phase gradient. The complexity in design and fabrication of phase shifters also increases with the increasing resolution of phase response discretization. Here we propose a new way to achieve acoustic wave steering using only two discrete phase shift values, 0 and π. Those two phase shifters form the acoustic version of binary phase grating, which is a special type of diffraction grating. Binary phase grating in optics is known to not have even order diffraction [91]. By proper design that will be shown in this chapter, all or most of the energy in the transmitted wave can be directed to one single direction. This design will lead to simple and robust metasurface realization. Furthermore, it will be shown that the designed metasurface generates highly efficient negative refraction for a large range of incident and diffracted angles. There is another way to understand the binary phase grating. In [92], the authors developed an aggressive metasurface discretization method. The number of independent phase shifters required to redistribute the energy to any of the N propagating diffraction orders is N. If there are only two diffraction orders that are propagative and we want to redistribute all the energy to one of them, we only need two different phase shifters.

There is another common property in the acoustic phase shifters that are previously designed. The time delay ($\Delta\tau = \frac{1}{c_0}nl$, l is the physical path length, n is the refractive index, c_0 is the sound velocity in air) does not change with frequency. This property means that the actual phase shift ($\Delta\varphi = 2\pi nlf/c_0$, f is the frequency) is frequency dependent. In this chapter, I will also introduce a new type of acoustic phase shifters in which the phase shifts ($\Delta\varphi$) does not change with frequency. Such broadband phase shifters have been realized in electrical circuits [93, 94, 95]. Here we extend the idea from electrical circuits into acoustics with the help of acoustic transmission line theory [40, 96]. The designed phase shifters are then applied to metasurfaces that can steer waves with different frequencies to different directions, focus waves with different frequencies to different locations, and demonstrate broadband transmission and reflection controlling.

2.2 Acoustic binary phase grating

In this section, the design of acoustic binary phase grating based on curved waveguide channels is described. Theoretical calculation, full wave simulation and experiment for the diffraction properties of the designed acoustic binary phase grating is also presented.

2.2.1 System model

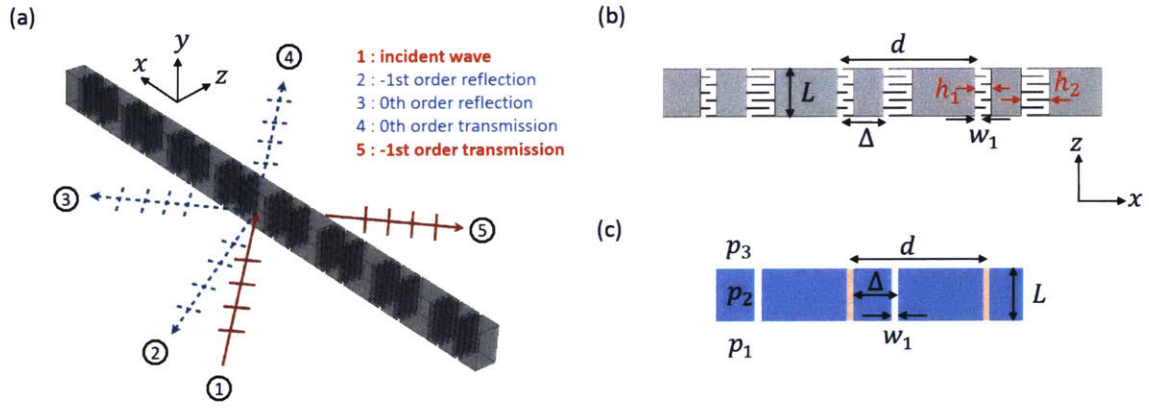

Figure 2-1: Models for grating layer. (a) System setup for wave steering with a layer of acoustic binary phase grating. Only two orders of diffraction are propagative, the -1st order and the 0th order. Among those four orders, most of the incidents energy is converted to the -1st order transmission by properly tune the parameters of the grating. (b) Model for acoustic binary phase grating with curved waveguide channels of different lengths. (c) An effective media model for the acoustic phase grating with waveguide channels.The refractive index in the yellow channel is n_1 and that in the white channel is n_2.

Ideally, the binary phase grating is composed of elements that produce uniform amplitude transmission and alternating phase shifts of 0 and π, as shown in Fig. 2-1a. Practically, it is difficult to find materials or structures that have perfect impedance matching with air in order to generate full transmission while also have sound speed variation in order to generate π phase shift. Narrow acoustic waveguide channels with cross section dimension smaller than wavelength are known to be able to generate phase delay proportional to the wave path length [66]. For waveguides with wave path length around $\lambda_0/2$ and λ_0 that generate phase shifts of π and 2π, the Fabry-Perot

resonances can be excited inside the tubes to achieve high transmission efficiency [97]. Based on those facts, we construct the acoustic binary phase grating in our system with the thickness in the z direction as $L = \lambda_0/4$. The π phase shifter is a curved channel of width h_1 and the 2π phase shifter is a curved channel of width h_2, as shown in Fig. 2-1b. According to [66], the curved channel with wave path length of l_w is equivalent to a straight channel of length $\lambda_0/4$ with refractive index $n_2 = 4l_w/\lambda_0$, where l_w can be calculated according to the values of L, h_1, and h_2.

The width of the channel inside, w_1, is much smaller than the working wavelength. The height of the channels in the y direction, h, is also smaller than wavelength. Those constrains are to ensure plane wave mode in the channels. For a binary phase grating with period $d = 2d_2$, the grating constant is $k_G = \pi/d_2$. The distance between the two phase shifters in one grating period is Δ. Plane wave expansion method [97] is used to calculate the theoretical transmission coefficients of different diffraction orders. The waves inside the channels and at both sides of the grating are expressed as combinations of plane wave modes. The coefficients of different modes are computed by matching pressures and perpendicular velocities at the two interfaces of the grating.

In the coordinate system shown in Fig. 2-1c, the pressure field $p_{in} = \mathrm{e}^{-jk_{x_0}x}$ incidents onto the grating from bottom (the propagating direction is in the z direction). So the pressure field at the bottom area of the grating is $p_1 = \mathrm{e}^{j(-k_{x_0}x - k_{z_0}z)} + \sum_m R_m \mathrm{e}^{j(-k_{x_m}x + k_{z_m}z)}$. The pressure field at the top area of the grating is $p_3 = \sum_m T_m e^{j(-k_{x_m}x - k_{z_m}(z-h))}$, where $k_{x_m} = k_{x_0} + \frac{2\pi}{d}m$, $k_{x_m}^2 + k_{z_m}^2 = k_0^2$. T_m and R_m represent the transmission and reflection coefficients of different orders. Since the width w_1 is much smaller than the wavelength, we assume that only the fundamental mode exists in the tubes. So the pressure distribution in the tube with refractive index n_1 is $p_{21} = A_1\mathrm{e}^{-jn_1k_0z} + B_1\mathrm{e}^{jn_1k_0z}$, and the pressure distribution in the tube with refractive index n_2 is $p_{22} = A_2\mathrm{e}^{-jn_2k_0z} + B_2\mathrm{e}^{jn_2k_0z}$. Define new parameters $v_1 = A_1 - B_1$, $v_1' = A_1\mathrm{e}^{-jn_1k_0L} - B_1\mathrm{e}^{jn_1k_0L}$, $v_2 = A_2 - B_2$, $v_2' = A_2\mathrm{e}^{-jn_2k_0L} - B_2\mathrm{e}^{jn_2k_0L}$. By matching the pressure and velocity at top ($z = L$) and bottom ($z = 0$) surfaces of the grating,

we obtain the following expressions for v_1, v_1', v_2, v_2':

$$-\Gamma_1 v_1 + [n_1 H + \Lambda_1] v_1' + n_2 G^+ v_2' = 0 \tag{2.1}$$

$$n_1 G^- v_1' - \Gamma_2 v_2 + [n_2 H + \Lambda_2] v_2' = 0 \tag{2.2}$$

$$[n_1 H + \Lambda_1] v_1 + n_2 G^+ v_2 - \Gamma_1 v_1' = 2\text{sinc}\left(\frac{k_{x_0}}{2} w_1\right) \tag{2.3}$$

$$n_1 G^- v_1 + [n_2 H + \Lambda_2] v_2 - \Gamma_2 v_2' = 2\text{sinc}\left(\frac{k_{x_0}}{2} w_1\right) \mathrm{e}^{jk_{x_0}(-\Delta)} \tag{2.4}$$

In those expression, $\Gamma_1 = \frac{1}{j\sin(n_1 k_0 L)}$, $\Gamma_2 = \frac{1}{j\sin(n_2 k_0 L)}$, $\Lambda_1 = \frac{\cos(n_1 k_0 L)}{j\sin(n_1 k_0 L)}$, $\Lambda_2 = \frac{\cos(n_2 k_0 L)}{j\sin(n_2 k_0 L)}$, $G^- = \sum_m \mathrm{e}^{jk_{x_m}(-\Delta)} \frac{a}{d} \frac{k_0}{\sqrt{k_0^2 - k_{x_m}^2}} \text{sinc}^2(\frac{k_{x_m}}{2} w_1)$, $G^+ = \sum_m \mathrm{e}^{jk_{x_m}\Delta} \frac{a}{d} \frac{k_0}{\sqrt{k_0^2 - k_{x_m}^2}} \text{sinc}^2(\frac{k_{x_m}}{2} w_1)$, $H = \sum_m \frac{a}{d} \frac{k_0}{\sqrt{k_0^2 - k_{x_m}^2}} \text{sinc}^2(\frac{k_{x_m}}{2} w_1)$. By solving those equations, we can get v_1, v_1', v_2, v_2'. Then the transmission coefficients (T_m) and reflection coefficients (R_m) are calculated as follows:

$$T_m(k_{x_0}) = \frac{a}{d} \frac{k_0}{\sqrt{k_0^2 - k_{x_m}^2}} \text{sinc}^2\left(\frac{k_{x_m}}{2} w_1\right) \left[v_1' + 2\mathrm{e}^{jk_{x_m}\Delta} v_2'\right] \tag{2.5}$$

$$R_0(k_{x_0}) = 1 - \frac{a}{d} \frac{k_0}{\sqrt{k_0^2 - k_{x_m}^2}} \text{sinc}^2\left(\frac{k_{x_m}}{2} w_1\right) \left[v_1 + 2\mathrm{e}^{jk_{x_m}\Delta} v_2\right] \tag{2.6}$$

$$R_{m\neq 0}(k_{x_0}) = -\frac{a}{d} \frac{k_0}{\sqrt{k_0^2 - k_{x_m}^2}} \text{sinc}^2\left(\frac{k_{x_m}}{2} w_1\right) \left[v_1 + 2\mathrm{e}^{jk_{x_m}\Delta} v_2\right] \tag{2.7}$$

By properly choosing n_1 and n_2, $T_m(k_{x_0})$ is tuned to around zero when m is an even integer $2N+1$. Among the odd orders, when $|k_{x_{2N+1}}| < k_0$, the $(2N+1)$th diffraction order generates propagating wave, and when $|k_{x_{2N+1}}| > k_0$, the $(2N+1)$th diffraction order generates evanescent wave that decays as it propagates away from the grating

and carries no energy to the farfield. From $|k_{x_{2N+1}}| = |k_{x_0} + (2N+1)\frac{2\pi}{d}| < k_0$, we get the number of allowed values of N as a function of $k_{x_0} \in [-k_0, k_0]$ and grating period $d \in [\lambda_0/5, 5\lambda_0]$ ($\lambda_0 = 75.6$mm is the wavelength in surrounding medium), as shown in Fig. 2-2.

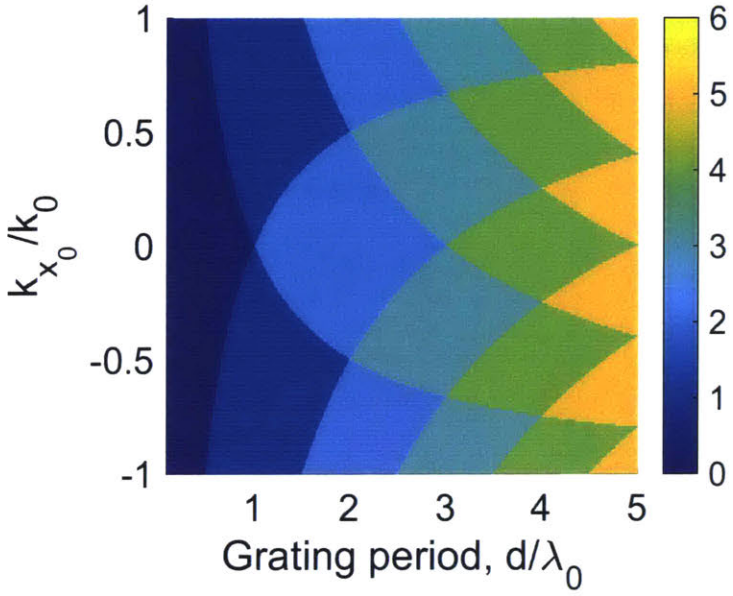

Figure 2-2: The number of allowed diffraction orders as a function of grating period d/λ_0 and the incident transverse wavenumber k_{x_0}/k_0.

From Fig. 2-2 we notice that when the grating period is small (which means the steering angle provided by the grating is large), the number of allowed N is zero. In this case, the incident wave is completely converted to evanescent wave in the transmission side. The evanescent wave does not carry any energy. Most of the energy is reflected. When d increases, the number of allowed N increases too. There is a region of particular interest, where only one value of N is allowed. Further observation found that $N = -1$ in the part of this region when $k_{x_0} > 0$ and $N = 0$ in the other part of this region when $k_{x_0} < 0$. The two parts are symmetrical with respect to the line $k_{x_0} = 0$, and correspond to the $+1$st or -1st order of diffraction, respectively.

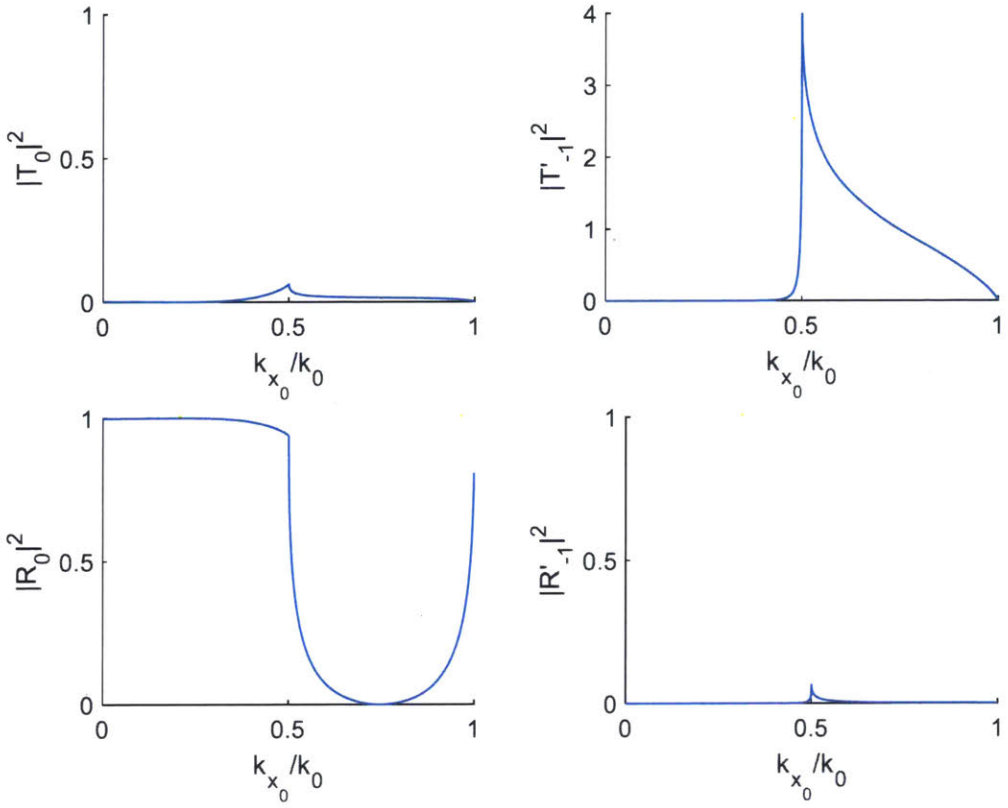

Figure 2-3: Diffraction coefficients of 0th and -1st orders diffraction in transmission and reflection when $d/\lambda_0 = 2/3$ and $\Delta = d/2$. (a) The 0th order transmission coefficient, $|T_0|^2$. (b) The -1st order transmission coefficient, $|T'_{-1}|^2$. (c) The 0th order reflection coefficient, $|R_0|^2$. (d) The -1st order reflection coefficient, $|R'_{-1}|^2$.

2.2.2 Diffraction properties of acoustic binary phase gratings

Choosing the period of the grating $d/\lambda_0 = 2/3$, and let the π phase shifter and 2π phase shifter distribute evenly in one period ($\Delta = d/2$), we plot the diffraction coefficients representing the energy distribution among transmitted and reflected 0th order and -1st order diffractions, $|T_0|^2$, $|T'_{-1}|^2 (= |T_{-1}e^{ik_z\delta}|^2)$, $|R_0|^2$ and $|R'_{-1}|^2 (= |R_{-1}e^{ik_z\delta}|^2)$, respectively, in Fig. 2-3. Here $k_z = \sqrt{k_0^2 - (k_{x_0} - k_G)^2}$ is the wave vector components in z direction, and $\delta = 0.1$m is an arbitrary distance larger than one wavelength so that all the evanescent components have decayed. The zeroth transmission coefficient $|T_0|^2$ is small as the result of proper choice of n_1 and n_2. At this d/λ_0 value, the additional wave vector provided by the phase grating is $k_G = 1.5k_0$. When $k_{x_0}/k_0 < 0.5$, all the diffraction modes are evanescent. As a

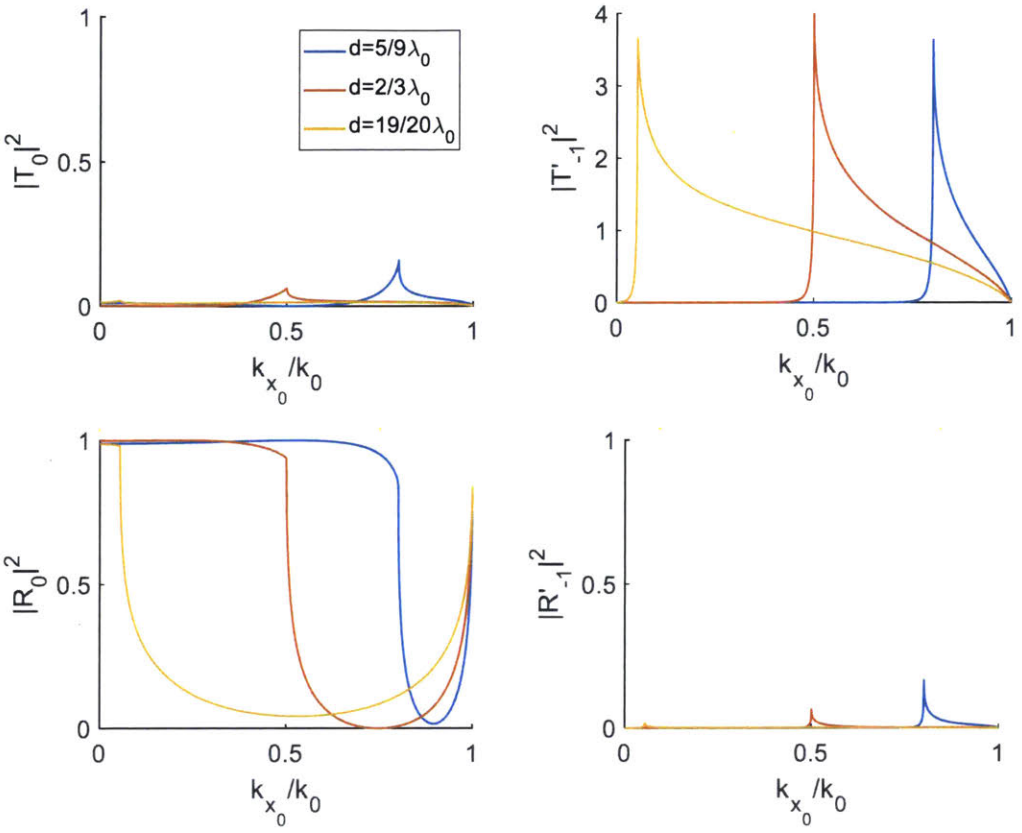

Figure 2-4: Comparison of diffraction coefficients in transmission and reflection when the grating periods are $d/\lambda_0 = 5/9, 2/3$, and $4/5$. In those plots $\Delta = d/2$. (a) The 0th order transmission coefficient, $|T_0|^2$. (b) The -1st order transmission coefficient, $|T'_{-1}|^2$. (c) The 0th order reflection coefficient, $|R_0|^2$. (d) The -1st order reflection coefficient, $|R'_{-1}|^2$.

result, $T_{-1}e^{ik_z\delta}$ and $R_{-1}e^{ik_z\delta}$ is around zero and the reflection coefficient R_0 is around one. When $0.5 < k_{x_0}/k_0 < 1$, The -1st diffraction order becomes propagating mode. As shown in Fig. 2-3c, R_0 has its smallest value at $k_{x_0}/k_0 = 0.75$. We define the diffraction efficiency as $1 - |R_0|^2$. At this input k_{x_0}, the -1st diffraction order corresponds to $k_x = -k_{x_0}$. The incident energy is diffracted to -1 order diffraction with 100% efficiency. Fig. 2-3 also tells us that for a wide input wave number range $k_{x_0}/k_0 \in [0.55, 0.95]$, the wave is steered to $k_x = k_{x_0} - k_G$, and the diffraction efficiency is larger than 75%.

By changing the grating period d, the added horizontal wave number k_G is changed, so is the steering angle. Fig. 2-4 gives the coefficients for different d that steer input

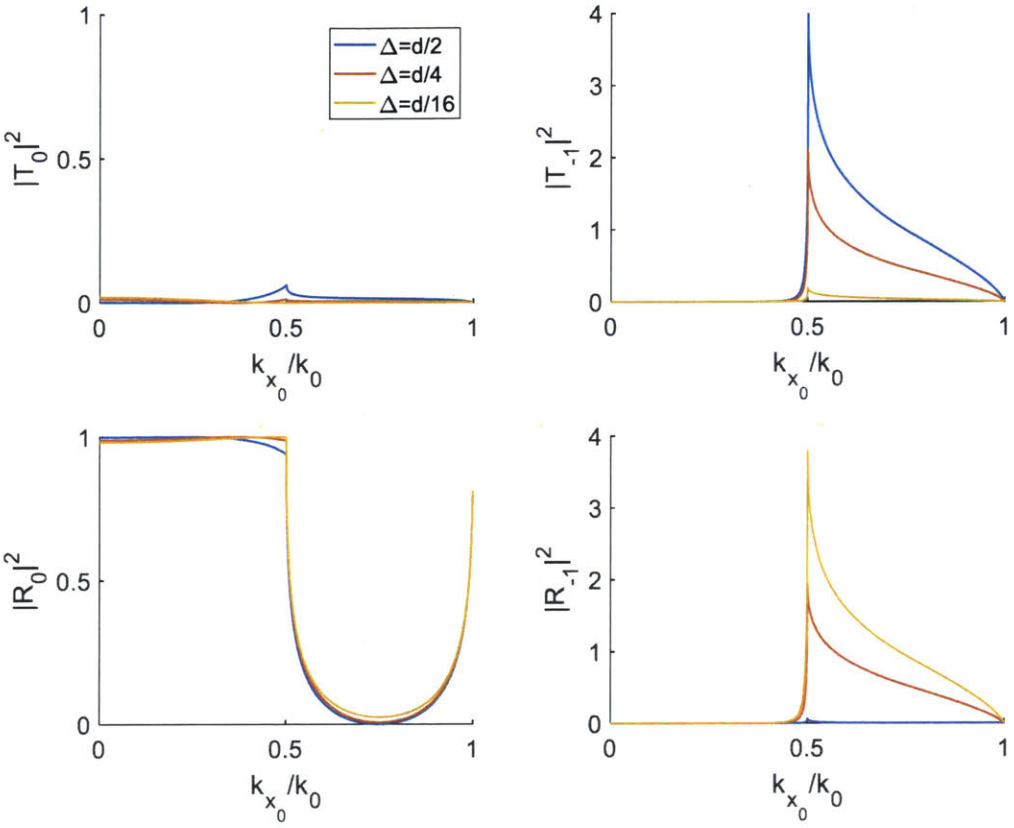

Figure 2-5: Comparison of diffraction coefficients in transmission and reflection when the distances between the π and 2π phase shifters in one unit cell are $\Delta = d/2, d/4$, and $d/16$. The grating period is $d/\lambda_0 = 2/3$. (a) The 0th order transmission coefficient, $|T_0|^2$. (b) The -1st order transmission coefficient, $|T'_{-1}|^2$. (c) The 0th order reflection coefficient, $|R_0|^2$. (d) The -1st order reflection coefficient, $|R'_{-1}|^2$.

waves to different directions. All the gratings with different d have similar behavior. The input wave with $k_{x_0}/k_0 \in [0, k_G/k_0 - 1]$ is all reflected back. The input wave with $k_{x_0}/k_0 \in [k_G/k_0 - 1, 1]$ is steered to a single direction $k_x = k_{x_0} - k_G$ in the transmission side. The steered wave locates at the same side as the incident wave. So the grating we designed offers a new way to achieve negative refraction. The diffraction efficiency is larger than 75% in most of the range $[k_G/k_0 - 1, 1]$ except the two small regions close to $(k_G/k_0 - 1)$ and 1.

In the previous discussion, the distance between two phase shifters in one period is $\Delta = d/2$. By changing Δ, the energy can be redistributed between R_{-1} and T_{-1}. Fig. 2-5 gives the diffraction coefficients when $\Delta = \frac{1}{8}d, \frac{1}{4}d, \frac{1}{2}d$. When Δ changes, the

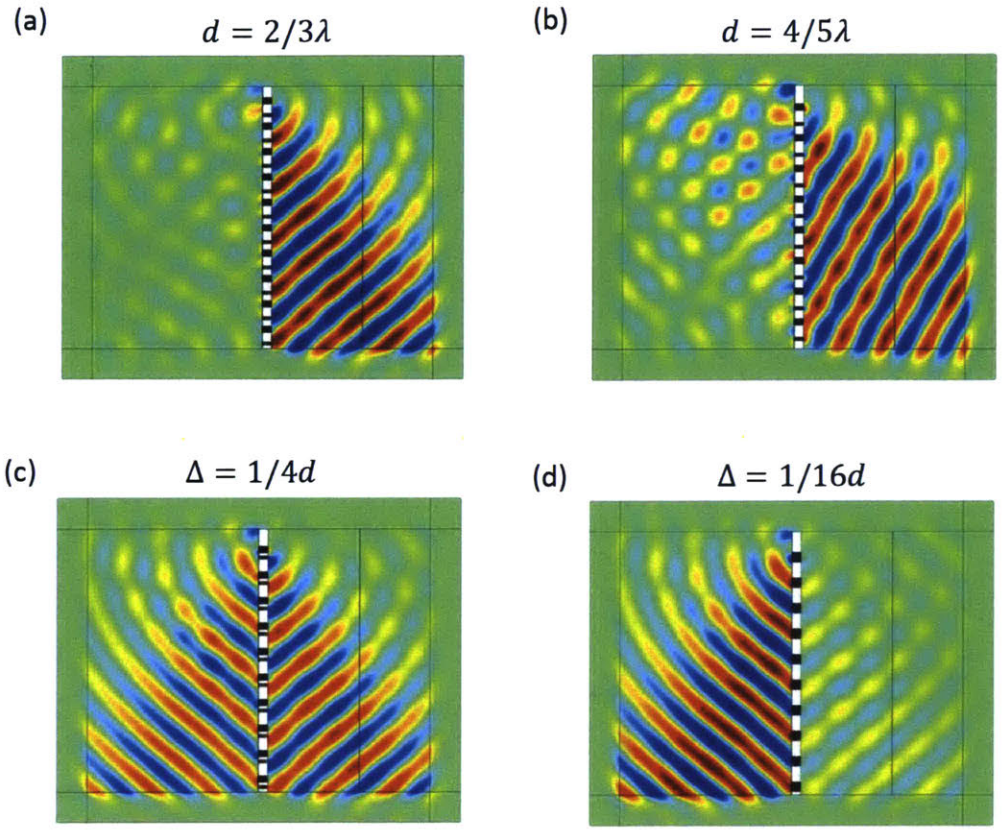

Figure 2-6: COMSOL simulation results of pressure distributions (left) and far-field patterns (right) of the scattered fields under different configurations. The incident wave number is $k_{x_0} = 0.75k_0$. (a) The grating period is $d/\lambda_0 = 2/3$. The distance between two phase shifters $\Delta = d/2$. (b) The grating period is $d/\lambda_0 = 4/5$. The distance between two phase shifters $\Delta = d/2$. (c) The grating period is $d/\lambda_0 = 2/3$. The distance between two phase shifters $\Delta = d/4$. (d) The grating period is $d/\lambda_0 = 2/3$. The distance between two phase shifters $\Delta = d/16$.

zeroth order transmission and zeroth order reflection does not change. The energy is redistributed between the -1st order reflection and -1st order transmission. When all the phase shifters are evenly distributed ($\Delta = d/2$), the -1st order transmission is the largest and the -1st order reflection is the smallest. The more uneven the distribution (Δ is closer to zero or closer to d), the larger the -1st order reflection.

COMSOL full wave simulation is performed for the designed gratings. In simulations, the gratings have finite number of periods and a total length of 520mm in the x direction. The grating is surrounded by perfect matching layers. A plane wave incident from one side of each grating, and the reflected and transmitted wave distribution

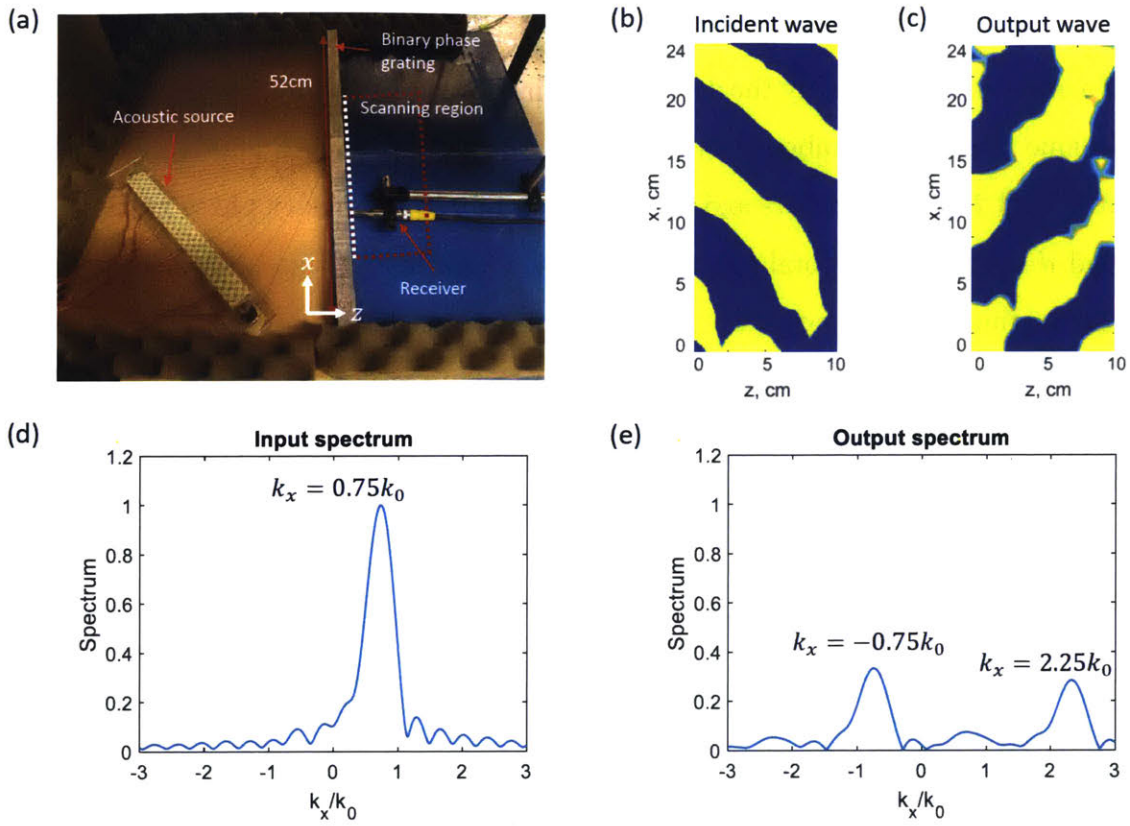

Figure 2-7: Experimental setup and measurement results for wave steering of a single binary phase grating. (a) Experimental setup. (b) Measured field distribution for incident wave with $k_{in} = -0.75k_0$. (c) Measured field distribution for transmitted wave. (d) Spatial spectrum of the incident wave measured along a line in x direction (white dashed line) when the grating is removed. (e) Spatial spectrum of the transmitted wave through the grating measured along the exit line (white dashed line) of the grating. The spectrum peak centered at $k_x/k_0 = -0.75$ is the propagating component we observed in (c) from the -1st order diffraction. The other peak centered at $k_x/k_0 = 2.25$ is the evanescent wave from the 1st order diffraction.

is calculated by finite element simulation in COMSOL. At the current simulation, the frequency we use is $f_0 = 4500$ Hz ($\lambda_0 = 76.2$ mm). The geometric parameters of the gratings are: $h_1 = 5.7$ mm, $h_2 = 12$ mm, $w_1 = 2.5$ mm, $L = \lambda_0/4 = 19.1$ mm. When $k_{x_0}/k_0 = 0.75$, for two different grating periods $d/\lambda_0 = 2/3$ and $4/5$, and when $\Delta = d/2$, the scattered field distributions are shown in Fig. 2-6a-b. The incident wave at $k_{x_0}/k_0 = 0.75$ is steered to different directions with larger than 75% efficiency. When $d/\lambda_0 = 2/3$, the field distributions when $\frac{1}{4}d$ and $\Delta = \frac{1}{16}d$ are also plotted in Fig. 2-6c-d. The energy is distributed from -1st order transmission to -1st

order reflection when Δ gets closer to zero.

In order to further verify the designed grating for wave steering, we use 3D printing technique (Autodesk Ember printer, acrylic resin) to fabricate a number of π phase shifters and 2π phase shifters and assembled them into the binary phase grating with period $d = 2/3\lambda_0$ and total length of 52 cm, as shown in Fig. 2-7a. The binary phase grating is then put inside a waveguide formed by two acrylic plastic plats. The height of the grating is 5 mm, while the height of the waveguide is 3 cm. The openings above and below the grating is sealed by other acrylic plastic blocks. A transducer array formed by eight transducers, each having diameter of 2 cm, is used as the line source. The line source is tilted to designed angles to generate plane waves in required directions. In the example shown in Fig. 2-7b and c, the line source is tilted to the angle that generates $k_{in} = -0.75k_0$. Eight periods of sinusoidal wave at frequency $f_0 = 4500$ Hz is incident on the grating. A receiver scans the transmitted wave in a scanning region of size 24 cm $\times$ 10 cm. At each scanning point, a time signal is obtained. Fig. 2-7b shows the incident wave in an empty waveguide at one time instance. Fig. 2-7d gives the spatial spectrum of the incident field. The spatial spectrum is obtained by first taking spatial Fourier transform for the time signal at each point along the line parallel and closest to the location of the grating exit (white dashed line in Fig. 2-7a), and then take spatial Fourier transform for the time domain Fourier coefficient at $f = 4500$ Hz. The spatial spectrum shows that the incident wave have wave number parallel to the grating as $k_{in} = 0.75k_0$. Fig. 2-7c gives the field distribution after the wave passes through the grating. The wave direction is changed as expected. The slight phase discontinuity observed in Fig. 2-7c is due to the distortion of the signal at the specific time instance. The distortion comes from the small "left-over" zeroth order diffraction from the binary phase grating and the defects in the fabricated grating layer. The spatial spectrum of the transmitted wave shown in Fig. 2-7e indicates that the transmitted wave is dominated by the component with $k_{out} = -0.75k_0$, which is generated by the -1st order diffraction of the grating. The zeroth order diffraction is small, as indicated by the almost completely attenuated peak at $k_{in} = 0.75k_0$. The other peak centered at

$k_x/k_0 = 2.25$ is the evanescent wave from the 1st order diffraction. This component will decay as it leaves the grating, so we cannot observe it in Fig. 2-7c. Comparing the peak value in Fig. 2-7d and e, we found that the transmission efficiency in the current experiment is relatively low (30%). This is mainly because of the fact that the height of the grating (5 mm) is much smaller than the height of the waveguide (3 cm). The thermal visous loss also further decreases the efficiency.

Compared to the metasurfaces previously proposed, the binary phase grating has the advantage of simple structure with only two different phase shift units while providing high steering efficiency, even for nearly-horizontal wave. The grating can demonstrate highly efficient negative refraction, as well as tunable energy distribution between transmitted and reflected wave in the -1 order diffraction. The total energy efficiency is limited by the thermal viscous loss in the narrow waveguide channels. In the future, it is possible to use other methods to achieve the two phase shift values that have less thermal viscous loss and easier fabrication method.

2.3 Broadband acoustic phase shifter design and applications in metasurfaces

In this section, a new type of broadband phase shifter in acoustics and its applications in metasurfaces for wave steering, focusing and energy transmission control is described.

2.3.1 Broadband phase shifters

In [95], the authors present the design of a Schiffman differential phase shifter for microwave circuits, which consists of two components. One component is a straight transmission line and the other is a coupled transmission line. Assume the input to both components is V. The output from the straight transmission line is $Ve^{j\phi_1}$, and the output from the coupled transmission line is $Ve^{j\phi_2}$. The phase difference $\phi_1 - \phi_2$ between the two components is nearly constant over broadband frequency

range by proper design of the two components. Similar as in [95], we consider a differential phase shifter in acoustics, in which the phase shift is the phase delay difference between two components. Here, one component is a straight 2-D acoustic waveguide with width d and length l_0 (Fig. 2-8a), which is analogous to the straight transmission line in [95], and the other component is a straight 2-D acoustic waveguide (width d and length l_1) with a Helmholtz resonator side branch (neck r_1, h_1 and cavity r_2, h_2) (Fig. 2-8b), which is similar to the coupled transmission line in [95]. We call the first component straight component and the other component resonator component.

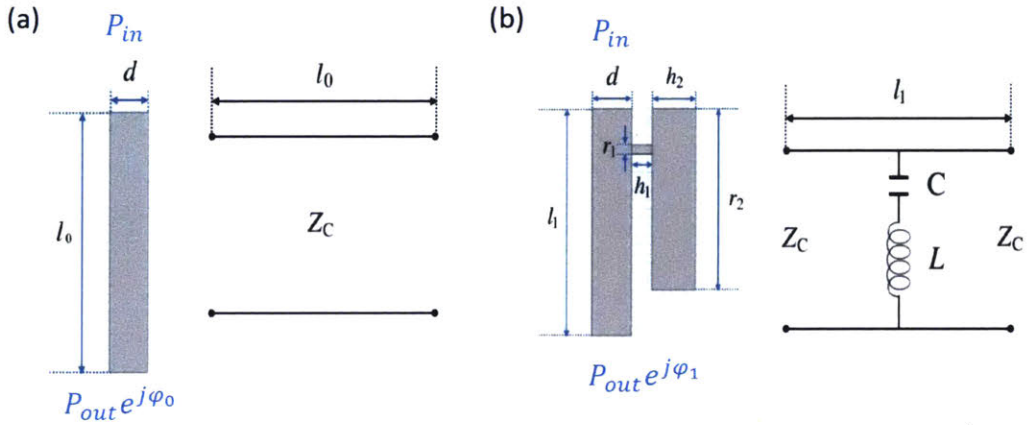

Figure 2-8: System schematics and the transmission line model for the two components of the phase shifter. (a) Straight component. (b) Resonator component.

The effective circuit model for the straight component is a delay line of length l_0, as shown in Fig. 1(c). Assume P_{in} is the incident pressure field, and $P_{out}e^{j\varphi_0}$ is the transmitted pressure field. If the waveguide is lossless, we have:

$$\frac{p_{out}}{p_{in}} = 1, \tag{2.8}$$

$$\varphi_0 = -kl_0. \tag{2.9}$$

The effective circuit model for the resonator component is a delay line with a side branch, which is composed of a capacitor and an inductor, as shown in Fig. 1(d). The characteristic impedance of a tube with width d is $Z_c = \frac{c\rho}{d}$, where ρ is the density of the material in the tube and c is the sound velocity inside the tube. The impedance

of the series of a capacitor and an inductor is $Z_s = \frac{1}{j\omega C} + j\omega L$. Here, $C = \frac{r_2 h_2}{\rho c^2}$ is the effective capacitance of the cavity in the Helmholtz resonator and $L = \frac{\rho h_1}{r_1}$ is the effective inductance of the neck of the Helmholtz resonator. The effective impedance at the point of side branch (point O) can be written as the parallel of Z_c and Z_s, which is

$$Z = \frac{(\frac{1}{j\omega C} + j\omega L) Z_c}{Z_C + \frac{1}{j\omega C} + j\omega L}. \tag{2.10}$$

The transmission coefficient T for the pressure field at point O is:

$$T = \frac{2Z}{Z_C + Z} = 1 - \frac{Z_C}{Z_C + 2j(\omega L - \frac{1}{\omega C})}. \tag{2.11}$$

We also assume P_{in} as the incident pressure field, $P_{out} e^{j\varphi_1}$ as the transmitted pressure field, and the system is lossless. We have:

$$\frac{p_{out}}{p_{in}} = |T|. \tag{2.12}$$

$$\varphi_1 = -kl_1 + \angle(T). \tag{2.13}$$

The differential phase shift between the straight component and the resonator component is

$$\Delta\varphi = \varphi_1 - \varphi_0 = k(l_0 - l_1) + \angle(T). \tag{2.14}$$

2.3.2 $\pi/4$ phase shifter

In our design, the 2π phase range is covered with eight phase shifters. So each phase shifter provides $\pi/4$ phase shift. If we assume the background material in the tubes is air ($c = 343$ m/s, $\rho = 1.29$ kg/m^3), and set $\Delta\varphi$ in Eq. (2.14) to $\pi/4$, we can obtain the geometrical parameters of the tubes and the Helmholtz resonator as follows: $l_0 = 25$ mm, $l_1 = 30$ mm, $d = 5$ mm, $r_1 = 1$ mm, $h_1 = 2.5$ mm, $r_2 = 20$ mm, $h_2 = 5.5$ mm.

The theoretical phase and amplitude response results are shown in Fig. 2-9a-c. The absolute phase of both the straight component (φ_0) and the resonator component (φ_1) are plotted as the function of input frequency in Fig. 2-9a, and the differential phase

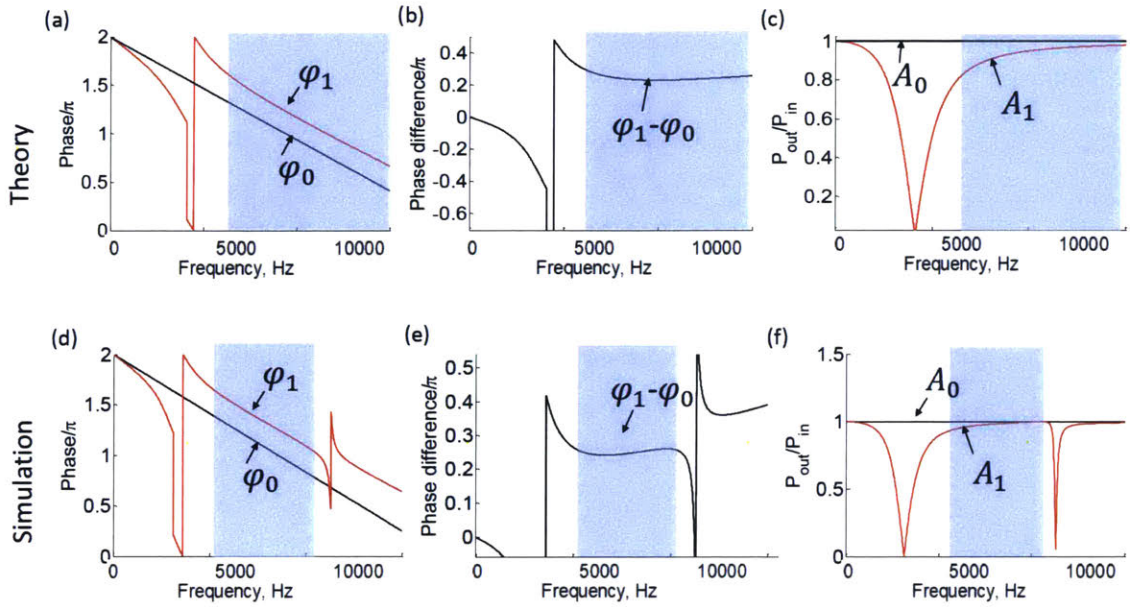

Figure 2-9: Theoretical calculation and FEM simulation of the designed $\pi/4$ phase shifter. (a) Theoretically calculated phase responses of the straight component (black line) and the resonator component (red line). (b) Theoretical phase difference of the two components. (c) Theoretically calculated amplitude responses of the straight component (black line) and the resonator component (red line). (d-f) FEM simulation results corresponding to (a-c).

shift $\Delta\phi$ is plotted as the function of frequency in Fig. 2-9b. From these two figures we can see that the resonator component has a resonance frequency at around 3.6kHz. When the frequency is above 5kHz, the $\Delta\varphi$ is around $\pi/4$. So the combination of the straight component and the resonator component can be seen as a broadband $\pi/4$ differential phase shifter when frequency is larger than 5 kHz. The amplitude response of the two components are plotted in Fig. 2-9c. Since the working frequency range (> 5 kHz) is away from the resonance frequency (3.6 kHz), the amplitude response is also broadband in this range.

Simulation is implemented in Comsol 4.4. The background material, the geometrical parameters of the tubes and the Helmholtz resonator are the same as in the theoretical results. The system is lossless and the boundaries are all hard wall boundary. The simulated phase and amplitude responses are shown in Fig. 2-9d-f. Similar to in Fig. 2-9, the absolute phase of both the straight component (φ_0) and

the resonator component (φ_1) are plotted in Fig. 2-9d, and the differential phase shift $\Delta\varphi$ is plotted in Fig. 2-9e. The resonance frequency is around 3 kHz, which is smaller than that in the theoretical result (3.6 kHz) and there is another resonance at 8.6 kHz. These differences are mainly because that we simplify the Helmholtz resonator into a series of a capacitor and an inductor. This simplification neglects the radiation impedance of the Helmholtz resonator and also neglects the higher order resonances. The differential phase shift $\Delta\varphi$ is around $\pi/4$ when frequency is from 4.5 kHz to 8.6 kHz. The amplitude response of the two components are plotted in Fig. 2-9f and is broadband within the range 4.5 kHz to 8.6 kHz.

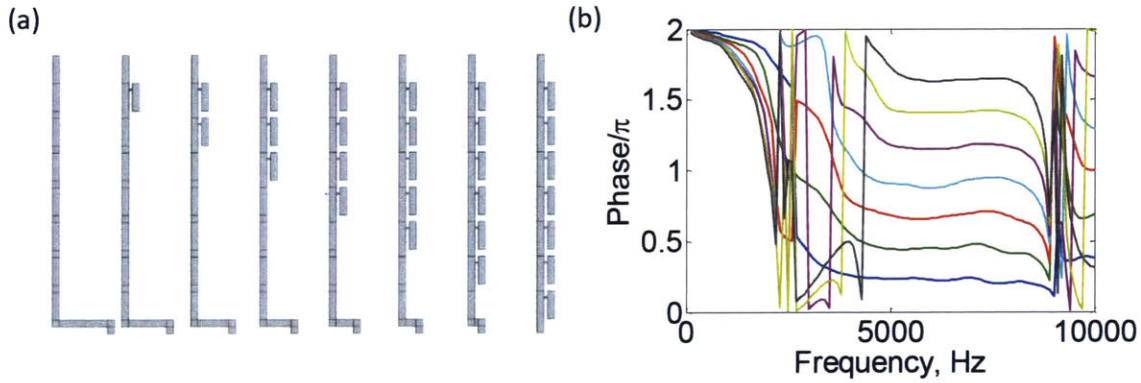

Figure 2-10: (a) Combinations of straight components and resonator components that can cover 0 to 2π phase shift. (b)Simulated differential output phase of the eight phase shifters components in (a)

Each combination of a straight component and a resonator component can generate $\pi/4$ phase shift. By cascading different numbers of resonator components and straight components, we can construct phase shifter units that cover the 0 to 2π phase range. As shown in Fig. 2-10a, if we assume the output phase of the first unit from the left is φ_0, then the output phases of the second to eighth units are $\varphi_k = \varphi_0 + k\frac{\pi}{4}$. Each unit provides a phase step of $\pi/4$ compared to the previous one. Comsol simulation of the differential output phase $(\varphi_i - \varphi_0)$ of each unit when the input phases are the same is shown in Fig. 2-10b. Within frequency range 4.8 kHz to 8.5 kHz, these units provide nearly flat phase shifts from 0 to 2π with a step $\pi/4$.

2.3.3 Acoustic metasurfaces based on the broadband phase shifters

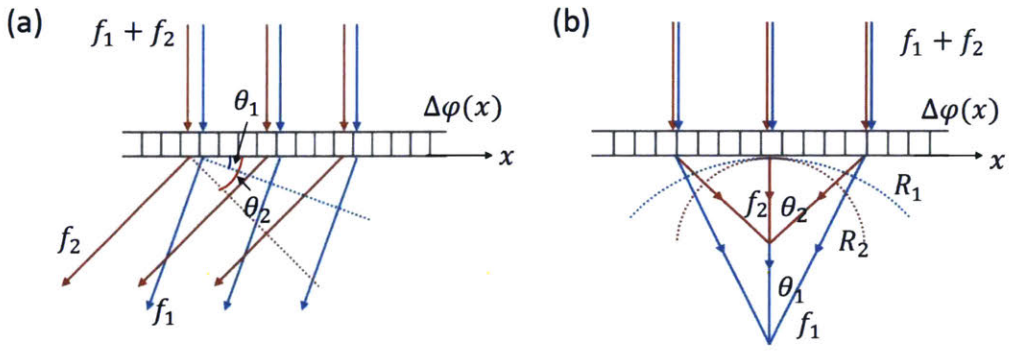

Figure 2-11: Acoustic metasurfaces designed for: (a) wave steering, (b) focusing.

New acoustic metasurfaces can be designed based on the units (Fig. 2-10a) that can achieve 0 to 2π broadband phase shift. The following are two examples.

The first example is acoustic flat lenses. As shown in Fig. 2-11, if we divide the surface into discrete units and put different phase shifters we designed into these unit cells, any phase gradient $\Delta\theta(x)$ can be generated. If $\Delta\varphi(x)$ is a linear function of the position, $\Delta\varphi(x) = Ax$ (Fig. 2-11a), the flat lens will change the propagating direction of the incident plane wave. If the incident wave is perpendicular to the surface, and we assume that the angel between the output wave and the surface is θ_i (different i represents different frequency). Then we have:

$$\frac{d\varphi}{dx} = A, \tag{2.15}$$

$$d\varphi = \frac{2\pi f_i}{c}\sin(\theta_i)dx, \tag{2.16}$$

$$\sin(\theta_i) = \frac{Ac}{2\pi f_i} = \frac{\lambda_i}{2\pi}\frac{d\varphi}{dx}, \tag{2.17}$$

where λ_i is the wavelength of the incident wave. From Eq. (2.17), we see that the propagation direction of transmitted wave is related to the phase gradient (which is a constant in our case because of the broadband phase shifter) and wavelength. This flat lens can separate different frequency components in the input wave to different

directions. Similarly, if we want to focus the incident plane wave into a point, as shown in Fig. 2-11b, then $\frac{x}{R_i} = \sin(\theta_i) = \frac{\lambda_i}{2\pi}\frac{d\varphi}{dx}$. So

$$R_i = \frac{2\pi x}{\lambda_i \frac{d\varphi}{dx}} \tag{2.18}$$

From Eq. (2.18), R_i, the distance of the focusing point to the surface, is inversely proportional to the wavelength. Thus this flat lens can focus different frequency components in the input wave to different points.

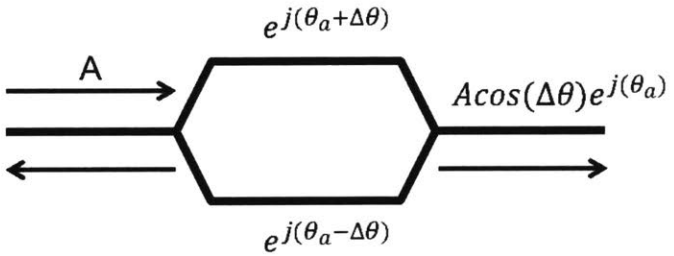

Figure 2-12: Broadband energy divider.

The second example is a broadband energy divider shown in Fig. 2-12. It's a two port device. The incident wave is assumed as A. The incident wave is first split into two branches. The two branches have different phase shifts $(\theta_a + \Delta\theta, \theta_a - \Delta\theta)$. The two branches are combined into one output port. The wave in the output pot can be written as:

$$P = Ae^{j(\theta_a+\Delta\theta)} + Ae^{j(\theta_a-\Delta\theta)} = A\cos(\Delta\theta)e^{j(\theta_a)} \tag{2.19}$$

From Eq. (2.19) we can see that the output amplitude is determined by the phase difference of the two arms and the output phase is determined by the average phase shift of the two arms. If we put our designed broadband phase shifter units to the two arms, then this two port device and tune the reflected and transmitted acoustic energy broadbandly.

2.4 Summary

In summary, in this chapter, we described two different types of phase shifters and the applications of them in designing acoustic metasurfaces. One of them is the phase shifter based on curved waveguide channels. The curved channel with different path length will generate different phase delays for the incident acoustic wave. The phase delay in this case is frequency dependent. We proposed and realized the acoustic binary phase grating that can achieve highly efficient diffraction of incident acoustic wave with much less phase shifters in each period, thus decreased the system complexity. Another type of phase shifters is the broadband acoustic phase shifter, which is based on the differential phase delay of two components. The phase shift is frequency independent over a broadband frequency range. This type of phase shifters can be used to design acoustic metasurfaces that can steer different frequency to different directions and focusing different frequency to different locations. It can also achieve broadband energy reflection and transmission control. In later chapters, I will show novel acoustic imaging devices for biomedical imaging, non-destructive testing, acoustic communication, etc., that are based on those phase shifters and metasurfaces.

Chapter 3

Hydrogel-based acoustic metamaterial with extremely tunable properties

3.1 Introduction

Acoustic materials have attracted great research interests in recent years, exemplified by novel devices such as acoustic lenses [41, 98, 99, 100], cloaks [55, 101] and absorbers [102, 103] with broad applications in medical imaging [72, 104, 105], underwater sonar and communication and marine biology [106]. Whereas conventional acoustic materials including metals, polymers, ceramics and woods are frequently used in various environments of solids, liquids and gases in different ranges of frequency, they cannot significantly change their acoustic properties once fabricated. Acoustic impedance mismatch between the acoustic materials and the environments causes energy loss and pulse aliasing, posing a grand challenge to acoustic imaging and communication. Addressing this challenge requires acoustic materials capable of varying acoustic impedance according to the different surrounding media and working frequencies. In particular, increasing resolution and efficiency of signal transductions in underwater and biomedical applications requires acoustic impedance match between

the acoustic materials and water over broadband frequency. Whereas mechanisms such as electro/magneto-mechanical coupling [107, 108, 109, 110] and structural deformation [111, 112] have been employed to tune acoustic properties of solid materials, the ranges of tunable acoustic properties and frequencies are limited. To the best of our knowledge, there has been no report on acoustic materials capable of tuning acoustic properties to match those of water, air and a variety of solid materials over broadband frequencies.

Here we propose meta-gel, a new approach and material system to achieve tunable acoustic properties over air-water-solid ranges and broadband frequencies based on a hydrogel matrix with designed channels that can be filled with various media. Since the major constituent of hydrogels is water (e.g., over 90 vol%), the density of and speed of sound in hydrogels are almost identical to the corresponding properties of water. Therefore, the acoustic impedance of hydrogels matches that of water much better than any conventional acoustic material [113]. Meanwhile, the polymer networks in hydrogels endow them with elasticity, which maintains the shapes of hydrogel matrix and filler media in the matrix. In addition, hydrogels have been designed to be mechanically tough [114, 115], and tough hydrogels with microstructural features such as channels and cavities have been fabricated to give functional structures and devices [113]. A combination of the above-mentioned hydrogels' unique properties enables the design of meta-gel capable of unprecedented tunable acoustic properties.

The work in this chapter is in collaboration with Prof. Xuanhe Zhao's group at MIT, including Kai Zhang (visiting scholar at Prof. Zhao'g goup), Qi He and Shaoting Lin (Graduate students at Prof. Zhao's group), and Yi Chen (Postdoc at Beijing Institute of Technology). The author contributions are: K.Z, Q. H and S.L prepared the samples. C.M and K.Z measured the acoustic properties. C.M did the numerical simulation and Y.C carried out the MST calculations.

3.2 Schematics of meta-gel

In Fig. 3-1A, we schematically illustrate the design of meta-gel. The meta-gel is based on a tough hydrogel matrix, which achieves high toughness by integrating mechanisms for dissipating mechanical energy and maintaining high stretchability of polymer networks [116] (see Materials and Methods for details on tough hydrogel matrix). Since the acoustic impedance of the hydrogel well matches that of water (19), underwater acoustic waves of various frequencies can achieve nearly complete transmission through the hydrogel matrix [113] (Fig. 3-1A). Next, we design and fabricate a pattern of air channels with significant volume fraction in the tough hydrogel matrix and then connect the channels with a set of pumps. The pumps can purge various filler media including air, water and liquid metal into the channels on demand (Fig. 3-1B-D). We propose the following hypotheses for the design and operation of meta-gel: i). When the channels are filled with water, the meta-gel recovers the acoustic properties of water, resulting in the total transmission of acoustic wave. ii). When the channels are filled with air, the acoustic properties of meta-gel can approximate those of air, resulting in the total reflection of acoustic wave. iii). When the channels are filled with liquid metal, the acoustic properties of meta-gel can approach those of soft solid materials such as biological tissues and engineering rubbers, resulting in the combined transmission and refection of acoustic waves. iv). The tunability is broadband.

To validate the above hypotheses, we adopt a pattern of equally spaced parallel channels in a tough hydrogel sheet, as shown in Fig. 3-2 (see Materials and Methods for details on fabrication of the hydrogel matrix with channels). The dimensions of the meta-gel sheet are 195 mm $\times$205 mm $\times$15.5 mm (length $\times$ width $\times$ thickness) with 31 circular channels embedded on the middle plane of the thickness direction and periodically arranged along the length direction. The diameter of the channel (a) is 2.2 mm, the distance between two adjacent channels (L) is 6.5 mm, and the length of the channel is 195 mm. A set of pumps are used to supply filler media including air, water and liquid metal (99.99% pure Gallium, The Gallium Shop) into the channels (Fig. 3-2C). Fig. 3-2 shows meta-gel sheet filled with water, air, and

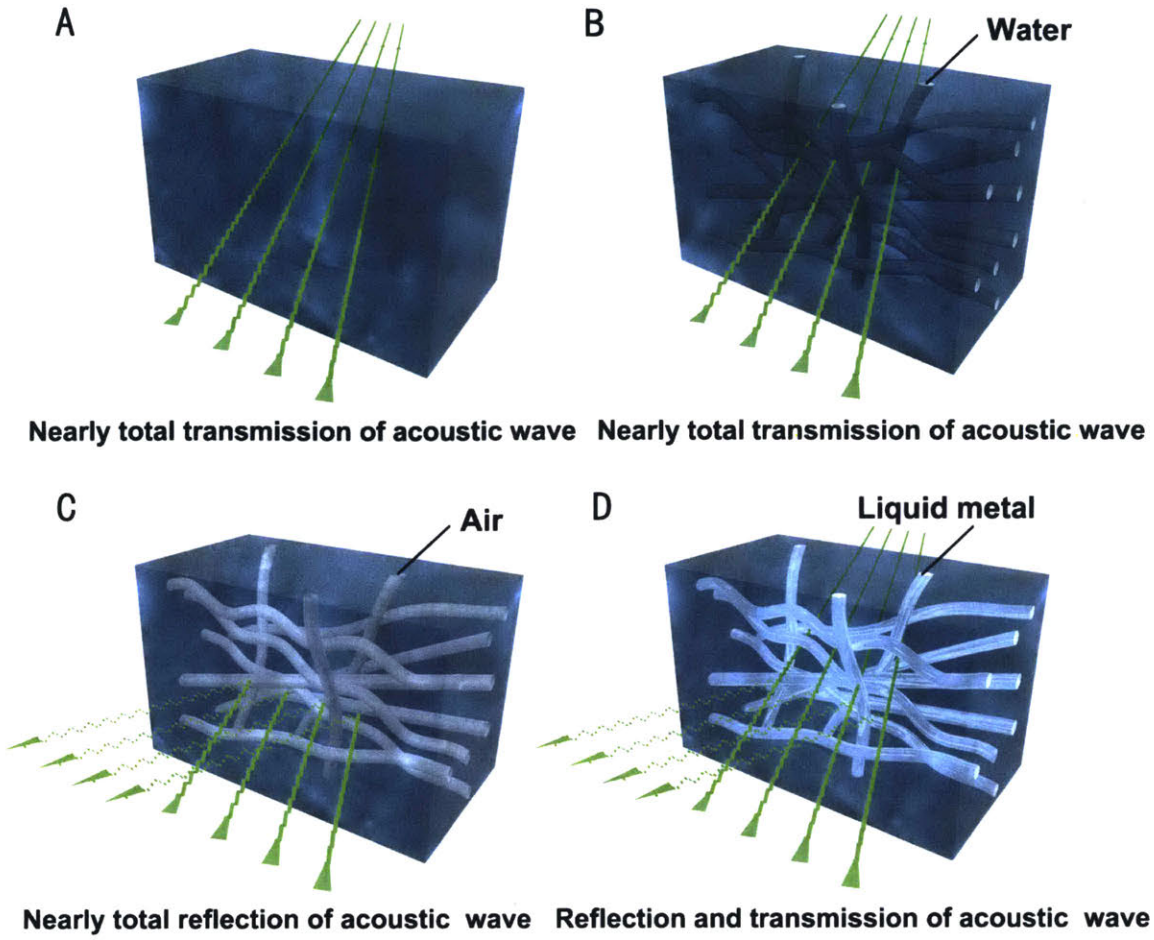

Figure 3-1: Schematics on the design of meta-gel consisting of microstructural channels in a tough hydrogel matrix. (A) Acoustic impedance of the homogeneous hydrogel matches well with water, resulting in nearly total transmission of underwater acoustic wave. The effective acoustic properties of the microstructured meta-gel can be tailored by filling the channels with various liquids including (B) water, (C) air and (D) liquid metal, giving nearly total transmission, nearly total refection and combined transmission and refection of acoustic waves, respectively.

liquid metal. Another thinner meta-gel sheet, whose dimensions are 280 mm $\times$110 mm $\times$6 mm (length $\times$ width $\times$ thickness) with 46 square channels, is also fabricated. The width of the square channel (a) is 3 mm, and the distance between two adjacent channels (L) is 6 mm.

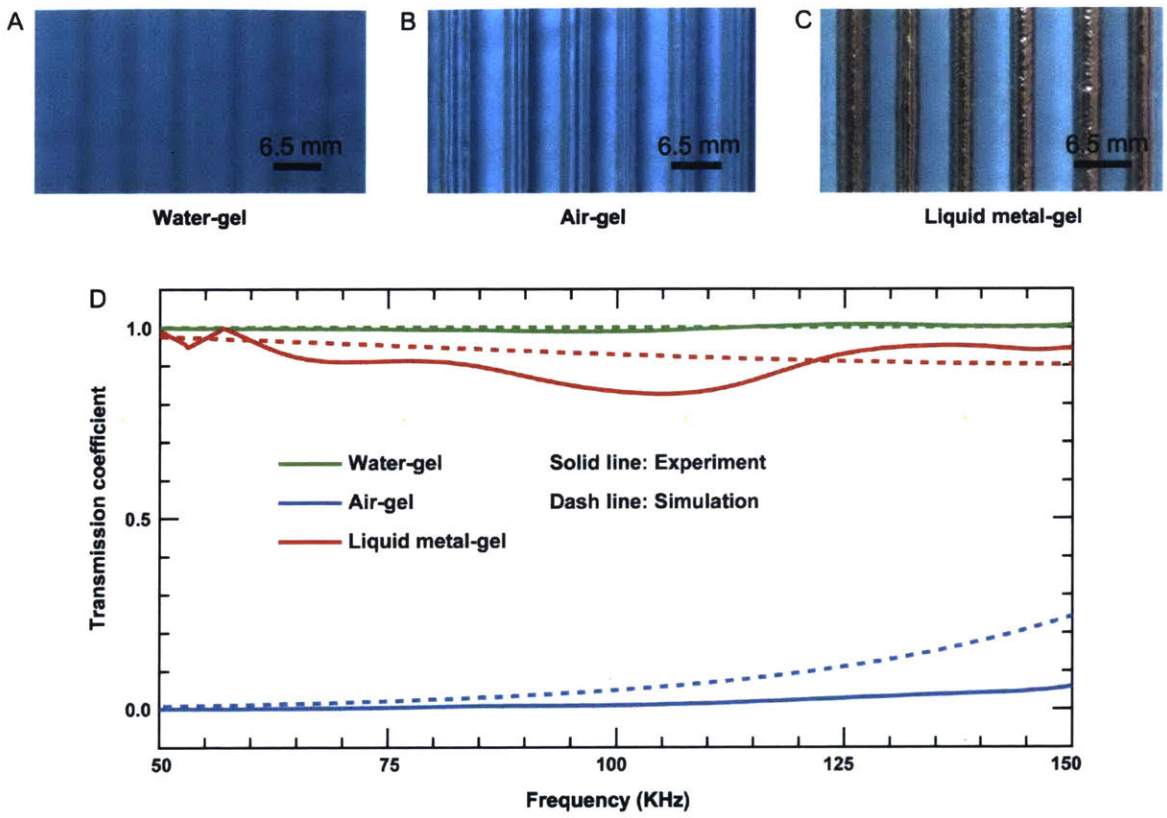

Figure 3-2: Broadband tunable acoustic transmission through the meta-gel by changing filler materials. The images of the underwater meta-gel filled with water (A), air (B) and liquid metal (C). (D) Transmission coefficient of the meta-gel filled with water, air and liquid metal over various frequencies from experiment and numerical simulation. Solid lines represent experiment result while dash lines represent simulation result. The diameter of the channel is $a = 2.2$ mm and the distance between two adjacent channels is $L = 6.5$ mm.

3.3 Tunable acoustic transmission of meta-gel sheet

The sound transmission through the meta-gel sheet (195 mm $\times$205 mm $\times$15.5 mm) is measured in a water tank for frequencies from 50 KHz to 150 KHz, a typical range for underwater acoustics, such as fish finding sonar, echo sounder, etc. (See Materials and Methods for details on experimental acoustic transmission coefficient measurements). Besides the structural design, we mainly propose to tune the acoustic properties of the meta-gel with two methods: 1) change filler materials inside the channels, 2) change the filling ratios of different materials.

3.3.1 First tuning method: change filler materials

For the first method, we fill all the channels with one type of material (air, water or liquid metal), and tune the acoustic properties by switching between different filler materials. The sound transmission through the meta-gel sheet is measured from 50 KHz to 150 KHz. As shown in Fig. 3-2D, the measured transmission coefficient of meta-gel sheet with water is above 0.989 in the frequency range from 50 KHz to 150 KHz, indicating almost perfect acoustic impedance match between the meta-gel and water. In contrast, when the channels in meta-gel sheet are filled with air, the transmission coefficient of meta-gel sheet reduces below 0.06 for all tested frequencies, giving nearly total refection of underwater acoustic waves. When the channels in meta-gel sheet are filled with liquid metal, the average transmission coefficient of meta-gel sheet is measured to be around 0.9. These results demonstrate that the meta-gel possesses tunable transmission coefficient of underwater acoustic waves in the frequency range of 50 KHz to 150 KHz, by simply varying the filler materials.

3.3.2 Second tuning method: change the filling ratios

In the second tuning method, we change the filling ratio of channels occupied by water and air while fixing the value of a and L. Here the diameter of the channel a is 2.2 mm and the distance between two adjacent channels L is 6.5 mm. N_{water} (N_{air}) denote the number of channels filled with water (air). Fig. 3-3A-C show the images of meta-gel sheets with different filling ratios. In Fig. 3-3D, we plot the experimentally measured acoustic transmission coefficient with $N_{\text{water}} : N_{\text{air}} = 1 : 0$, $1 : 3$, $1 : 5$, $1 : 8$, $2 : 1$, $2 : 2$, $2 : 3$ and $0 : 1$, respectively, in frequency range from 50 KHz to 150 KHz. By tuning N_{water} and N_{air}, the transmission coefficient can be tuned to cover the range from 0 to 1. The numerical simulated transmission coefficients for the same set of N_{water} and N_{air} are plotted Fig. 3-3E (see Materials and Methods for details), showing similar trends as Fig. 3-3D. The discrepancy between the experiment and the numerical simulation is mainly caused by the following factors: The experiment measures a finite system with boundaries while the simulation models an infinite periodic

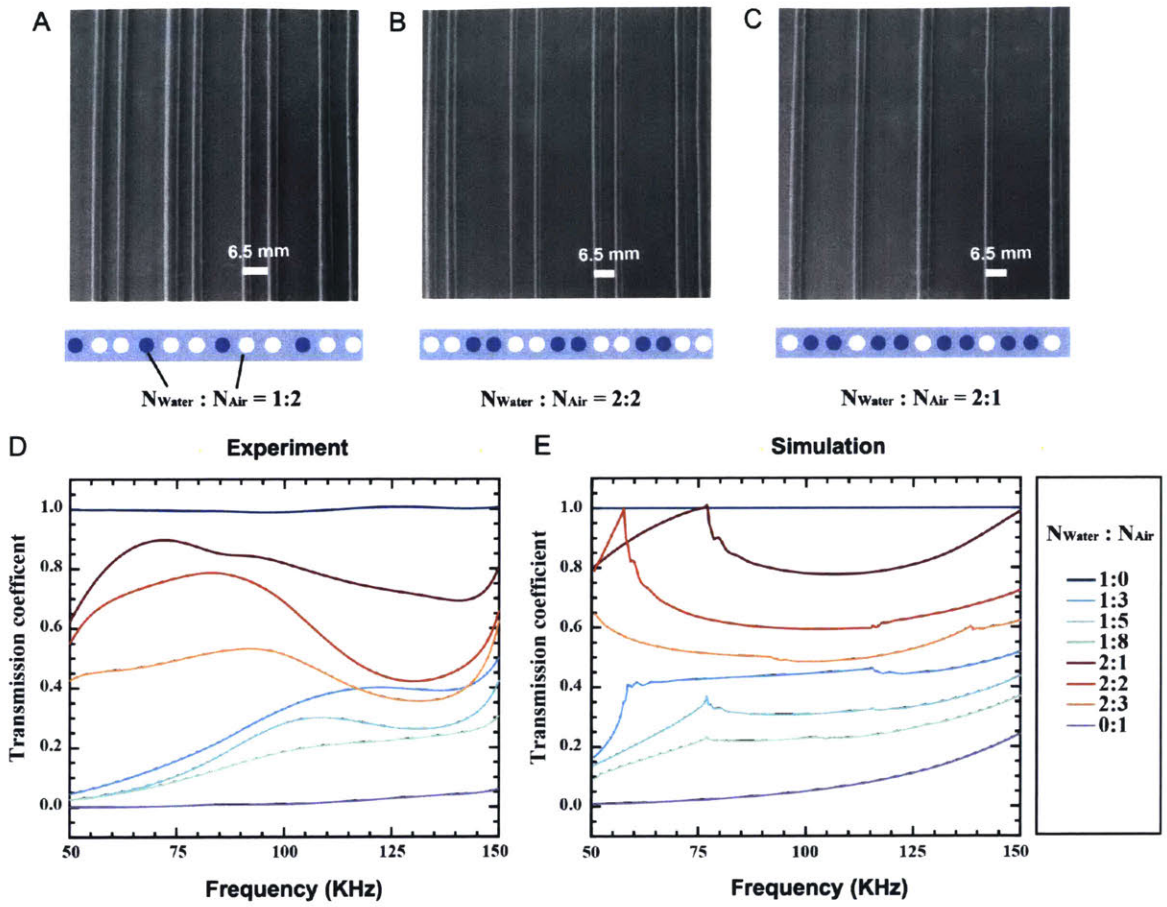

Figure 3-3: Broadband and wide-range tunable acoustic transmission of the meta-gel by changing the filling ratios. The images of the underwater meta-gel with different filling ratio. The ratio of water to air (Nwater: Nair) canbe mixed at (A) $1:2$, (B) $2:2$, (C) $2:1$. (D-E) Experiment and numerical transmission coefficients for the set of Nwater and Nair. The width of the square channel $a = 2.2$ mm and the distance between two adjacent channels $L = 6.5$ mm.

system. The viscous loss and background noise in experiments are not presented in the simulation.

3.3.3 Acoustic transmission coefficient of the meta-gel sheet over frequency range 0.4 KHz to 5 MHz by simulation

Using COMSOL simulation, we calculate the acoustic transmission coefficient over a wide frequency range of 0.4 KHz to 5 MHz (Fig. 3-4) for the sample with dimensions $a = 2.2$ mm and $L = 6.5$ mm. According to the calculation, when the channels are filled with water, the transmission coefficient of meta-gel still maintains almost 1 from 0.4 KHz to 5 MHz, which also has been proved by experimental test and previous work [113]. By change the filling ratio N_{air} and N_{water}, transmission coefficient in the range from 0 to 1 can be achieved from 0.4 KHz to 150 KHz, beyond the range in experimental measurements. In addition, as increasing frequency range, acoustic transmission coefficient of the meta-gel gradually approaches to almost constant over MHz. Multiple scattering theory (MST) method [117] is also developed by collaborators for calculating the acoustic transmission coefficient of the meta-gel sheet. MST and COMSOL simulation matches very well, as indicated by Fig. 3-4.

Besides the comsol simulation and MST method, the wave transmission behavior in this high frequency range can also be explained by the principle of geometrical acoustics [118]. The number of acoustic rays transmitted through the meta-gel layer is proportional to the projected area of the meta-gel regions that are impedance matched with water (i.e., the hydrogel part) on a plane perpendicular to the acoustic rays. The lowest acoustic transmission coefficient of air-gel sheet that can be achieved by the currently fabricated meta-gel sample with $a = 2.2$ mm and $L = 6.5$ mm is around 0.68. The area fraction of air-to-water for the fabricated meta-gel is $2.2 : 4.3$. The acoustic transmission through the meta-gel is $4.3/(2.2 + 4.3) = 0.66$, which matches with the MST model and numerical simulation. The transmission coefficient increases linearly with the increase of L (i.e., the decrease of air's volume fraction). Thus, tunable transmission coefficient fully covering the range from 0 to 1 in high frequency can be achieved by designing air's volume fraction.

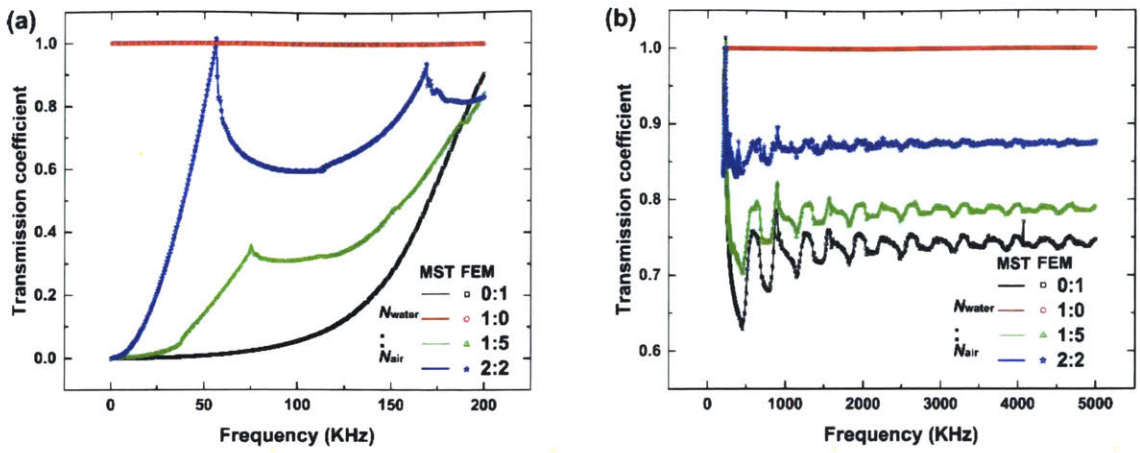

Figure 3-4: Transmission coefficient of the meta-gel in frequency range 0.4 KHz to 5 MHz. The filling ratio N_{water} and N_{air} is $0:1$, $1:5$, $2:2$ and $1:0$, respectively. The width of the channel in the meta-gel is 2.2 mm and the distance between two adjacent channels is 6.5 mm.

3.4 Application of the meta-gel sheet to ultrasonic imaging

The tunable acoustic properties of the meta-gel at MHz frequency are also investigated by ultrasound imaging. As illustrated in Fig. 3-5, a layer of the meta-gel is placed between the probe of an ultrasonic imaging system (GE LOGIQ E9; GE Healthcare) and a plastic frog all immersed in water. At frequency of 4 MHz, the frog can be clearly imaged by the ultrasound probe when the channels in the meta-gel are filled with water, but disappears once the channels are filled with air, as shown in Figs. 3-5B and 3-5C. The horizontal lines of white spots in the upper part of the scan (Figs. 3-5C) is the air-gel sheet. Although the transmission coefficient of our used meta-gel sheet at MHz frequency is not zero, the meta-gel can still be used as a shutter for ultrasonic imaging with adjustable imaging windows. It is indicated that acoustic wave can transmit through the meta-gel filled with water, but scattered by the meta-gel filled with air, where both the amplitude and phase of the acoustic wave are disturbed. We can achieve imaging windows of target objects with "on" state and "off" state on demand. The switch between the "on" state and "off" state is controlled by pumping water or air into the corresponding regions of the meta-

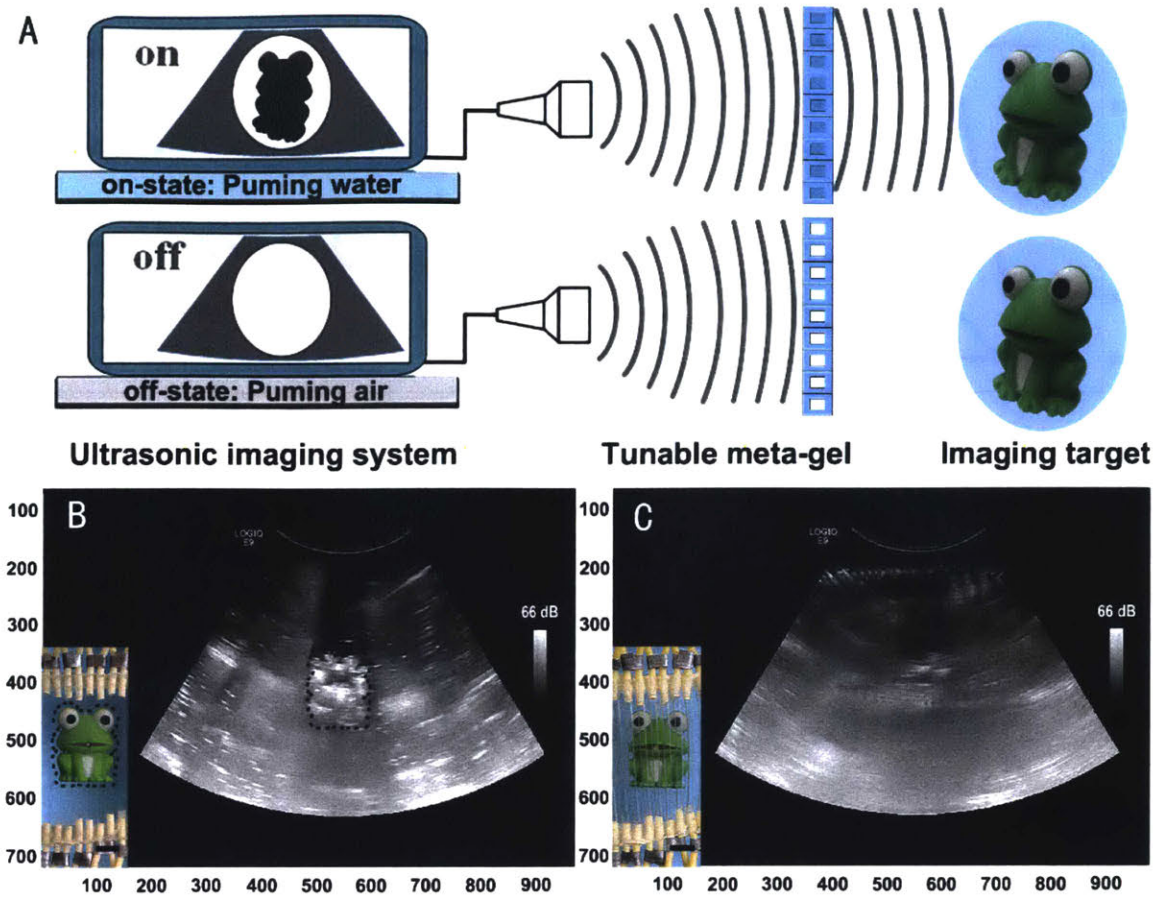

Figure 3-5: Application of the meta-gel in on-demand ultrasound imaging. (A) Schematics of the on-demand ultrasound imaging system enabled by a meta-gel filled with water or air. Experimental results of ultrasound imaging through the meta-gel filled with (B) water and (C) air at 4 MHz. The target can be imaged clearly by ultrasound through a layer of meta-gel filled with water, while disappears once the channels in the meta-gel are filled with air. The scale bar of the optical image in (B) and (C) is 12 mm. The grey scale bar of the ultrasound image in (B) and (C) represents the dynamic range defined as the difference between the maximum and minimum values of the displayed signal.

gel. This capability of selectively blocking unwanted region of strong scattering can potentially enable ultrasound imaging with enhanced contrast.

3.5 Effective parameter retrieval of meta-gel

If the acoustic wavelength is larger than microstructural features of a meta-gel (e.g., channel diameter), the meta-gel can be taken as a macroscopically homogeneous

material. The effective material properties are calculated with effective medium theory [119]. With the effective parameter retrieval method [119], we calculate the acoustic impedance of the meta-gel with all the channels filled with water, air, or liquid metal, from the transmission and reflection coefficients from numerical simulation in COMSOL. (See Supplementary Material for details on the calculation). The acoustic impedance of the meta-gel as a homogenous material can be expressed as [120] $Z = \sqrt{\rho_{\text{eff}} \cdot K_{\text{eff}}}$, where ρ_{eff} and K_{eff} are the effective density and bulk modulus of the meta-gel, respectively. The values of ρ_{eff} and K_{eff} depend on the density and bulk modulus of the filler media. In comparison, we further give the Z values of typical gases, liquids and solids.

We plot the Z values of meta-gel with different dimensions and filler ratios in Fig. 3-6. Z values of all the air-gel sheet occupies the region where acoustic impedance is close to zero. The Z values of all the water-gel sheets keep the same as water, which is independent on the structural feature, while that of liquid metal-gel sheets vary with increasing filling volume fraction (data points I-VI). By tuning the filler media, the meta-gel sheet with the channel pattern used in experiments (i.e., $a = 2.2$ mm, $L = 6.5$ mm) can possess a region of Z between 3.75×103 Pa s/m and 2.16×106 Pa s/m. The meta-gel sheet with $a = 3$ mm, $L = 6$ mm have a larger region of Z between 0.18×103 Pa s/m and 2.70×106 Pa s/m, which almost covers the Z values of typical liquids (e.g., water, acetone, benzene, ethyl alcohol, carbon tetrachloride, glycerin, oil, toluene, seawater, sulfuric acid, in the range of 0.81×106 Pa s/m to 2.34×106 Pa s/m) and soft solids (e.g., fat, muscle, blood, rubber, polyethylene, polystyrene, in the range of 1.39×106 Pa s/m to 2.41×106 Pa s/m), even approaching the Z values of gases (e.g., air, oxygen, nitrogen, argon, chloroform, in the range of 0.41×103 Pa s/m to 0.51×103 Pa s/m). To further expand the meta-gel's tunable range of Z, we choose other dimensions of the channel pattern (i.e., $a = 2.2$ mm, $L = 2.3$ mm, or $a = 3$ mm, $L = 3.1$ mm,), so that the channels occupy a higher volume fraction of the meta-gel sheet than the previous structure. Z of the meta-gel with $a = 2.2$ mm and $L = 2.3$ mm can reach to 1.04×107 Pa s/m by filling liquid metal, while the liquid metal-gel with $a = 3$ mm and $L = 3.1$ mm can achieve

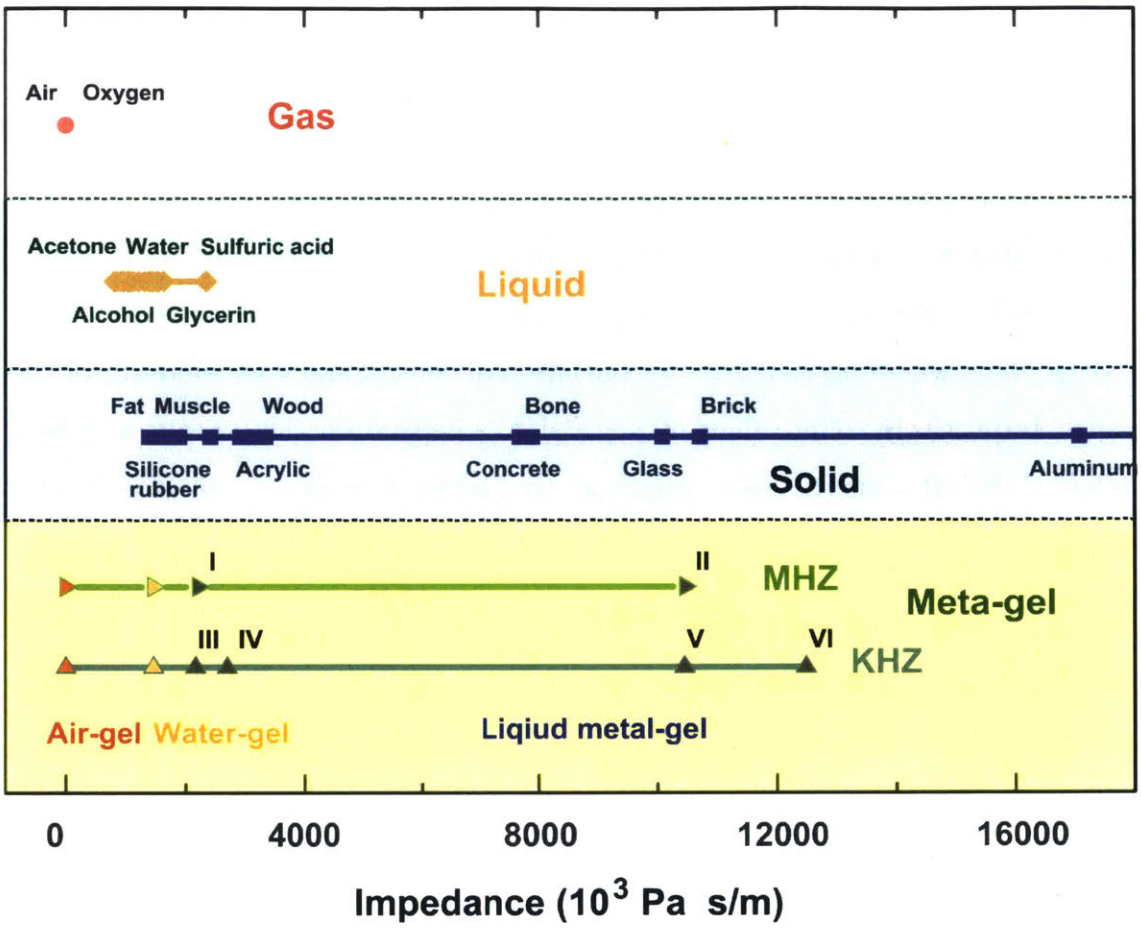

Figure 3-6: Acoustic impedances for various types of solids, liquids and gases in comparison with the meta-gel filled with various ratios of fillers and different dimensions. Meta-gel sheet with six different structural feature are proposed. I: $a = 110$ μm, $L = 325$ μm; II: $a = 110$ μm, $L = 115$ μm; III: $a = 2.2$ mm, $L = 6.5$ mm, used in experiments; IV: $a = 3$ mm, $L = 6$ mm; V: $a = 2.2$ mm, $L = 2.3$ mm; VI: $a = 3$ mm, $L = 3.1$ mm.

the maximum value of Z to 1.25×107 Pa s/m. (Fig. 3-6). When the wavelengths of acoustic waves in water are larger than the feature sizes of meta-gel sheet, the tunability of Z is based on material composition instead of resonance, so the meta-gel works broadbandly. When the feature size of meta-gel sheet is shifted down to micro size (i.e., $a = 110$ μm, $L = 115$ μm), simulation shows that the working frequency range of tunable Z is shifted to MHz. (Fig. 3-6) (See Materials and Methods for details).

3.6 Materials and Methods

3.6.1 Hydrogel and meta-gel composite fabrication

Hydrogel materials. In the tough hydrogel, Acrylamide (AAm; Sigma-Aldrich A8887) was used as the monomer for the covalently crosslinked stretchy network and Sodium alginate (Sigma-Aldrich A2033) ionically was used for the physically crosslinked dissipative network. In the polyacrylamide (PAAm) network, N,N-methylene-bis-acrylamide (Bis; Sigma-Aldrich 146072) was used as crosslinker and Ammonium Persulphate (APS, Sigma A3678) was used as photoinitiator. Calcium chloride solution (Sigma 746495) was prepared for the tough hydrogel, to provide the calcium ion crosslinked with Sodium alginate.

Fabrication on meta-gel composite. The meta-gel sheet consisted of straight channels arranged in the tough hydrogel matrix. A mold with 46 detachable bars was first designed and fabricated using laser cutter (Epilog Mini/Helix; Epilog Laser) based on computer aided design drawings. Crosslinked hydrogels were fabricated by pouring pre-gel solution into the mold and covering glass plates. The pre-gel solution for the soft PAAm-alginate hydrogel was prepared by mixing carefully degassed aqueous solution (12 wt.% AAm, 2 wt.% sodium alginate, 0.2 wt.% Bis, 0.2 mol/liter APS). The crosslinked hydrogels in the mold were kept in a humid chamber for one hour to make sure the formation of crosslinks. Thereafter, the crosslinked hydrogel sample were carefully separated from the mold. The hydrogel sample with channels were immersed in calcium chloride solution (2.22 wt.%) for 4 days to generate the tough hydrogel, and then in deionized water at least for 4 days to reach equilibrium swollen state. Finally, the neighboring channels in the hydrogel were connected by using a latex tube and sealed with superglue.

3.6.2 Acoustic measurement of the transmission coefficient of the meta-gel sheet

We conducted transmission measurements for the fabricated sample with $a = 2.2$ mm (channel diameter) and $L = 6.5$ mm (period). The whole sample has dimension of 195 mm $\times$205 mm $\times$15.5 mm with 31 channels. The emitter is held fixed at the bottom of the water tank, with a 10 cm perpendicular distance to the middle of the sample. The sample is held completely horizontal and stable on an acrylic plastic ring plate which is fixed by four rods extending from the top platform. The receiver is placed 2 cm above the sample, and it is attached to a 2D moving stage which is attached to the top platform.

For each configuration of the channel filling, we measure the acoustic transmission through the sample for frequency range [50. 150] KHz with CTG Model ITC-1042 (emitter) and CTG Model ITC-1089D (receiver). The emitter sends a pulse wave with the form $P_{in} = \cos(2\pi \times 5 \times 10^4 t)$, where $t \in [0.\, 1/(4 \times 10^5)]$ s. The time domain waveform and the Fourier spectrum of P_{in} are plotted in Fig. 3-7(a-b). A receiver scans a region of 5 cm^2 located 2 cm above and parallel to the sample. At each scanning point, a transmitted signal is measured as a time domain waveform. A typical measured signal Pout for frequency range [50, 150] KHz is plotted in Fig. 3-7(c). A time window is multiplied to the measured signal to get the portion of direct transmitted signal through the sample and eliminate reflections and those transmitted through the surrounded opening in the water tank. We then perform Fourier transform to the time-windowed signal to obtain the frequency spectrum (Fig. 3-7(d)). The spectrum covers the frequency range of [50. 150] KHz. After getting the frequency spectrums for all the points in the scanning region, we compute the average power spectrum by averaging the square of each individual frequency spectrum. The transmission coefficient of each channel filling configuration is obtained from the ratio of two measurements. One measurement is performed when the sample is put in the water tank, and anther measurement is performed when sample removed, serving as reference. We plot the acoustic transmission coefficients for different filling configurations in

frequency range $[50, 150]$ KHz.

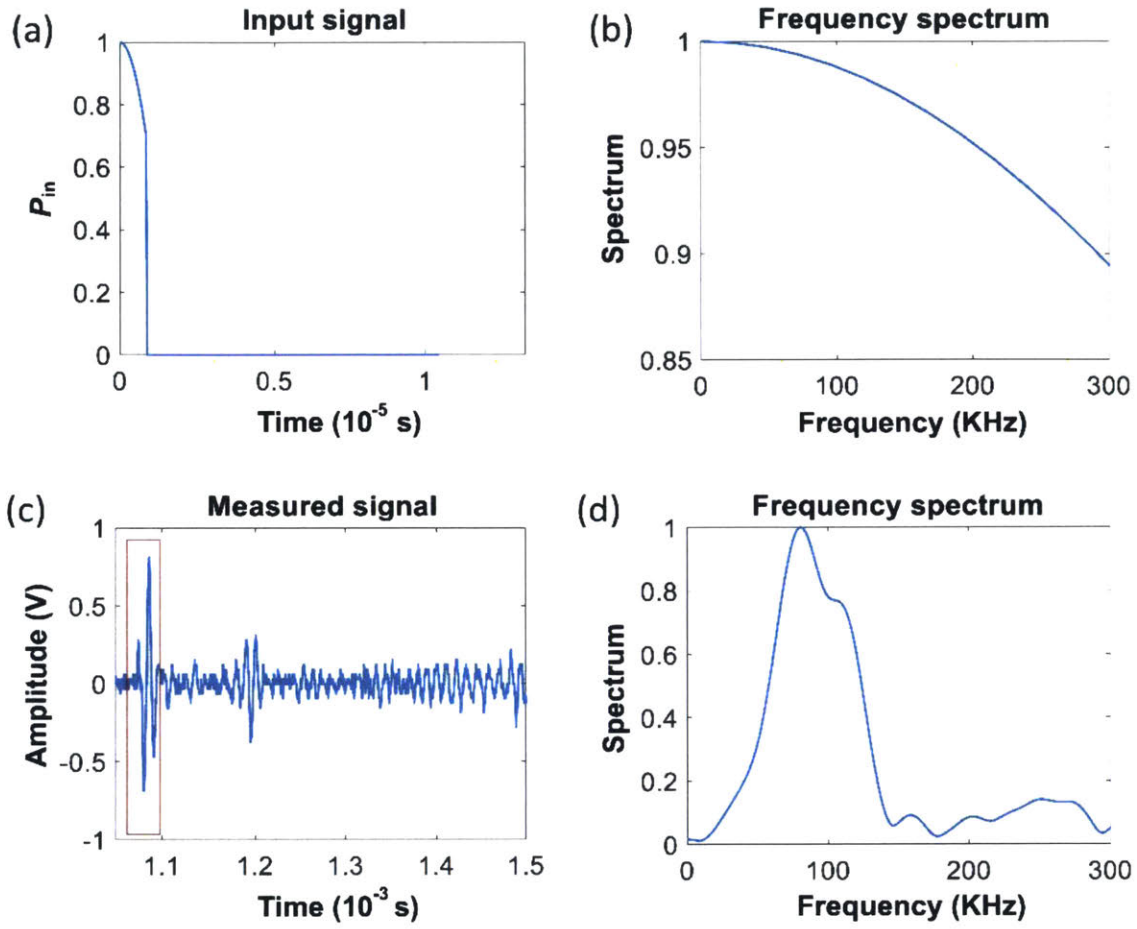

Figure 3-7: Measurements for $[50, 150]$ KHz frequency range. (a) Time domain waveform of input signal. (b) Frequency spectrum of input signal. (c) An example of received signal. The region inside the red rectangle is the time windowed signal. (d) Frequency spectrum of time-windowed measured signal.

3.6.3 COMSOL simulation on underwater acoustic transmission of the meta-gel.

The underwater acoustic transmission of the meta-gel was investigated in COMSOL Multiphysics based on the multiple scattering decomposition method. For example, the simulation model for the channel filling configuration water: air =1:2 was shown in Fig. 3-8. The hydrogel was described by a nearly incompressible Neo-Hookean material model, while the air and water were described by acoustic materials. Bulk

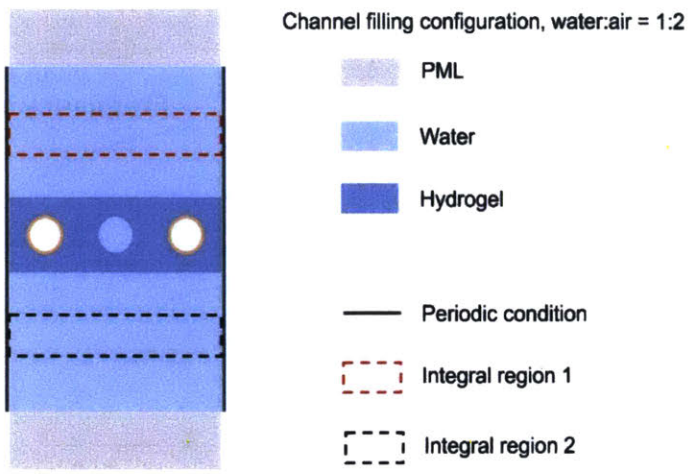

Figure 3-8: Simulation model in COMSOL based on the multiple scattering decomposition method.

modulus and shear modulus of the tough hydrogel [113, 121] was 2.21 GPa and 10.8 KPa, respectively and the acoustic velocity and density of water were 1466 m/s and 1000 kg/m^3, respectively. The air was considered to be non-dissipative, the acoustic velocity and density of which are assumed to be 343 m/s and 1.204 kg/m^3, respectively. The density and velocity of the liquid metal are taken as 6250 kg/m^3 and 2847 m/s, respectively [122]. Quadratic serendipity and quadratic Lagrange elements were used for solid and acoustic materials, respectively, with the largest element size smaller than one tenth of acoustic wavelength. The right and left ends of the metagel unit cell were set as periodic boundary condition, and all the interfaces between hydrogel and fluid (air and water) were set to be Acoustic-Structure Boundaries. The top and bottom sides of the simulation region were surrounded by perfectly matched layer (PML) Background pressure field was applied in the whole model to provide an incident sound pressure. Two integral regions were defined to obtain the transmission coefficient and reflection coefficient corresponding to each order. The jth order transmission coefficient and reflection coefficient were evaluated by $T_j = \int p_t \exp(ik_{jx}x + ik_{jy}y)ds/S_{\text{region1}}$ and $R_j = \int p_s \exp(ik_{jx}x - ik_{jy}y)ds/S_{\text{region2}}$, respectively, where p_t was the total acoustic pressure, p_s was the scattered acoustic pressure, S was the area of the integral region, $k_{jx} = 2\pi/(a \cdot j)$ and $k_{jy} = \sqrt{k_0^2 - k_{jx}^2}$ were wave vector components of the j^{th} order diffracted plane wave (a was the width

of the model and k_0 was the incident wave number). The total energy transmission coefficient and reflection coefficient were expressed as $TE = b_j T_j^2$ and $RE = b_j R_j^2$, where b_j was the ratio between k_{jy} and k_0.

3.6.4 Acoustic impedance of meta-gel and other composites calculated by effective parameter retrieving method

When the wavelengths of acoustic waves in water are larger than the feature sizes of our current design of meta-gel sheet, we can approximate the meta-gel sheet as a macroscopically homogeneous material. We calculate the effective acoustic impedance of meta-gel using combination of numerical simulation and the effective parameter retrieval method [119]. The meta-gel sheet with different channel dimensions was first investigated by using the Acoustic-Solid Interaction Module in COMSOL Multiphysics. A periodic super cell of meta-gel composites was placed in a 2D waveguide. Periodic boundary condition was set to the left and right boundaries of the super cell. A plane wave in designed frequency range was incident to the meta-gel sheet filled with water and the reflection field R0 and transmission field T0 were recorded. The acoustic impedance of the material was then calculated as $Z = \pm\sqrt{\frac{(1+R_0)^2-T_0^2}{(1-R_0)^2-T_0^2}} Z_{\text{water}}$, following the effective parameter retrieving method [119], where is the acoustic impedance of the water (Table 3.1). The sign was determined by requiring that the real part of the impedance be positive. The real part of the Z was compared with acoustic impedance of other materials. During the calculation, the thickness of the meta-gel layer is set to be identical to the diameter of the channel. The other pure hydrogel part is neglected since the acoustic properties of hydrogel was identical to that of water. Normalized impedance is defined as the ratio of acoustic impedance of meta-gel to that of water. The acoustic impedance of water is $1466 \times 10^3\ Pa \cdot s \cdot m^{-1}$. Normalized impedances for different channel dimensions and filling materials are plotted in Fig. 3-9.

The densities and sound velocities of different materials including solid, liquid and gas were listed on Table 3.1, Table 3.3 and Table 3.2. The acoustic impedances of the materials were then calculated as the product of the density and sound velocity.

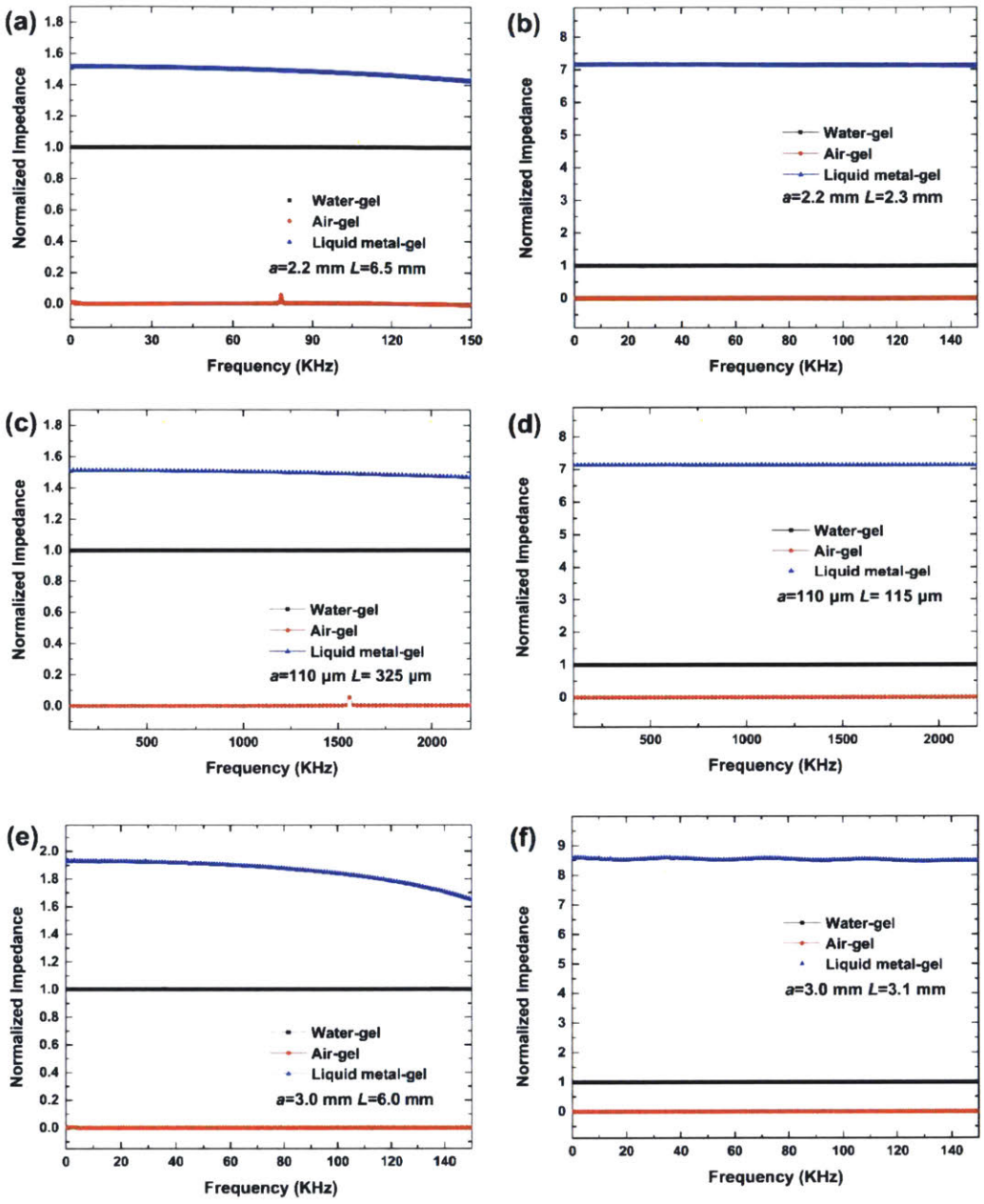

Figure 3-9: Normalized impedance (Z/Z_{water}) of different meta-gel sheets filled by water, air and liquid metal. The acoustic impedance of water is 1466×10^3 Pa s m^{-1}.

3.7 Summary

In this work, we use tough hydrogels with designed patterns of channels filled with air, water or liquid metal to achieve tunable acoustic properties that match those of air, water and soft solids over broadband frequencies. Besides the unprecedented broadband tunable acoustic transmission, the proposed meta-gel is also low-cost,

Table 3.1: Acoustic properties of solid [1]

Material	**Density** (Kg m^{-3})	**Acoustic impedance** (Pa s m^{-1} 10^3)
Fiberglass	1500	4110
Lucite	1180	3162
Nylon	1120	2912
Polyethylene	910	1892.8
Polystyrene	1030	2410
Acrylic (Perspex)	1190	3249
Polyvinylchloride, (PVC)	1390	3329
Silicone rubber	1100	1634
Wood	1000	3300-5000
Brick	1400-2400	5040-10080
Concrete	2400	7680-8880
Granite	1800-2600	10710-15470
Glass, Pyrex	1400-1800	7896-10152
bone	1912	7801
fat	952	1389
muscle	1080	1706
blood	1057	1665

Table 3.2: Acoustic properties of gas [1]

Material	**Density** (Kg m^{-3})	**Acoustic impedance** (Pa s m^{-1} 10^3)
Acetylene	1.092	0.359
Air	1.204	0.413
Ammonia (30°C)	0.717	0.315
Argon	1.661	0.511
Carbon monoxide	1.165	0.391
Chloroform (22°C)	2.994	0.461
Ethane	1.264	0.399
Ethylene (20°C)	1.26	0.412
Helium	0.1664	0.162
Hydrogen	0.0899	0.116
Hydrogen chloride	1.528	0.453
Hydrogen sulfide (24°C)	1.434	0.443
Neon (30°C)	0.899	0.4144
Nitric oxide (16°C)	1.249	0.4172
Nitrogen (29°C)	1.165	0.4129
Oxygen	1.331	0.4206

Table 3.3: Acoustic properties of liquid [1]

Material	**Density** (Kg m^{-3})	**Acoustic impedance** (Pa s m^{-1} 10^3)
Acetone	785	850
Benzene	874	958
Carbon Tetrachloride	1584	1446
Ethyl Alcohol	789	915
Gasoline	711	961
Glycerin	1259	2340
n-Hexanol	811	1057
Kerosene	820	1033
Motor oil	880	1531
Petrol	711	872
Octane	692	810
Oil (castor)	956	1425
Oil (lubricating)	900	1315
Phenol	956	1218
n-Propanol	804	970
Pyridine	979	1387
Toluene	867	1132
Turpentine	870	1079
Water	1000	1466
Sulfuric Acid	1838	2349
Seawater	1025	1549

environmentally friendly and compatible with human body. The method and material system reported here open new avenues to both design and applications of future acoustic materials. For example, while parallel channels of millimeter size have been adopted in the current meta-gel sheet, more sophisticated 2D or 3D channel patterns with finer features may lead to better tunability and/or broader range of acoustic properties. Other filler media such as silicone oil or glycerol may be explored for future meta-gels. The tunable impedance match of meta-gel with water and various soft solid materials over broadband frequencies will facilitate the development of new underwater acoustic devices and medical imaging devices.

Chapter 4

Far-field acoustic subwavelength imaging and edge detection based on spatial filtering and wave vector conversion

4.1 Introduction

Acoustic imaging techniques have been widely used in areas such as medical ultrasonic imaging [3], nondestructive testing [123], and underwater sonar systems [124, 125]. Similar to other wave-based imaging techniques, the high spatial frequency information of an object is carried by evanescent waves that decay exponentially as they leave the object. The loss of those evanescent waves in conventional imaging systems leads to the diffraction limit [74]. The working wavelength of acoustic imaging is relatively large compared to imaging techniques using other wave forms (e.g., optical wave, x-ray, electron beams, microwaves, etc.). Thus the resolution upper bound posed by the diffraction limit has larger impact on acoustic imaging. Various approaches have been developed to realize acoustic imaging beyond the diffraction limit [17, 18, 38, 39, 45, 46, 47, 49, 50, 75, 76, 77, 104, 126, 127].

The near-field scanning technique [75] is one of the earliest techniques for acoustic subwavelength imaging. Measurements have to be made in close proximity (fractions of wavelength) to objects in order to capture the evanescent components. This greatly limits its application. In the past decade, acoustic metamaterial based lenses have demonstrated the potential in subwavelength imaging [17, 18, 38, 39, 45, 46]. The dispersion relation and effective material properties were modified inside the metamaterials to support the propagation of evanescent waves. By coupling to acoustic metamaterial lenses in the nearfield of the objects, the evanescent waves can be measured further away from objects. Although the distance is extended through the use of existing acoustic metamaterials, the thermal viscous loss due to wave propagation in resonating elements is still a major constraint limiting the use of metamaterial-based lenses in subwavelength imaging.

If the evanescent wave can be converted to propagating wave and propagate in free-space or empty waveguide, the propagation distance will be much less limited by thermal viscous loss. Hyperlenses [47, 49] use cylindrical-shaped anisotropic metamaterials to couple and gradually compress large subwavelength wave vectors to small propagating wave vectors. At the exit of a hyperlens, image size is larger than wavelength and can be detected in the far-field. However, due to the geometric shape, higher spatial resolution of hyperlenses is at the cost of smaller field of view. The time reversal technique [50, 76, 77] uses random subwavelength scattering arrays to convert evanescent waves to propagating waves in the near field. In combination with time reversal mirror in the far-field, acoustic subwavelength focusing is realized. However, time reversal imaging is not a direct projection based technique. It requires a complex recording/playback system and the image needs to be formed at the same location as the object. Those requirements reduce the flexibility for applications. Far-field superlenses were designed in optics to realize far-field subewavelength imaging. They were designed by using gratings to convert optical evanescent waves to propagating waves [128, 129]. The converted propagating waves were measured in far-field free space and reconstructed computationally. In order to apply gratings to imaging, the overlapping of multiple diffraction orders needs to be addressed. In the design

of optical far-field superlens, the overlapping was removed by combining the grating with a metal layer that can excite subwavelength surface plasmon to couple selected spatial frequencies to the grating. However, no counterpart of surface plasmon exists in acoustics. Thus no such far-field superlens has been realized in acoustics yet.

In this work, we propose mechanisms in acoustics to realize the functions of optical surface plasma and grating, and combine them to demonstrate an acoustic far-field subwavelength imaging system. A resonator array (denoted as filter layer) of subwavelength unit cells is designed to realize the function of surface plasma in order to amplify selected subwavelength spatial frequencies. The acoustic binary phase grating [91] (denoted as grating layer) developed in Chapter 2, which has only even order diffraction, is designed to remove the incident propagating components and convert the incident subwavelength components to propagating ones. The combination of those two proposed structures forms the transmitter of the system, and establishes the one-to-one relationship between the subwavelength wave vectors and the propagating ones. Furthermore, instead of measuring the converted propagating wave directly and performing the back conversion in computer as implemented in the optical far-field superlens, we use a receiver that is spatially symmetrical to the transmitter to physically reconvert the propagating wave to the original evanescent wave in the far-field of the object, resulting in a reciprocal transmitting/receiving pair. In the proposed system, wave propagation will take place in empty waveguide with much less thermal viscous loss than in metamaterials. We will show that while the transmitter still needs to be close to the object, the receiver can be many wavelengths away from the object and the distance can be flexible. This is the reason why we call the designed system far-field lenses. Our system will work as spatial filters that separate different subwavelength spatial frequencies and project them to the far-field. Edge detection will be experimentally demonstrated as an example of far-field sub-wavelength imaging of our proposed system.

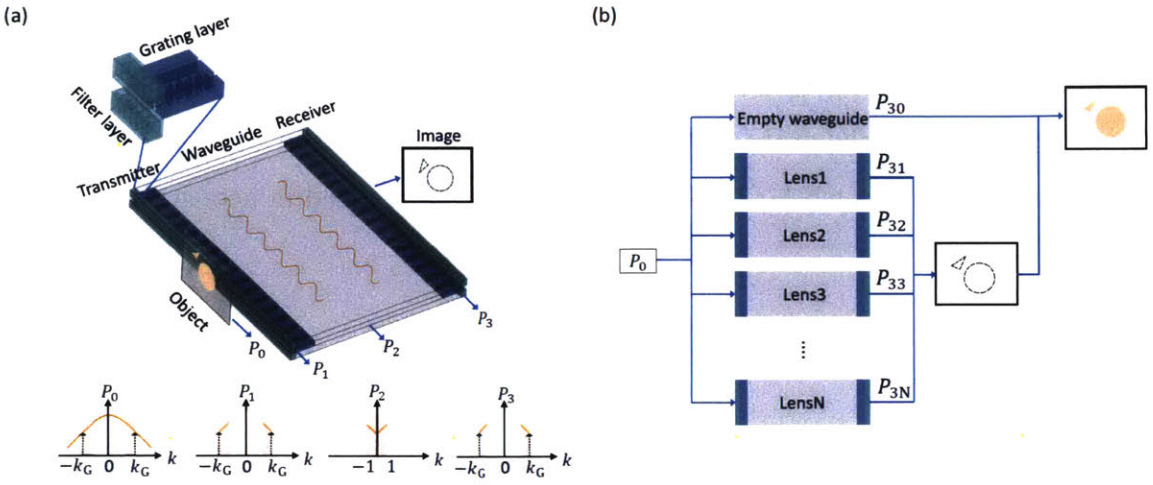

Figure 4-1: System schematics and the working process of the proposed acoustic far-field subwavelength imaging system. (a) System schematics. The whole system is composed of a transmitter and a receiver that are spatially symmetrical. Each part is composed of a filter layer (green) and a grating layer (blue). Evanescent wave $P_1 = \int_k p_1(k)\mathrm{e}^{j(kx-2\pi f_0 t)}dk$, where $|k| \in [k_\mathrm{G} - k_0, k_\mathrm{G}]$, will be filtered out by the filter layer from the scattered wave by the object $P_0 = \int_{-\infty}^{\infty} p_0(k)\mathrm{e}^{j(kx-2\pi f_0 t)}dk$, and be converted to propagating wave $P_2 = \int_{k'} p_2(k')\mathrm{e}^{j(k'x-2\pi f_0 t)}dk'$, ($k' = k - k_\mathrm{G} \in [-k_0, 0]$ when $k > 0$ or $k' = k + k_\mathrm{G} \in [0, k_0]$ when $k < 0$) by the grating layer in the transmitter. In the receiver, P_2 will be converted back to evanescent wave $P_3 = \int_k p_3(k)\mathrm{e}^{j(kx-2\pi f_0 t)}dk$. (b) Imaging process. By tuning the geometric parameters of filter layer and grating layer, different subwavelength spatial frequency bands of the scattered wave from object (P_0) can be separately projected to far-field (P_{3n}, $n = 1, 2, 3....$). The propagating band can be obtained by propagating through empty waveguide. The full subwavelength image can be obtained by summing up all the bands ($P_\mathrm{I} = \sum_{n=0}^{N} P_{3n}$). The edge of the object can be detected by adding up just the subwavelength components ($P_\mathrm{E} = \sum_{n=1}^{N} P_{3n}$.).

4.2 System model

Fig. 4-1a illustrates the system configuration that will enable the transmitter/receiver to faithfully convert evanescent wave to propagating wave and vice versa. As a proof of concept, the system is set in air with sound speed $c_\mathrm{air} = 343\mathrm{m/s}$. The object here is assumed to be acoustic scattering media with subwavelength details and is put in contact with the filter layer in the transmitter. The sound source emits continuous wave at frequency f_0 (corresponding to wavenumber k_0 in air) or a short pulse with center frequency f_0. The scattered sound wave from the object,

$P_0 = \int_{-\infty}^{\infty} p_0(k)e^{j(kx-2\pi f_0 t)}dk$, enters the filter layer in the transmitter. P_0 is expressed as the integration of the Fourier spectrum for the scattered wave from the object, based on the principle of spatial Fourier transform[130]. P_0 contains both propagating waves ($|k| < k_0$) and evanescent waves ($|k| \geq k_0$). The function of the filter layer is to amplify the wave components with a selected wavenumber band. After passing through the filter layer, the filtered wave is now $P_1 = \int_k p_1(k)e^{j(kx-2\pi f_0 t)}dk$, where $|k| \in [k_G - k_0, k_G]$ or $|k| \in [k_G, k_G + k_0]$ (In Fig. 4-1a we plot the former case.). $k_G = 2\pi/\gamma$ is the grating constant corresponding to grating period γ. The function of the grating layer is to convert the subwavelength wave vectors emerging from the filter layer to propagating wave vectors by momentum addition. After passing through the grating layer, P_1 will be converted to $P_2 = \int_{k'} p_2(k')e^{j(k'x-2\pi f_0 t)}dk'$. If $k > 0$, the conversion is through the -1st order diffraction of the grating and $k' = k - k_G$. If $k < 0$, the conversion is through the $+1$st order diffraction of the grating and $k' = k + k_G$. The grating is designed to only have odd diffraction orders, thus the propagating components from the filter layer, which is the zeroth order diffraction, is further suppressed. The receiver is composed of the same grating layer and the filter layer as the transmitter. By reciprocity, the receiver takes the reverse process. The grating layer first adds k_G to or subtracts k_G from k' to obtain $P_3 = \int_k p_3(k)e^{j(kx-2\pi f_0 t)}dk$. The amplitudes $p_1(k)$, $p_2(k')$ and $p_3(k)$ are derived in later sections as transmission coefficients of filter layers and grating layers. The grating will also generate other higher odd order diffractions (3th order, 5th order,...). Then the filter layer in the receiver will perform post-filtering for the waves with wave number $|k| \in [k_G - k_0, k_G]$ or $[k_G, k_G + k_0]$ in the first order diffraction. Other higher order diffractions are all attenuated after passing through the filter layer at the receiver. In order to prevent the overlapping of $+1$st and -1st diffraction orders of the grating layer, the wavenumber bands of the wave after passing through the filter layer cannot locate in $[k_G - k_0, k_G]$ and $[k_G, k_G + k_0]$ simultaneously. By changing the geometric parameters, the filtering band of the filter layer and the grating constant k_G of the grating layer can be adjusted to different locations in the spatial spectrum. Thus we can separately project the bands $|k| \in [nk_0, (n+1)k_0]$, $n = 1, 2, 3, 4, ...N$, to the far-field, as shown in Fig. 4-1b.

The received signals are denoted by P_{3n} respectively. The propagating waves with $|k| \in [0, k_0]$, denoted by P_{30}, will be obtained by wave propagating through an empty waveguide without transmitter/receiver. The final image can be formed in two ways. One way is summing up all the components together ($P_{\mathrm{I}} = \sum_{n=0}^{N} P_{3n}$). In this case, a full image with subwavelength details $|k| \in [0, (N+1)k_0]$ will be obtained. The other way is summing up only the subwavelength components ($P_{\mathrm{E}} = \sum_{n=1}^{N} P_{3n}$). In this case, the edge image of the object that is represented by higher spatial frequencies will be obtained. To demonstrate the concept in this work, we will show three different configurations that work for $|k| \in [k_0, 2k_0]$, $[2k_0, 3k_0]$, and $[3k_0, 4k_0]$.

4.3 Transmission properties of filter layer

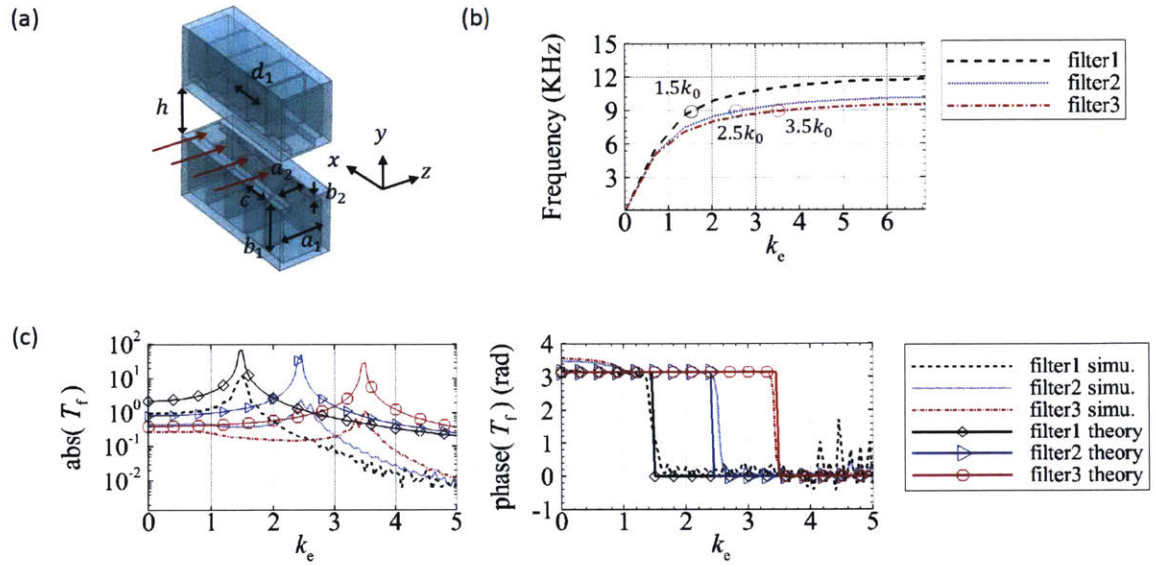

Figure 4-2: Model and properties of the filter layer. (a) Model for filter layer. The geometric parameters are: $b_1 = 5$ mm, $a_2 = 2.5$ mm, $c = 2.5$ mm, $b_2 = 0.75$ mm, $h = 5$ mm, and $d_1 = 2.75$ mm. By changing a_1, the filtered wave vector can be tuned. We choose $a_1 = 4.5$ mm for $k_e = 1.5$ (filter1), $a_1 = 6$ mm for $k_e = 2.5$ (filter2), and $a_1 = 6.5$ mm for $k_e = 3.5$ (filter3). (b) Theoretically calculated dispersion relations of filter1, filter2 and filter3 in the x direction. The dispersion relation curves of filter1, filter2 and filter3 pass through $k_e = 1.5$, $k_e = 2.5$ and $k_e = 3.5$ respectively at $f_0 = 9000$ Hz. (c) Amplitudes and phases of theoretically calculated and simulated transmission coefficients of filter layers.

The purpose of filter layer is to couple incident waves with specific wave numbers from input to output of the layer, as a near-field spatial filter. In optics, such filtering is realized through the excitation of surface plasma in a metallic layer. However, there is no counterpart of surface plasma in acoustics yet. We propose to realize the near-field spatial sound filtering by using two identical arrays of Helmholtz resonators (HRs) facing each other with distance h, forming a waveguide of height h for the wave to pass through (Fig. 4-2a). Here h is smaller than the wavelength λ_0 in free space to guarantee that the wave vector in y direction is zero. Each HR in the arrays is built with a cavity having widths a_1 and c, and height b_1, and a rigid tube having widths a_2 and c, and height b_2. The array period is d_1. The resonance frequency of the HR corresponds to a wavelength that is much larger than the size of the HR itself, so we can use lumped circuit model to approximate the HRs [2, 26], with the cavity acting as the capacitor and the tube acting as the inductor.

When the incident field propagates through the waveguide, some components with specific transverse wave numbers will be coupled to the resonance mode of the HR arrays. The HRs in the array should have much smaller sizes and periods compared to the working wavelength in order to make the coupling of subwavelength components possible. We choose our working frequency as $f_0 = 9000$ Hz, corresponding to wavelength of $\lambda_0 = 38.1$ mm, for demonstration. The proposed system can be scaled to other sizes and working frequencies depending on different applications. In the coordinate system shown in Fig. 4-2a, the incident field at the entrance of the filter layer has pressure distribution $p_{\text{in}} = \mathrm{e}^{ik_0k_{\text{e}}x}$, where $k_{\text{e}} = k/k_0$ is the effective wave vector in the x direction. The output pressure field distribution $p_{\text{out}} = p_1\mathrm{e}^{ik_0k_{\text{e}}x}$ along the x direction is obtained at the exit of the filter layer. The transmission coefficient of the filter layer, $T_{\text{f}}(k_{\text{e}})$, is defined as $T_{\text{f}} = p_{\text{out}}/p_{\text{in}}$. It is the coupling of wave component with effective vector k_{e} from the input to the output of the filter. The theoretical transmission coefficient is calculated using lumped circuit model.

When the unit dimension is much smaller than wavelength, the waveguide and the HRs can be represented by the lumped element model, as shown in Fig. 4-3.

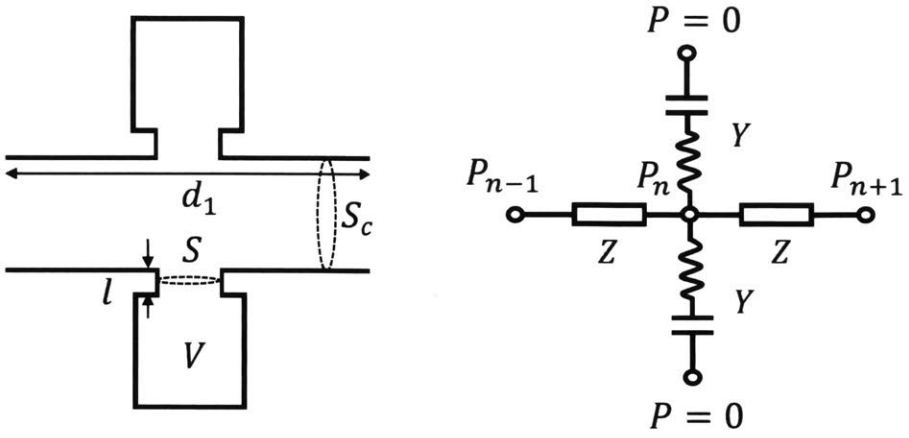

Figure 4-3: Lumped element model of Helmholtz resonator array

Following the method in [26], we have

$$\frac{\partial P}{\partial x} = \frac{ZU}{d_1} \tag{4.1}$$

$$\frac{\partial U}{\partial x} = \frac{ZYP}{d_1} \tag{4.2}$$

In the calculation, P is the averaged excess pressure, U is the volume velocity, $Z = jk_0 d_1 \frac{\rho c}{S_c}$ is the lumped element impedance of the waveguide, and $Y = -j/\left(\frac{\omega \rho l}{S} - \frac{\rho c^2}{\omega V}\right)$ is the admittance of the HR, $k = \omega/c$ is the wave number, $\omega = 2\pi f$ is the angular frequency, and f is the frequency. The system is assumed to be loss-free.

From Eq. (4.1), and Eq. (4.2),

$$jkP = \frac{Z}{d_1 U} \tag{4.3}$$

$$jkU = \frac{2Y}{d_1} P \tag{4.4}$$

We further get

$$\left(d_1^2\frac{\partial^2}{\partial x^2}+2YZ\right)P=0 \tag{4.5}$$

If sound source is distributed along the x direction in the waveguide between two HR arrays, Eq. (4.5) will have a source term on the right-hand side and becomes

$$\left(d_1^2\frac{\partial^2}{\partial x^2}+2YZ\right)P=s(x) \tag{4.6}$$

where $s(x)=s_0\mathrm{e}^{jk_ek_0x}$, and s_0 is a constant indicating the magnitude of the sound source. Then the pressure distribution in the waveguide of the filter layer is

$$P=\frac{s_0}{d_1^2k_e^2k_0^2+2YZ}\mathrm{e}^{jk_ek_0x} \tag{4.7}$$

The transmission coefficient is P/p_{in}:

$$T_{\mathrm{f}}(k_{\mathrm{e}})=\frac{s_0}{d_1^2k_{\mathrm{e}}^2k_0^2+2YZ}, \tag{4.8}$$

where s_0 is a constant indicating the strength of the coupling, Z is the effective impedance and Y is the effective admittance. Y and Z are functions of the geometric parameters of the HR arrays. In Eq.(4.8) and the expressions of Z and Y, $c=340$ m/s, $d_1=2.75$ mm, $S_c=W_1h$ is the cross-sectional area of the waveguide perpendicular to x direction, where W_1 is the size of the waveguide between the two HR arrays in the z direction, $h=5$ mm, $l=0.75$ mm, $S=a_2^2$ is the area of the HR neck tube, $a_2=2.5$ mm, $V=a_1b_1c$ is the volume of the HR cavity.

When the denominator $(d_1^2k_{\mathrm{e}}^2k_0^2+2YZ)$ approaches zero, the resonance occurs and the transmission through the waveguide between the HR arrays is largely enhanced. Eq. 4.8 is derived based on the assumptions that no damping is considered and the array is infinitely long. This is comparable to eigenmode analysis. In real-

istic experiments or simulations, the arrays are of finite length and damping has to be considered, so that the transmission will not diverge. From $d_1^2 k_e^2 k_0^2 + 2YZ = 0$, we get $k_e = \sqrt{-\frac{2YZ}{d_1^2 k_0^2}}$, which determines the wave number that is amplified by the filter layer. By changing the cavity size a_1 of the HRs, we obtained that $k_e = 1.5$ for the filter layer with $a_1 = 4.5$ mm (denoted by filter1), $k_e = 2.5$ for the filter layer with $a_1 = 6$ mm (denoted by filter2), and $k_e = 3.5$ for the filter layer with $a_1 = 6.5$ mm (denoted by filter3). The theoretical calculation of s_0 in Eq. 4.8 needs multiple scattering theory and mode analysis for the waves inside HRs and the waveguides. Here instead, we use COMSOL full wave simulation to calculate s_0. Two HR arrays, each containing 90 HRs, are used in the simulation (see Methods section for detailed description of the COMSOL simulation). By matching the theoretical and simulated T_f at $k_e = 0$, we get $s_0 = 2.35$, 1.85 and 1.5 for three curves respectively.

For each $k_e \in [0, 5]$, the amplitudes and phases of both theoretical and simulated T_f for the three values of a_1 are plotted in Fig. 4-2c. Both theoretical and simulation results show that the amplitude is amplified at $k_e = -\frac{2YZ}{d_1^2 k_0^2}$. Neither case considers loss. The amplification obtained in the simulation is in general smaller than that in the theoretical calculation. It is because that in the simulation the filter layer has finite numbers of HRs, which is unable to produce the resonant amplitude that approaches infinity shown in the theoretical calculation for infinite structures. Both theory and simulation indicate a π phase shift before the resonance wave vector and zero phase shift after the resonance wave vector.

The dispersion relations of the filter layers in x direction for three different a_1 values are calculated from the eigenvalue of Eq.(4.5), which follows the equation

$$d_1^2 k_x^2 + 2YZ = 0 \tag{4.9}$$

Substituting the expressions of Y and Z, we get

$$k_x^2 = -\frac{2\omega}{d_1 S_c \left(\frac{\omega l}{S} - \frac{c^2}{\omega V}\right)} \tag{4.10}$$

The dispersion relations are plotted in Fig. 4-2b. The dispersion relation curve shifts to lower frequencies as a_1 increases, resulting in larger k_e corresponding to $f_0 = 9000$ Hz. By further increasing a_1, the filter layer can work for wave vectors larger than $3.5k_0$. The largest wave vector that can be accessed is determined by $k_e \leq \frac{\pi}{d_1 k_0}$, where d_1 is the period of the HR array. In our case, $d_1 = 2.75$ mm, so $k_e \leq 6.9$.

4.4 Transmission properties of grating layer

In our designed system, a grating layer is put next to the filter layer to convert the subwavelength wave to propagating wave. A grating usually has multiple diffraction orders. The key here is to establish a one-to-one relationship between the wave vectors before and after conversion. Observing the simulated transmission coefficients in Fig. 4-2b, we find that the propagating wave components ($k_e \in [0, 1]$) are still large compared to the filtered subwavelength components, especially for filter layers of higher spatial frequencies. Those unwanted propagating waves will transmit through the grating layer by the zeroth order diffraction and overlap with the subwavelength components of interest that transmit by the first order diffraction. Acoustic binary phase grating developed in Chapter 2 does not have even order diffraction. Thus we propose to use acoustic binary phase grating to eliminate the zeroth order diffraction of the propagating components.

In Chapter 2, we developed the acoustic binary phase grating based on two waveguide channels with different wave path length. The two waveguide channels generate the π and 2π phase shift needed for the binary phase grating. Here, we construct the acoustic binary phase grating in our system with a straight channel of length 17.5 mm (around $\lambda_0/2$) and a curved channel with wave path length of around λ_0 but size

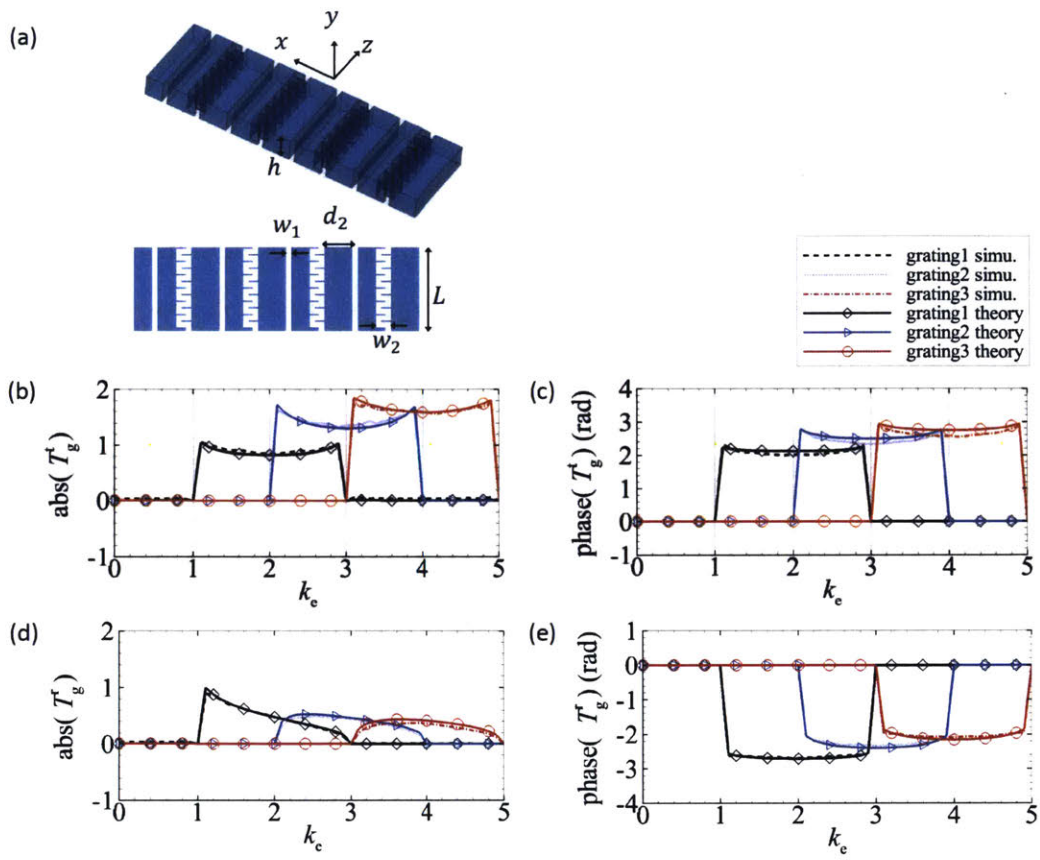

Figure 4-4: Model and properties of the grating layer. (a) Model for grating layer. Geometrical parameters are: $w_1 = 1.25$ mm, $w_2 = 6.95$ mm, $L = 18.75$ mm. Changing the grating period d_2 will results in different k_G. We choose $d_2 = 18.9$ mm for $k_G = 2k_0$ (grating1), $d_2 = 12.6$ mm for $k_G = 3k_0$ (grating2), and $d_2 = 9.4$ mm for $k_G = 4k_0$ (grating3). (b-c) Amplitudes (b) and phases (c) of theoretical and simulated transmission coefficients of grating layers in the transmitter. (d-e) Amplitudes (d) and phases (e) of theoretical and simulated transmission coefficients of grating layers in the receiver.

of 17.5 mm in the z direction, as shown in Fig. 4-4a. The width of the channels is 1.25 mm. The height of the channels, $h = 5$ mm in the y direction, is the same as the height of the waveguide between the two HR arrays.

For a binary phase grating with period $2d_2$, the grating constant is $k_G = \pi/d_2$. In Chapter 2, the first order diffraction is still propagating wave, with wave number smaller than $k_0 = 2\pi/\lambda_0$. Here we design the grating period d_2 such that the first order diffraction is at the subwavelength band that we want to convert to or convert from propagating band. The transmission coefficient $T_g^t(k_e)$ for the grating is defined

as the coupling efficiency from subwavelength components $k_e k_0$ to the propagating components $k_e k_0 - nk_G$ through the $-n$th order diffraction. $T_g^r(k_e)$ is defined as the coupling efficiency from the propagating components $k_e k_0 - nk_G$ to the subwavelength components $k_e k_0$ through the $+n$th order diffraction ($k_e \in [n-1, n+1]$, $n = 0, 1, 2, ...$). $T_g^t(k_e)$ and $T_g^r(k_e)$ are calculated with plane wave expansion method [97], which is described in Chapter 2. The waves inside the channels and at both sides of the grating are expressed as combinations of plane wave modes. The coefficients of different modes are computed by matching pressures and perpendicular velocities at the two interfaces of the grating.

In order to verify the theoretical approach, COMSOL full wave simulation is performed to calculate the $T_g^t(k_e)$ and $T_g^r(k_e)$ of the grating with size of 250 mm in the x direction (see the Methods section for detailed description of the COMSOL simulation). Fig. 4-4b-4-4e show the amplitudes and phases of the theoretical and simulated transmission coefficients $T_g^t(k_e)$ and $T_g^r(k_e)$ of the three phase gratings with different grating periods corresponding to $k_G = 2k_0$, $3k_0$, and $4k_0$ (denoted by grating1, grating2, and grating3, respectively). Both theoretical calculation and simulation show that the grating layer demonstrates large -1st and $+1$st order diffraction for efficient subwavelength/propagating wave vector conversion as well as near-zero zeroth order diffraction for removing the influence of propagating components in the incoming wave. $T_g^t(k_e)$ gives positive phase shifts and $T_g^r(k_e)$ gives negative phase shifts.

Smaller channel width w_1 will decrease the unit cell size in x direction, enabling larger k_G for converting larger subwavelength wave vectors to propagating wave vector range. However, a smaller channel width will generate more thermal viscous loss inside the channels. The choice of w_1 here is a trade-off among those factors at frequency 9000 Hz.

4.5 Image transfer function of the whole system

In the whole system shown in Fig. 4-1a, the receiver will reconvert the propagating waves converted from subwavelength waves by the transmitter back to the original

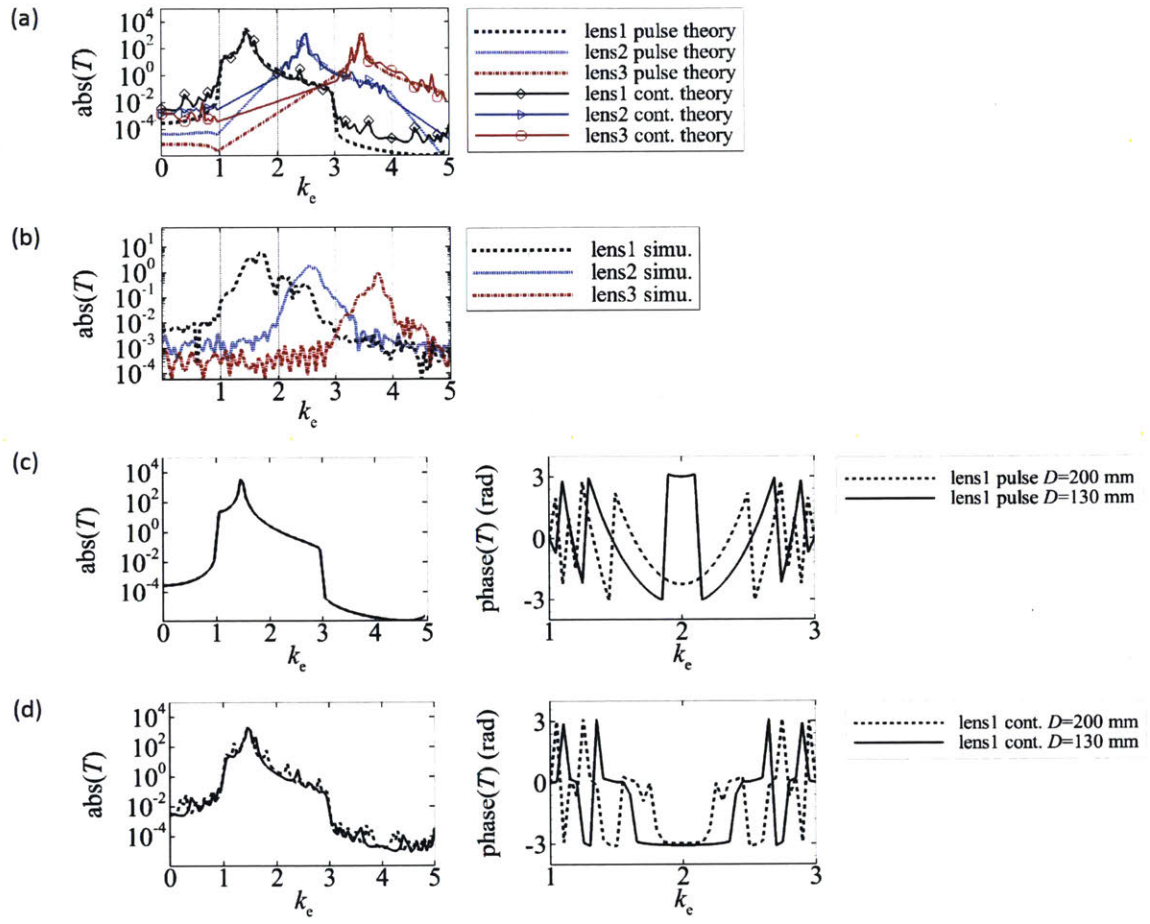

Figure 4-5: Transmission properties of the whole system. (a) Amplitudes of theoretically calculated image transfer functions of lens1, lens2 and lens3 for pulse source case and continuous source case. Lens1, lens2 and lens3 correspond to systems that work for wave vectors in $k_e \in [1,2]$, $[2,3]$, and $[3,4]$, respectively. (b) Amplitudes of simulated image transfer function of lens1, lens2 and lens3. Simulation is performed in frequency domain, taking into consideration the multiple reflections between gratings. (c) When using continuous source, theoretically calculated amplitudes and phases of image transfer functions for lens1 when $D = 130$ mm and $D = 200$ mm. D is the distance between the transmitter and the receiver. (d) When using pulse source, theoretically calculated amplitudes and phases of image transfer functions for lens1 when $D = 130$ mm and $D = 200$ mm.

forms. Three filter layer/grating layer combinations are considered: 1) $a_1 = 4.8$ mm, $k_G = 2k_0$, 2) $a_1 = 5.9$ mm, $k_G = 3k_0$, and 3) $a_1 = 6.5$ mm, $k_G = 4k_0$ (denoted by lens1, lens2 and lens3, respectively). The distance between the transmitter and the receiver is D in all three combinations. The waves propagate in empty waveguide of length D with negligible loss.

When calculating the transmission coefficient of the whole system (denoted as image transfer function), we need to consider two cases. One case is when continuous wave being used as the sound source. Multiple reflections between the two gratings need to be taken into consideration. In this case, the plane wave expansion method is applied to the combination of the two gratings and the space between them (see Methods section for detailed derivation). The calculated transmission coefficient for the combination of two gratings is denoted as $T_{\mathrm{g}}(k_{\mathrm{e}})$. The other case is when a short pulse being used as the sound source. Similar to 'single pass' of signals, all multiple reflections are neglected because their arrival time at the receiver does not overlap with the direct arrived signal. In this case, we only need to consider the phase delay in the empty waveguide from transmitter to receiver. The transmission coefficient of the two gratings and the space between is expressed as $D_{\mathrm{g}}(k_{\mathrm{e}}) = T_{\mathrm{g}}^{\mathrm{t}} T_{\mathrm{g}}^{\mathrm{r}} \mathrm{e}^{-jD\sqrt{k_0^2-(k_{\mathrm{e}}k_0-k_{\mathrm{G}})^2}}$, $k_{\mathrm{e}} \in [\frac{k_{\mathrm{G}}}{k_0}-1, \frac{k_{\mathrm{G}}}{k_0}+1]$.

The image transfer function can be expressed as $T_{\mathrm{continuous}} = T_{\mathrm{f}} T_{\mathrm{g}} T_{\mathrm{f}}$ (when using continuous source) or $T_{\mathrm{pulse}} = T_{\mathrm{f}} D_{\mathrm{g}} T_{\mathrm{f}}$ (when using pulse source), indicating the coupling strength of subwavelength wave component with effective wave vector k_{e} from the input side to the output side. When $D = 130$ mm $(3.4\lambda_0)$, the amplitudes of theoretically calculated $T_{\mathrm{continous}}$ and T_{pulse} for lens1, lens2 and lens3 are plotted in Fig. 4-5a. Since the transmission coefficient of the filter layer has a much larger magnitude than that of the grating layer near resonance, both amplitudes of $T_{\mathrm{continous}}$ and T_{pulse} are dominated by the trend of filter layer amplitude response. The image transfer functions of the three lenses are also obtained in COMSOL frequency domain simulation. Fig. 4-5b shows the amplitudes of the simulated image transfer functions. Fig. 4-5a and Fig. 4-5b both indicate that the subwavelength waves with wavenumber $k_{\mathrm{e}} \in [1,2]$,$[2,3]$, and $[3,4]$ are separately projected to the output of the receiver. The amplitudes of simulated image transfer functions are smaller than the theoretically calculated ones mainly because of the difference between theoretical and simulated amplitudes of the filter layer transmission shown in the previous section.

In order to study the influence of varying distance D, we plot the theoretically calculated amplitude and phase (Fig. 4-5c) of $T_{\mathrm{continous}}$ for lens1 ($a_1 = 4.8$ mm, $k_{\mathrm{G}} =$

$2k_0$) when $D = 130$ mm and 200 mm. From Fig. 4-5c we find that in continuous source case, whereas the multiple reflections between the waveguide generate small variations in the amplitude response, the major trend of band-filtering behavior does not change with distance D. However, changing D will result in large change in the phase response, unlike that in the amplitude response. The theoretically calculated amplitudes and phases of T_{pulse} for lens1 when $D = 130$ mm and 200 mm are also plotted in Fig. 4-5d. As indicated by the expression of $D_g(k_e)$, the amplitude does not change with D while the phase does. From above analysis, we conclude that changing D will only change phases of different wave vector components but not the amplitudes. With proper phase compensation, the distance between image and object can be changed flexibly without influencing the imaging quality.

4.6 Subwavelength imaging and edge detection

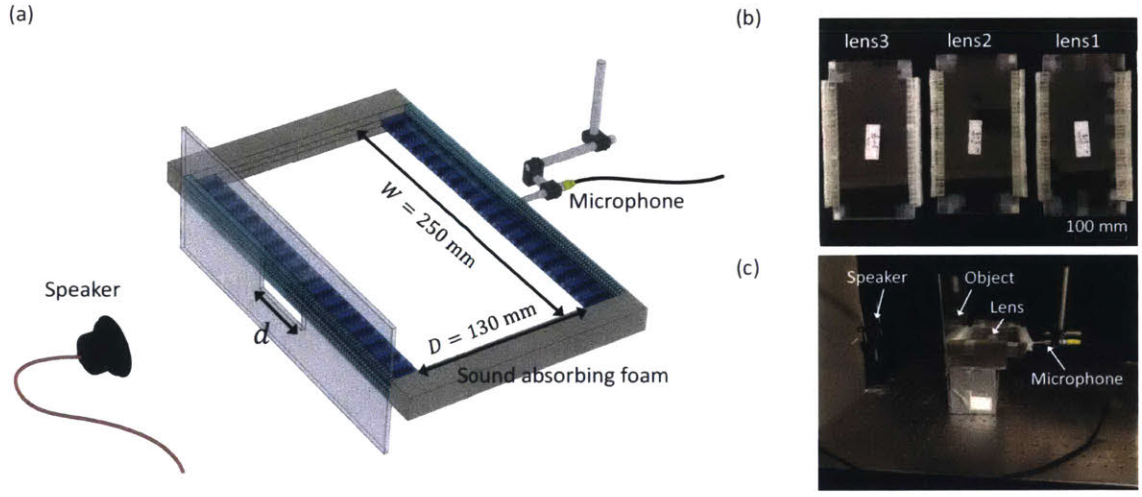

Figure 4-6: Experimental setup. (a) Experimental setup for subwavelength imaging and edge detection of 1-D slits. The speaker is 20 cm away from the lenses. The objects are 1-D slits put at the entrance of the transmitter. A microphone is used to scan the signal distribution at the exit of the receiver. (b) 3D printed lens1, lens2 and lens3. (c) A photo of the experimental system.

The designed far-field subwavelength imaging system has the ability to separate spatial frequency bands and project them to the far-field. Different spatial frequency

bands represent portions of the image with different spatial resolutions. By manipulating those separated bands, various functions can be realized. For example, if we add all the separated bands together, a full image of the object can be reconstructed with subwavelength details. If only the higher spatial frequency bands are added, edge detection of the objects can be achieved, which is an important function in image processing [131, 132, 133, 134, 135].

We use Autodesk Ember 3D Printer to fabricate the three sets of transmitting and receiving pairs lens1, lens2 and lens3 that work for $k_e \in [1,2]$, $[2,3]$, and $[3,4]$, respectively (Fig. 4-6). Each set is put into a waveguide of height $h = 5$ mm and width 250 mm to confine the converted propagating wave from the transmitter to the receiver. The propagating distance is $D = 130$ mm. We first use the fabricated system to image a 1D slit of size $d = 60$ mm ($1.57\lambda_0$). Four measurements are performed, three of which are from the three devices (lens1, lens2, lens3) corresponding to $k_e \in [1,2]$, $[2,3]$ and $[3,4]$. Another measurement is performed when the slit is put at the entrance of the same waveguide as the other measurements but without any of the HR arrays and gratings (len0), correspoinding to the propagating components $k_e \in [0,1]$. Each measurement gets the sound field distribution along the exit of the corresponding lens. Detailed measurement and data processing procedure are in the Methods section. Normalized spatial spectrums of the measured field distributions, $S'_n(k_e)$, $n = 0.1.2,3$, are plotted in Fig. 4-7a-4-7d as black solid lines. The measured spectrum of each lens verifies the spatial filtering capability of our designed system. From Fig. 4-7a-4-7d we also observe that all the other higher order diffraction components are at least 15 dB smaller than those in the 1st order diffraction after passing through the filter layer at the exit end.

The normalized space domain signals $I_n^p(x)$, $n = 0,1,2,3$ are obtained by taking inverse Fourier transform of the windowed spatial spectrums (See Methods) and plotted in Fig. 4-7e-4-7h. By adding all four normalized signals together, we get $I_{\text{full}}(x) = \sum_{n=0}^{3} I_n^p(x)$, which is a full image of the 60 mm slit, as shown in Fig. 4-7j. If we remove the diffraction limited component I_0^p , $I_{\text{edge}}(x) = \sum_{n=1}^{3} I_n^p(x)$ gives two edges of the slit having distance of 60 mm, as shown in Fig. 4-7i. Each edge is indi-

cated by a peak having half-width of around $\lambda_0/4$. The signal-to-noise ratio (SNR) is defined as the ratio of peak height at the edge to the second largest peak height within $[-\lambda_0, \lambda_0]$ distance of the edge (neglecting the peak height of the other edge in this range, if exists). SNR for the 60 mm slit edge detection is calculated as around 6 dB for both edges. The black dashed lines in Fig. 4-7 are COMSOL simulation results of spectrums and images corresponding to the experimental measurements.

We repeat the measurement process to obtain the I_1^{p}, I_2^{p}, and I_3^{p} of slits with sizes 30 mm ($0.8\lambda_0$), 15 mm ($0.4\lambda_0$), and 10 mm ($0.26\lambda_0$), and plotted the $I_{\mathrm{edge}}(x) = \sum_{n=1}^{3} I_n^{\mathrm{p}}(x)$ for the corresponding three slits in Fig. 4-8a-4-8c. The edges of 30 mm and 15 mm slits are successfully detected. The SNR of the 30 mm slit is 7.5 dB for the left edge and 8.1 dB for the right edge. The SNR of the 15 mm slit is 7.5 dB for the left edge and 5.7 dB for the right edge. However the system fails to detect the edges of the 10 mm slit, since the highest spatial frequency we can detect is less than $4k_0$, corresponding to feature size larger than $\lambda_0/4 = 9.5$ mm. 10 mm is almost the limitation of detection in the current system. In Fig. 4-8i, we only observe one peak of size around 10 mm, instead of two edges with 10 mm distance.We then use the four lenses to perform imaging for double-slit objects. One object is composed of one 20 mm ($0.52\lambda_0$) slit and one 30 mm ($0.8\lambda_0$) slit with 20 mm edge-to-edge distance. Another object is composed of two 10 mm ($0.26\lambda_0$) slits that have 10 mm edge-to-edge distance. We plot the experimental full images and edge images for the objects in Fig. 4-8d-4-8g. The four lenses successfully capture both the edges and the full image for the 20 mm-30 mm double slits. And as expected, our device gives the subwavelength image of the two slits but does not capture the edges due to the upper limit of wave vector range, which is $4k_0$. One can notice that the obtained images are not perfect square functions as the object, and the edges have widths of around $\lambda_0/4$ instead of being perfect pulses. Those imperfections are due to the fact that we only use four lenses to obtain spatial information up to $4k_0$. In order to fully recover the square images similar to the objects, more than four lenses that can recover deeper subwavelength information are necessary. The smaller or more complex the object is, the more spatial wave vector bands are needed in order to resolve the image.

In order to better evaluate the performance of the four lenses, we plot red dashed lines in Fig. 4-7e- 4-7j and Fig. 4-8 as theoretical references. Those red dashed lines are obtained with the corresponding $[0, k_0]$,$[k_0, 2k_0]$,$[2k_0, 3k_0]$,or $[3k_0, 4k_0]$ bands directly cut from the spatial Fourier transforms of the slits. For example, the red dashed line in Fig. 4-7f is obtained with the following steps: 1) Perform spatial Fourier transform for the 60 mm slits (a rectangular function with width 60 mm) to obtain the spectrum. 2) Use a window function to obtain the $[k_0,2k_0\ ]$ band from the spectrum. 3) Perform reverse Fourier transform for the windowed $[k_0,2k_0\ ]$ band to get the red dashed line in Fig. 4-7f showing the spatial field distribution of the $[k_0. 2k_0]$ band. We can see that the experimental outputs from the lenses are very similar to those theoretical references. The slight differences are due to the non-uniform transmission amplitudes for different wave vector components passing through the lenses. The non-uniform amplitudes are caused by non-uniform frequency response of the system for different wave vectors as well as different influence of damping on different wave vectors. The blue solid lines in Fig. 4-8 represent the diffraction-limited images from the empty waveguide (lens0), from which we can verify the resolution improvement by adding the signals from lens1, lens2 and lens3.

4.7 Discussion

The experimental results have successfully demonstrated that our designed system can separate and project different subwavelength spatial frequency bands to the far-field. The distance between image and object is largely extended compared to other subwavelength imaging systems based on negative index materials, Fabry-perot resonances, or trapped modes. The distance can now be many wavelengthes away and also be flexible according to application. Furthermore, the waveguide between the transmitter and the receiver in our system does not need to be straight as long as the height of the waveguide is smaller than the wavelength in free space. We can bend the waveguide according to the applications. The demonstrated system in this paper works in transmission mode. The system can also work in reflection mode,

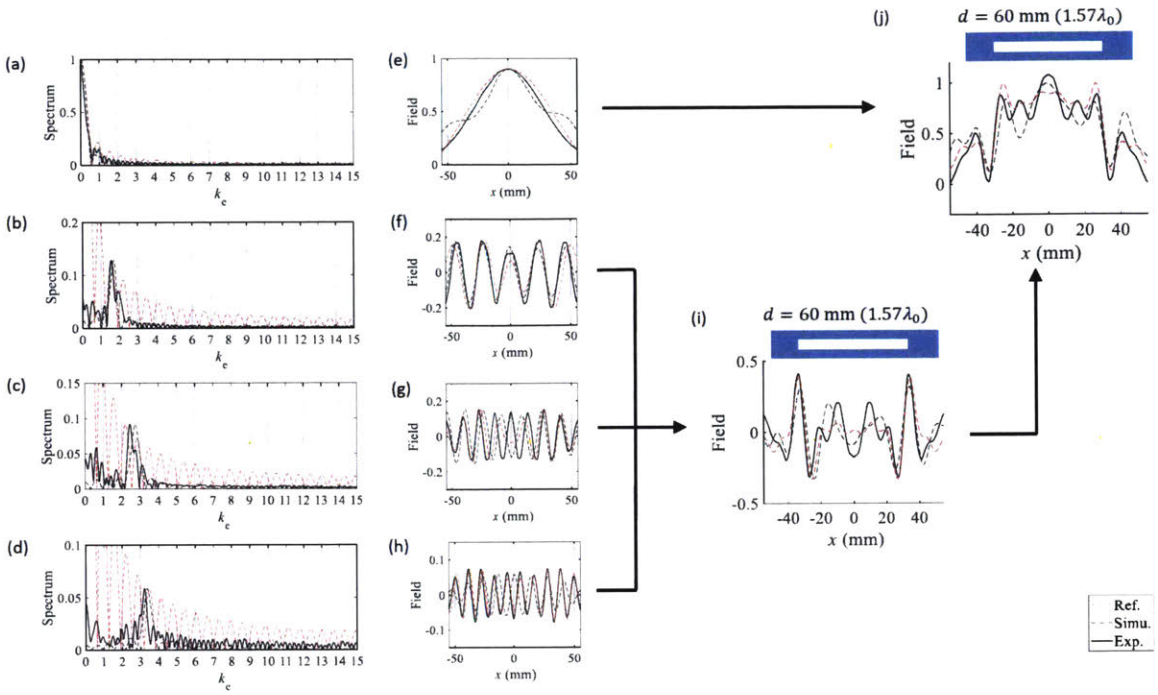

Figure 4-7: Subwavelength imaging and edge detection results of a 1-D 60 mm ($1.57\lambda_0$) slit. (a-d) When the object is a 60 mm slit, the normalized spatial spectrums of received signals from empty waveguide (a), lens1 (b), lens2 (c), and lens3 (d), respectively. (e-f) The reverse Fourier transforms of the shaded regions $k_e \in [0, 1]$ (e), $[1, 2]$ (f), $[2, 3]$ (g), and $[3, 4]$ (h) in the spectrum plotted in (a-d) correspondingly. (i) The edge image of the 60 mm slit by adding three subwavelength components. (j) The full image of the 60 mm slit by adding subwavelength as well as propagating components. In (a-j), black solid lines are experimental measurements, black dashed lines are simulation results, and red dashed lines are theoretical references.

where only one set of filter layer and grating layer combination is needed. The spatial symmetrical part can be performed by simply adding a reflecting mirror in the far-field. Another intriguing property of our system is that the transmitter and the receiver are symmetrical. An object can be put to either side to project the subwavelength information to the other side. With this symmetry, our system can be used as long distance acoustic communication system to exchange subwavelength information. Those tunabilities in the positions of object/image and the waveguide shape give our system unprecedented flexibilities compared to other far-field imaging systems such as hyperlenses and time reversal techniques.

There are several limiting factors for the spatial resolution of the system. The first

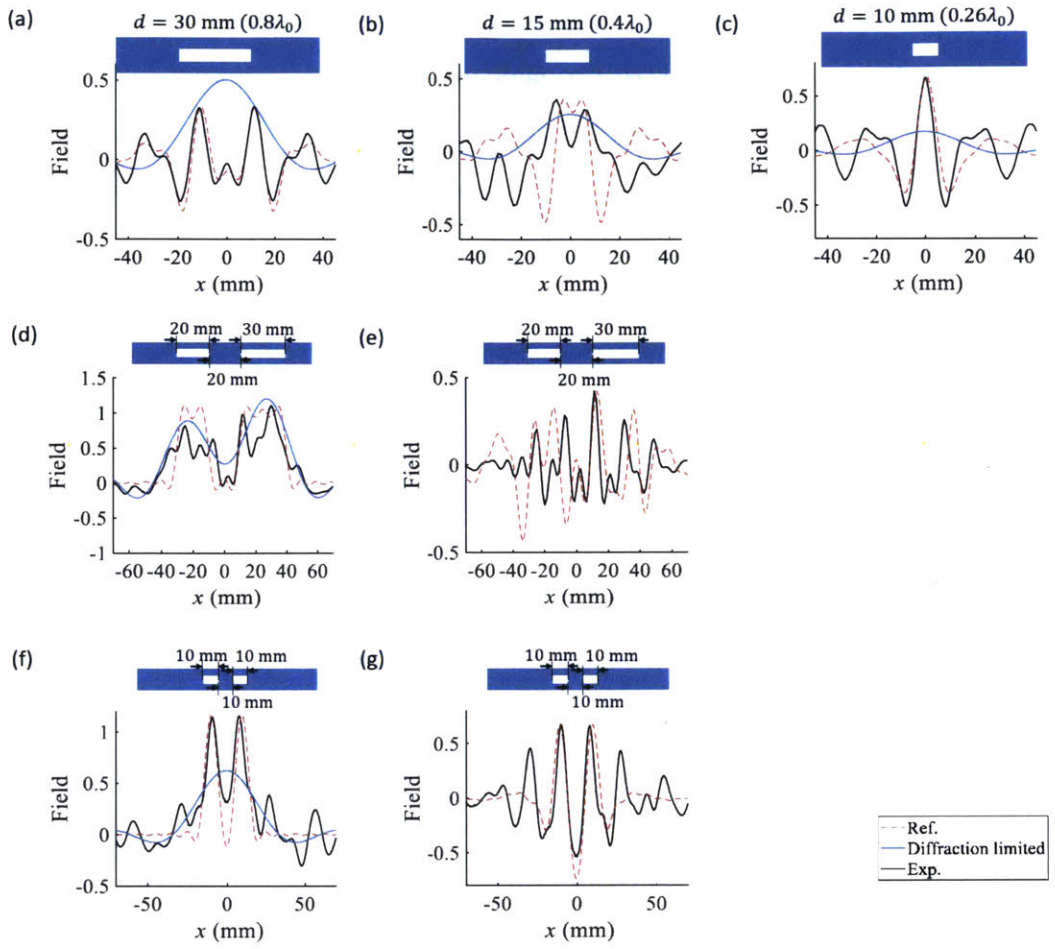

Figure 4-8: Subwavelength imaging and edge detection for 1-D single slits and double slits. (a-c) Edge images for a single slit of size 30 mm (a), 15 mm (b), and 10 mm (c), respectively. (d) The full image of a double-slit object with 20 mm and 30 mm slit widths and 20 mm edge-to-edge distance. (e) The edge image of the 20 mm-30 mm double slits. (f) The full image of a double-slit object with 10 mm and 10 mm slit widths and 10 mm edge-to-edge distance. (g) The edge image of the 10 mm-10 mm double slits. In (a-g), black solid lines are experimental measurements, blue solid lines are diffraction limited results from empty waveguide, and red dashed lines are theoretical references.

factor comes from the filter layer. As discussed earlier, the largest wave vector that can be amplified by the filter layer is limited by the periods of the filter layer, which is determined by the smallest size of Helmholtz resonators. However, smaller Helmholtz resonator size results in higher working frequency. Higher working frequency will further result in smaller wave vector range. In order to increase the spatial resolution, resonators in the filter layer should be able to generate lower resonance frequency

with smaller size. The second factor comes from the grating layer. The largest wave vector that can be converted back to propagating wave is determined by the grating period, which is limited by the smallest lateral size of each phase delay channel. The loss is another factor that will influence the resolution since higher spatial frequency components will be attenuated more by the thermal loss in each component.

Our work on the acoustic far-field subwavelength imaging system will lead to a number of directions that worth exploration in the future. For example, in the future, the current 1D line scanner type lenses can be expand to 2D to perform 2D subwavelength spatial filtering and edge detection. Currently, multiple lenses with different geometric parameters are needed for obtaining different spatial bands. In the future, tunable lenses can be designed such that the spatial filtering band can be adjusted in real-time. The working frequency of the current system is 9000 Hz, which is easy for demonstration in lab. In the future, the frequency range can be shifted to other applications' ranges by tuning the system size. In the current demonstration, the filter layer and the grating layer are built separately. In the future, if there is a way to combine the filter layer and the grating layer together, then the fabrication complexity will be largely decreased.

4.8 Methods

4.8.1 Experimental setup

As shown in Fig. 4-6a, the slit to be imaged is put in contact with the HRs in the transmitter (len1, lens2 and lens3) or the entrance of the empty waveguide (lens0). The left and right sides of the waveguide are covered by sound absorbing foam. A sound speaker located 20 cm (around five wavelengths) away from the slit sends eight periods of 9000 Hz sound wave. The wave incidents on the slit and the scattered wave from the slit enters the transmitter. At the receiver, a microphone (PCB 130F20) scans the sound field along the x direction at the exit of the HR arrays. The scanning has resolution of 1.25 mm and in total 180 points (22.5 cm) are scanned. At each

scanning point, 0.01 seconds (90 periods for wave of frequency 9000 Hz) of the sound wave is recorded.

4.8.2 Experimental data normalization

A time window of 10 periods is applied to each directly measured signal to obtain the portion of sound signal that comes from the imaging system in order to eliminate the interference of reflected wave from surrounding environment (the lab walls, table surface, etc.) and the multiple reflections inside the waveguides. By taking the time domain Fourier transform of the time-windowed signals, the complex values of the 9000 Hz components at all scanning points are obtained as $I_n(x)$, where $n = 0, 1, 2, 3$ (device number). Spatial Fourier transforms of $I_n(x)$ are obtained as $S_n(k_e)$,$n = 0, 1, 2, 3$. The 1-D spatial Fourier transform of a rectangular function of 60 mm width, $S_r(k_e)$, is used as reference for normalization (plotted as red dashed lines in Fig. 4-7a-4-7d). We normalize the amplitude of the measured spectrum $S_n(k_e)$ to the amplitude of the reference $S_r(k_e)$, and compensate for the phase variations of different wave vectors caused by passing through the system. Each $S_n(k_e)$ is divided by the factor $A_n = \frac{\max|S_n(k_e)|}{\max|S_r(k_e)|} e^{j\phi_n(k_e)}$, where $\frac{\max|S_n(k_e)|}{\max|S_r(k_e)|}$ is the ratio of the maximum amplitudes of $S_n(k_e)$ and $S_r(k_e)$ in the range $k_e \in [n-1, n+1]$, $n = 1, 2, 3$. The time windowed signal has 10 periods, which is shorter than the time needed for second arrival from waveguide internal reflection ($3D/c_{air}$). So $\phi_n(k_e)$ is the phase of image transfer function $T_{pulse} = T_f D_g T_f$ theoretically calculated for lens1, lens2, and lens3. When $n = 0$, $\phi_0(k_e) = e^{-j(D+2L+2a_1)\sqrt{k_0^2-(k_e k_0)^2}}$ ($k_e \in [-1, 1]$) is the phase profile after wave propagates through distant $D + 2L + 2a_1$ in an empty waveguide, where L is the length of the grating layer in z direction and a_1 is the size of the filter layer in z direction. The A_n calculated here using the slit of size $d = 60$ mm are stored and used as normalization factors for imaging processes of other slit sizes. The normalized spectrums are denoted by $S'_n(k_e)$, $n = 0, 1, 2, 3$. Multiplying $S'_n(k_e)$ with a rectangular function $R_n(k_e)(R_n(k_e) = 1$ when $|k_e| \in [n-1, n]$ and $R_n(k_e) = 0$ elsewhere) to eliminate the components outside the range $|k_e| \in [n-1, n]$, and performing the inverse spatial Fourier transform for $S'_n(k_e)R_n(k_e)$, we obtain the processed space

domain signal $I_n^{\mathrm{p}}(x)$,$n = 0, 1, 2, 3$.

4.8.3 Theoretical transmission coefficient of the two-grating combination, T_g

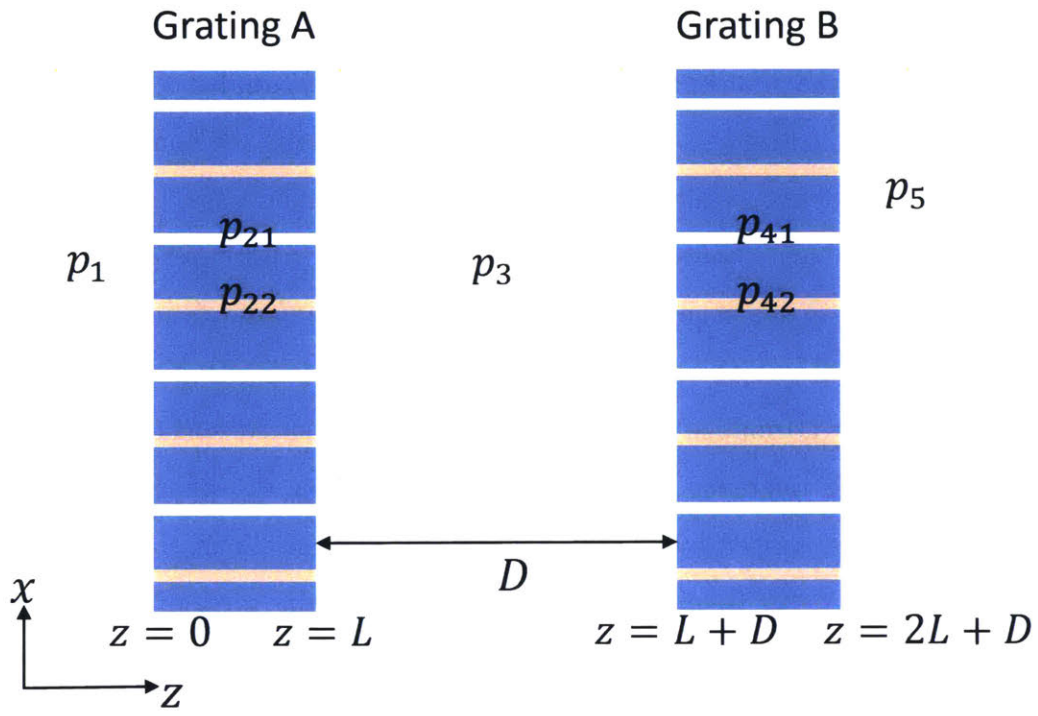

Figure 4-9: Model of two gratings with distance D.

In the double grating model shown in Fig. 4-9, the pressure field $p_{in} = \mathrm{e}^{-jk_{x_0}x}$ incidents onto the grating from left. So the pressure fields in areas separated by the boundaries of Grating A and Grating B are:

$$p_1 = \mathrm{e}^{j(-k_{x_0}x - k_{z_0}z)} + \sum_m R_m^a \mathrm{e}^{j(-k_{x_m}x + k_{z_m}z)}, \tag{4.11}$$

where $k_{x_m} = k_{x_0} + \frac{2\pi}{d}m$, $k_{x_m}^2 + k_{z_m}^2 = k_0^2$,

$$p_{21} = A_1 \mathrm{e}^{-jn_1k_0z} + B_1 \mathrm{e}^{jn_2k_0z}, \tag{4.12}$$

$$p_{22} = A_2 e^{-jn_1 k_0 z} + B_2 e^{jn_2 k_0 z}, \tag{4.13}$$

$$p_3(z = L) = e^{j(-k_{x_p} x)}(A_0 + B_0) + \sum_{m \neq p} T_m^a e^{j(-k_{x_m} x - k_{z_m}(z-L))}, \tag{4.14}$$

where p is the mode number when $|k_{x_p}| \leq k_0$,

$$p_{41} = A_3 e^{-jn_1 k_0 (z-L-D)} + B_3 e^{jn_1 k_0 (z-L-D)}, \tag{4.15}$$

$$p_{42} = A_4 e^{-jn_2 k_0 (z-L-D)} + B_4 e^{jn_2 k_0 (z-L-D)}, \tag{4.16}$$

$$p_5 = \sum_m T_m^b e^{j(-k_{x_m} x - k_{z_m}(z-2L-D))}. \tag{4.17}$$

Define new parameters $v_1 = A_1 - B_1$, $v_2 = A_2 - B_2$, $v_3 = A_1 e^{-jn_1 k_0 L} - B_1 e^{jn_1 k_0 L}$, $v_4 = A_2 e^{-jn_2 k_0 L} - B_2 e^{jn_2 k_0 L}$, $v_5 = A_3 - B_3$, $v_2 = A_4 - B_4$, $v_3 = A_3 e^{-jn_1 k_0 L} - B_3 e^{jn_1 k_0 L}$, $v_4 = A_4 e^{-jn_2 k_0 L} - B_4 e^{jn_2 k_0 L}$. By matching the pressure and perpendicular velocity at the four surfaces of the two gratings, we obtain the following expressions for v_1, v_2, v_3, v_4, v_5, v_6, v_7, v_8:

$$[H + \Lambda_1]v_1 + 2G^+ v_2 - \Gamma_1 v_3 = 2\text{sinc}\left(\frac{k_{x_0}}{2} w_1\right), \tag{4.18}$$

$$G^- v_1 + [2H + \Lambda_2]v_2 - \Gamma_2 v_4 = 2\text{sinc}\left(\frac{k_{x_0}}{2} w_1\right) e^{jk_{x_0}(-\frac{d}{2})}, \tag{4.19}$$

$$-\Gamma_1 v_1 + [H_p + \Lambda_1 + P_1]v_3 + \left[2G_p^+ 2P_1 e^{\frac{jk_{x_p} d}{2}}\right] v_4 - P_2 v_5 - 2P_2 e^{\frac{jk_{x_p} d}{2}} v_6 = 0, \tag{4.20}$$

$$-\Gamma_2 v_2 + \left[G_p^- + P_1 e^{\frac{-jk_{x_p} d}{2}} v_3\right] + [2H_p + \Lambda_2 + 2P_1]v_4 - P_2 e^{\frac{-jk_{x_p} d}{2}} v_5 - 2P_2 v_6 = 0, \tag{4.21}$$

$$-P_2v_3 - 2P_2\mathrm{e}^{\frac{-jk_{x_p}d}{2}}v_4 + [H_p + \Lambda_1 + P_1]v_1 + \left[G_p^+ + 2P_1\mathrm{e}^{\frac{jk_{x_p}d}{2}}\right]v_2 - \Gamma_1 v_7 = 0, \quad (4.22)$$

$$-P_2\mathrm{e}^{\frac{-jk_{x_p}d}{2}}v_3 - 2P_2v_4 + \left[G_p^- + P_1\mathrm{e}^{\frac{-jk_{x_p}d}{2}}\right]v_5 + [2H_p + \Lambda_2 + 2P_1]v_6 - \Gamma_2 v_8 = 0 \quad (4.23)$$

$$-\Gamma_1 v_5 + [H + \Lambda_1]v_7 + 2G^+ v_8 = 0, \quad (4.24)$$

$$-\Gamma_2 v_6 + G^- v_7 + [2H + \Lambda_2]v_8 = 0. \quad (4.25)$$

In those expressions, $\Gamma_1 = \frac{1}{j\sin(k_0L)}$, $\Gamma_2 = \frac{1}{j\sin(2k_0L)}$, $\Lambda_1 = \frac{\cos(k_0L)}{j\sin(k_0L)}$, $\Lambda_2 = \frac{\cos(2k_0L)}{j\sin(2k_0L)}$, $G^- = \sum_m \mathrm{e}^{jk_{x_m}(-\frac{d}{2})}\frac{a}{d}\frac{k_0}{\sqrt{k_0^2-k_{x_m}^2}}\mathrm{sinc}^2\left(\frac{k_{x_m}}{2}w_1\right)$, $G^+ = \sum_m \mathrm{e}^{jk_{x_m}(\frac{d}{2})}\frac{a}{d}\frac{k_0}{\sqrt{k_0^2-k_{x_m}^2}}\mathrm{sinc}^2\left(\frac{k_{x_m}}{2}w_1\right)$, $H = \sum_m \frac{a}{d}\frac{k_0}{\sqrt{k_0^2-k_{x_m}^2}}\mathrm{sinc}^2\left(\frac{k_{x_m}}{2}w_1\right)$, $G_p^- = \sum_{m\neq p} \mathrm{e}^{jk_{x_m}(-\frac{d}{2})}\frac{a}{d}\frac{k_0}{\sqrt{k_0^2-k_{x_m}^2}}\mathrm{sinc}^2\left(\frac{k_{x_m}}{2}w_1\right)$, $G_p^+ = \sum_{m\neq p} \mathrm{e}^{jk_{x_m}(\frac{d}{2})}\frac{a}{d}\frac{k_0}{\sqrt{k_0^2-k_{x_m}^2}}\mathrm{sinc}^2\left(\frac{k_{x_m}}{2}w_1\right)$, $H_p = \sum_{m\neq p} \frac{a}{d}\frac{k_0}{\sqrt{k_0^2-k_{x_m}^2}}\mathrm{sinc}^2\left(\frac{k_{x_m}}{2}w_1\right)$,

$P_1 = \frac{a}{d}\frac{k_0}{\sqrt{k_0^2-k_{x_p}^2}}\mathrm{sinc}^2\left(\frac{k_{x_p}}{2}w_1\right)\frac{\cos(k_{z_p}D)}{j\sin(k_{z_p}D)}$, $P_2 = \frac{a}{d}\frac{k_0}{\sqrt{k_0^2-k_{x_p}^2}}\mathrm{sinc}^2\left(\frac{k_{x_p}}{2}w_1\right)\frac{1}{j\sin(k_{z_p}D)}$, where $|k_{x_p}| \leq k_0$.

By solving those equation,s we can get v_1, v_2, v_3, v_4, v_5, v_6, v_7, v_8. Then the transmission coefficients (T_m) and reflection coefficients (R_m) are calculated as follows:

$$T_m^b(k_{x_0}) = \frac{a}{d}\frac{k_0}{\sqrt{k_0^2-k_{x_m}^2}}\mathrm{sinc}\left(\frac{k_{x_m}}{2}w_1\right)\left[v_7 + 2\mathrm{e}^{jk_{x_m}(\frac{d}{2})}v_8\right] \quad (4.26)$$

$$R_0^a(k_{x_0}) = 1 - \frac{a}{d}\frac{k_0}{\sqrt{k_0^2-k_{x_0}^2}}\mathrm{sinc}\left(\frac{k_{x_0}}{2}w_1\right)\left[v_1 + 2\mathrm{e}^{jk_{x_0}(\frac{d}{2})}v_2\right] \quad (4.27)$$

$$R_{m\neq 0}^a(k_{x_0}) = -\frac{a}{d}\frac{k_0}{\sqrt{k_0^2-k_{x_m}^2}}\mathrm{sinc}\left(\frac{k_{x_m}}{2}w_1\right)\left[v_1 + 2\mathrm{e}^{jk_{x_m}(\frac{d}{2})}v_2\right] \quad (4.28)$$

$T_g(k_e)$ is defined as T_0^b when $k_{x_0} = k_e k_0$.

4.8.4 COMSOL simulation setups

The pressure acoustics module in COMSOL Multiphysics 5.1 is used in all the simulations below. The background medium is air. The HRs, channels and the waveguides are all modeled as rigid walls (having infinitely large acoustic impedance).

Transmission coefficient of the filter layer

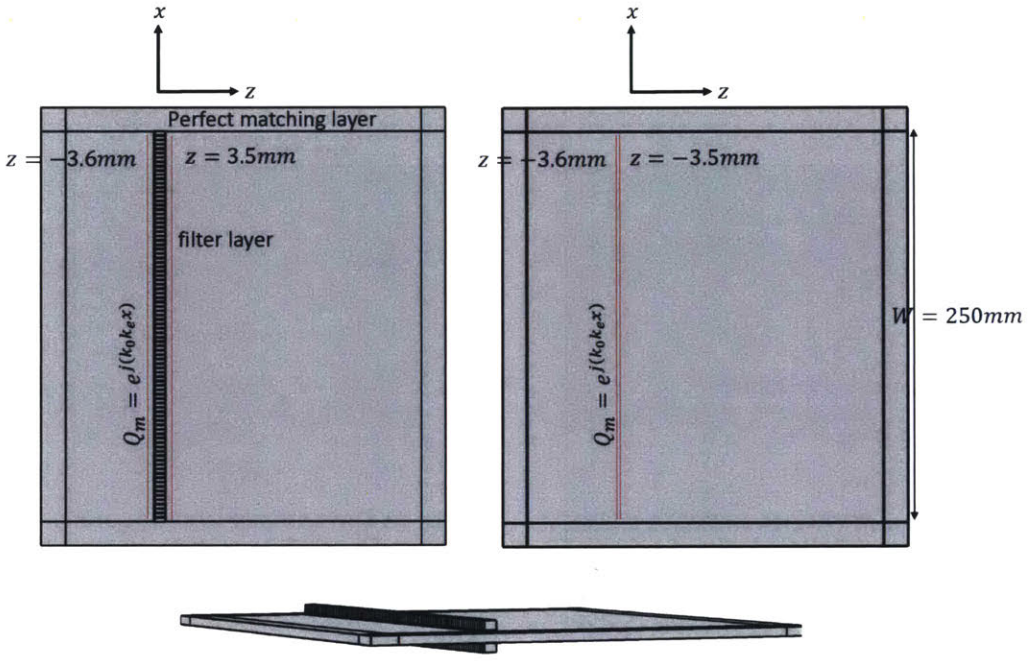

Figure 4-10: COMSOL simulation setup for filter layer

The filter layer is composed of two HR arrays. Each array has 90 Helmholtz resonators with period of 2.75 mm, resulting in a structure with size 250 mm in the x direction. A waveguide of height in y direction $h = 5$ mm and width in x direction $W = 250$ mm is inserted between the two HR arrays. The center of the HR arrays is placed at $z = 0$. The waveguide is surrounded by perfect matched layers. A monopole line source with distribution $Q_m = \exp[i(k_0 k_e x)]$ is set along the x direction at $z = -3.6$ mm. At frequency $f = 9000$ Hz, the pressure distribution along x direction at $z = 3.5$ mm is obtained through the frequency domain full wave simulation. For each input $k_e \in [0, 5]$, the spatial fourier transform of the output

pressure distribution is obtained and denoted by $p_{out}(k'_e, k_e)$, meaning the output pressure with wave vector k'_e when the input effective wave vector is k_e. The same monopole line source with distribution $Q_m = \exp[i(k_0 k_e x)]$ is set along the x direction at $z = -3.6$ mm of an empty waveguide and the spatial Fourier transform of pressure distribution at $z = -3.5$ mm is obtained as $p_{ref}(k'_e, k_e)$. The transmission coefficient of the filter layer, T_f, is defined as $T_f(k_e) = \frac{p_{out}(k_e,k_e)}{p_{ref}(k_e,k_e)}$.

Transmission coefficient of the grating layer

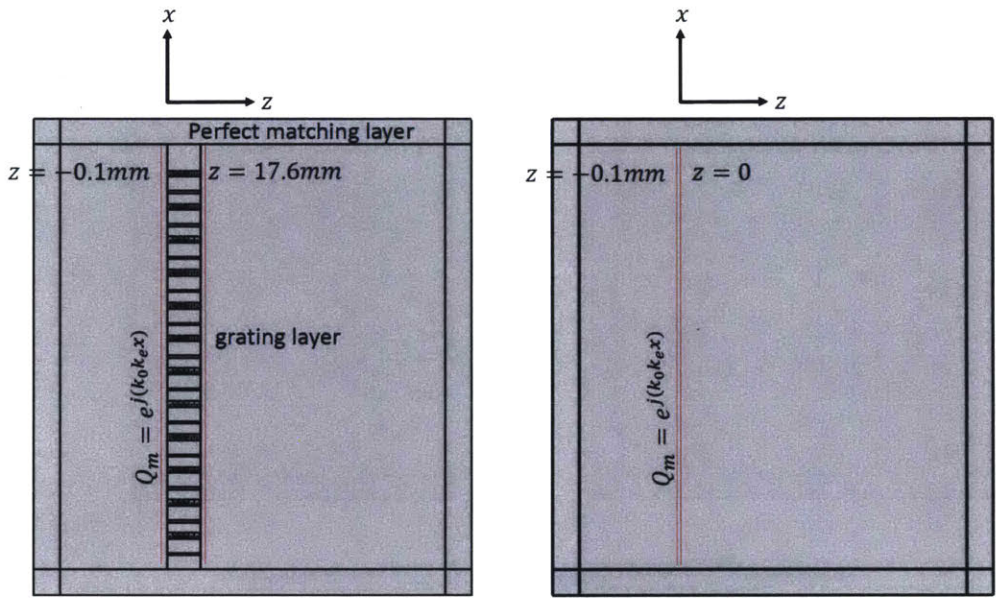

Figure 4-11: COMSOL simulation setup for a single grating layer

The grating layer is designed to have same size in x direction as the filter layer, which is 250 mm. For three different grating periods $d_2 = 18.9$ mm, 12.6 mm,and 9.4 mm, the number of π phase shifter and 2π phase shifter pairs is 13, 20, and 26. The grating layer is put into the same waveguide that is used for the simulation of filter layers. The entrance side of the grating is set at $z = 0$ mm. A monopole line source with distribution $Q_m = \exp[i(k_0 k_e x)]$ is set along the x direction at $z = -0.1$ mm. At frequency $f = 9000$ Hz, the pressure distribution along x direction at $z = 17.6$ mm (0.1 mm after the exit of the grating) is obtained through the frequency domain full wave simulation. For each input k_e, the spatial Fourier transform of

the output pressure distribution is obtained and denoted by $p_{out}(k_e', k_e)$, meaning the output pressure with wave vector k_e' when the input effective wave vector is k_e. The same monopole line source with distribution $Q_m = \exp[i(k_0 k_e x)]$ is set along the x direction at $z = -0.1$ mm of an empty waveguide and the spatial Fourier transform of pressure distribution at $z = 0$ mm is obtained as $p_{ref}(k_e', k_e)$. The transmission coefficients of the grating layer, T_g^t and T_g^r, are calculated as $T_g^t(k_e) = \frac{p_{out}(k_e - k_G, k_e)}{(p_{ref}(k_e, k_e)}$, $T_g^r(k_e) = \frac{p_{out}(k_e, k_e - k_G)}{p_{ref}(k_e - k_G, k_e - k_G)}$, where $k_e \in \left[\frac{k_G}{k_0} - 1, \frac{k_G}{k_0} + 1\right]$.

Transmission coefficient of the whole structure

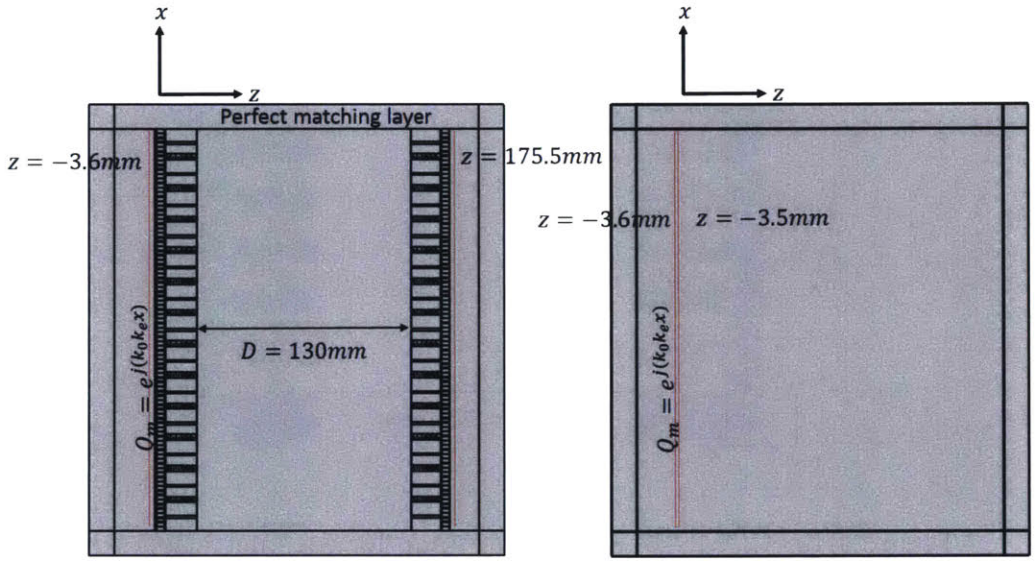

Figure 4-12: COMSOL simulation setup for the whole system.

In the simulation, the transmitting end and the receiving end are combined as a whole system and are placed in the same waveguide as previous simulations. The input plane is at $z = -3.6$ mm. The entrance of the grating layer in the transmitting end is at $z = 3.5$ mm. The distance between two gratings is 130 mm. and the output plane is at $z = 175.5$ mm. A monopole line source with distribution $Q_m = \exp[i(k_0 k_e x)]$ is set along the x direction at $z = -3.6$ mm. At frequency $f = 9000$ Hz, the pressure distribution along x direction at $z = 3.5$ mm is obtained through the frequency domain full wave simulation. For each input $k_e \in [0, 5]$, the spatial Fourier

transform of the output pressure distribution is obtained and denoted by $p_{out}(k_e', k_e)$, meaning the output pressure with wave vector k_e' when the input effective wave vector is k_e. The same monopole line source with distribution $Q_m = \exp[i(k_0 k_e x)]$ is set along the x direction at $z = -3.6$ mm of an empty waveguide and the spatial Fourier transform of pressure distribution at $z = -3.5$ mm is obtained as $p_{ref}(k_e', k_e)$. The transmission coefficient of the whole system, T, is defined as $T(k_e) = \frac{p_{out}(k_e,k_e)}{p_{ref}(k_e,k_e)}$.

Simulation of edge detection

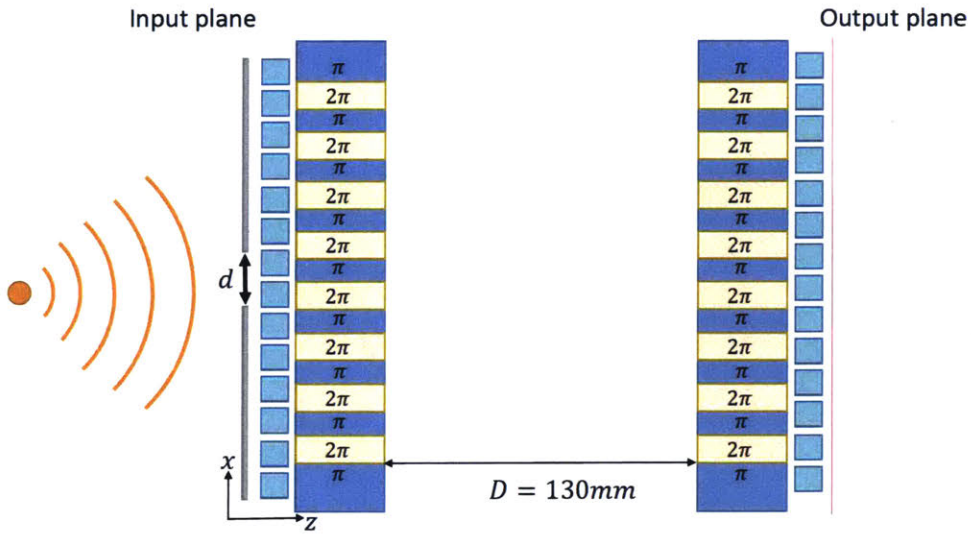

Figure 4-13: COMSOL simulation setup for edge detection.

Frequency domain COMSOL simulations are performed for the imaging process of the three devices and the empty waveguide. The slit with width d is put at the input plane. A point monopole source is put at 20 cm away from the slit. The simulation frequency is set at $f = 9000$ Hz. The spatial Fourier transform of the field along the transverse direction (x direction) at the detection plane are obtained as $F_n(k_e)$, $n = 0, 1, 2, 3$. $F_n(k_e)$ is normalized with $B_n = \frac{\max|F_n(k_e)|}{\max|S_r(K_e)|} e^{i\phi_n'(k_e)}$, where $\frac{\max|F_n(k_e)|}{\max|S_r(k_e)|}$ is the ratio of the maximum amplitudes of $F_n(k_e)$ and $S_r(k_e)$ in the range $k_e \in [n-1, n+1]$, $n = 1, 2, 3$. The simulation is implemented in the frequency domain. The multiple reflection between gratings is automatically included in the frequency response. So $\phi_n(k_e)$ is the phase of transmission coefficient $T_{continuous} = T_f T_g T_f$

theoretically calculated for lens1, lens2, and lens3. $\phi_0(k_e)$ is the phase delay for wave propagation in distance $D+2L+2a_1$, as in the experimental case. The inverse Fourier transforms of the normalized $\frac{F_n(k_e)}{B_n}$, which are denoted by $I_n^s(x)$.

4.9 Summary

In summary, we have designed and tested an acoustic subwavelength imaging system based on wave vector conversion. The combination of resonator arrays that enhance the waves with specific wave vectors, and binary phase gratings that add or subtract wave vectors by first order diffraction, establishes a one-to-one relationship between the subwavelength and propagating wave components. All theoretical, simulation and experimental data confirmed the capability our system in separating and projecting different subwavelength wave vector bands to the far-field of the object. We have demonstrated the application of our system with the edge detection of acoustic scattering objects with resolution upper limit of $\lambda_0/4$ and signal-to-noise ratio of ~ 6 dB. The system can be scaled to sizes of interest in ultrasonic medical imaging and non-destructive testing applications to increase the imaging resolution, and be applied to acoustic communication systems to increase the information capacity by incorporating subwavelength information.

Chapter 5

Subwavelength wave filtering/enhancement with low sound speed materials

5.1 Introduction

Acoustic wave is widely used in medical ultrasonic imaging and nondestructive testing owing to its non-radiative and noninvasive nature. The resolution of traditional acoustic imaging systems is limited to around half wavelength due to the loss of evanescent fields, which carry deep subwavelength details of the image. By increasing the working frequency, the resolution could be increased, but at the cost of decreasing penetration depth. Various approaches were proposed to increase the resolution without increasing working frequency [17, 18, 38, 39, 45, 46, 47, 49, 50, 75, 76, 77, 104, 126, 127]. The key to those approaches is to better collect the information carried by decaying evanescent fields [74].

Pendry, et. al. first brought up the idea of perfect lens with negative refraction [38]. In background medium of air (impedance $Z = Z_0$ and refractive index n=1), a slab of material with matched impedance $Z = Z_0$ and refractive index n=-1 can amplify the evanescent components and realize perfect image focusing. Negative

refractive index can be realized in phononic crystals with band folding of the dispersion curve due to Bragg scattering [136, 137, 138, 139, 140, 141, 142]. It can also be realized in metamaterials by having both negative effective mass density and negative effective bulk modulus at the same time [25, 27, 41, 66]. Later researchers found that the negative bulk modulus is not necessary. When the mass density is negative, the surface resonance state can be excited at the interface of positive/negative density materials and the evanescent wave can be amplified at the interfaces for subwavelength imaging [43].The subwavelength imaging devices using negative parameters are called superlenses. In acoustics, the negative density and negative bulk modulus are realized with locally resonant subwavelength structures, e.g. solid cores with elastic coating [21], Helmholtz resonators [26], membranes [143], soft porous material [28], or coiling-up-space waveguide channels [66], etc. Besides the superlenses with negative parameters, material with anisotropic parameters demonstrate cylindrical or hyperbolic dispersion relation shapes and support the propagation of subwavelength wave components. Materials with anisotropic material properties form the so-called hyperlenses for subwavelength imaging [47, 49, 144].

Can a slab of isotropic material with positive parameters be used for subwavelength imaging? The answer is yes. In [145], the authors proposed that the evanescent acoustic wave can be amplified by coupling to a material slab with slow sound speed. The multiple reflections between the two interfaces of the slab amplifies the decaying evanescent field. In [145], an initial theoretical derivation is developed for the enhancement of evanescent field based on the analogy with quantum mechanics. In our work shown in this chapter, the exact expression for acoustic wave transmission coefficient is derived based on acoustic wave equations. The influences of layer thickness, material properties, and damping factors are studied systematically. Full wave FEM simulation for the evanescent enhancement is also demonstrated.

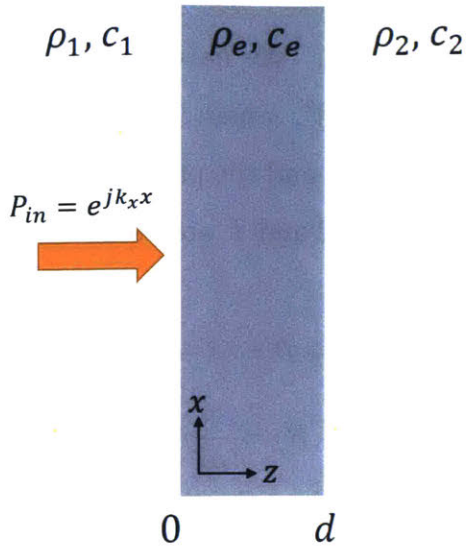

Figure 5-1: System model. Wave incidents the material slab of thickness d from left to right.

5.2 System model

Considering a slab of material of thickness d, density ρ_e, and sound speed c_e, placed between medium 1 (ρ_1, c_1) and medium 2 (ρ_2, c_2). A sound wave with pressure distribution along the interface of medium 1 and the slab, $P_{in} = e^{jk_x x}$, incidents on the interface at $z = 0$. k_x is the wave vector along x direction. The pressure in medium 1, medium 2 and the slab can be expressed as follows:

$$P_1 = e^{jk_x x}e^{-jk_{z1}z} + Re^{jk_x x}e^{jk_{z1}z}, \tag{5.1}$$

$$P_2 = Ae^{jk_x x}e^{-jk_{ze}z} + Be^{jk_x x}e^{jk_{ze}z}, \tag{5.2}$$

$$P_3 = Te^{jk_x x}e^{-jk_{z2}(z-d)}, \tag{5.3}$$

where R and T are the reflection and transmission coefficients of the wave passing through the slab. A and B are the coefficients representing the weights of wave traveling forward and backward inside the slab. In Eq. 5.1-5.3, k_{z1}, k_{z2} and k_{ze} are the vertical wave numbers in medium 1, medium 2 and the slab, respectively.

The transverse wave number k_x does not change at the interfaces of different media according to momentum reservation. We have $k_x^2 + k_{z1}^2 = (2\pi f/c_1)^2$, $k_x^2 + k_{z2}^2 = (2\pi f/c_2)^2$, and $k_x^2 + k_{ze}^2 = (2\pi f/c_e)^2$, where f is the frequency of the wave. By matching the velocities in z direction and the pressures at interfaces $z = 0$ and $z = d$, the following expressions for A, B, R and T are obtained:

$$1 + R = A + B \tag{5.4}$$

$$\frac{1}{\rho_1} jk_{z1}(1 - R) = \frac{1}{\rho_2} jk_{z2}(A - B) \tag{5.5}$$

$$Ae^{-jk_{z2}d} + Be^{jk_{z2}d} = T \tag{5.6}$$

$$\frac{1}{\rho_2} jk_{z2}(Ae^{-jk_{z2}d} - Be^{jk_{z2}d}) = \frac{1}{\rho_3} jk_{z3}T \tag{5.7}$$

From Eq. 5.4-5.7, we get the expression for T as:

$$T = \frac{2k_{z1}k_{ze}\rho_e\rho_2}{(k_{z1}k_{z2}\rho_e^2 + k_{ze}^2\rho_1\rho_2)\sin(k_{ze}d)i + (k_{z1}k_{ze}\rho_e\rho_2 + k_{ze}k_{z2}\rho_1\rho_e)\cos(k_{ze}d)};$$

5.3 Water/water interface

In this section, we consider the case when both medium 1 and medium 2 are water ($\rho_1 = \rho_2 = \rho_{water} = 1000$ kg/m^3, $c_1 = c_2 = c_{water} = 1500$ m/s). We assume the density of the slab is also $\rho_e = 1000$ kg/m^3. If the sound speed in the slab (c_e) is smaller than in water, some of the plane wave components with wave vector $2\pi f/c_{water} < k_x < 2\pi f/c_e$ is evanescent in the surrounding medium 1 and 2 but is propagative in the slab. The transmission of those evanescent wave components will be enhanced by the propagating modes inside the slab.

First, transmission coefficient T as a function of the incident normalized transverse wave vector $k_e = \frac{k_x c_{water}}{2\pi f}$ is calculated when the sound speed of the slab is assumed to be $c_e = 200$m/s (corresponding to refractive index $nr = 7.5$, if the refractive index of water is assumed to be $n_{water} = 1$) and the slab thickness is $d = 0.05\lambda$, where $\lambda = c_{water}/f$ is the wavelength of the wave in water.

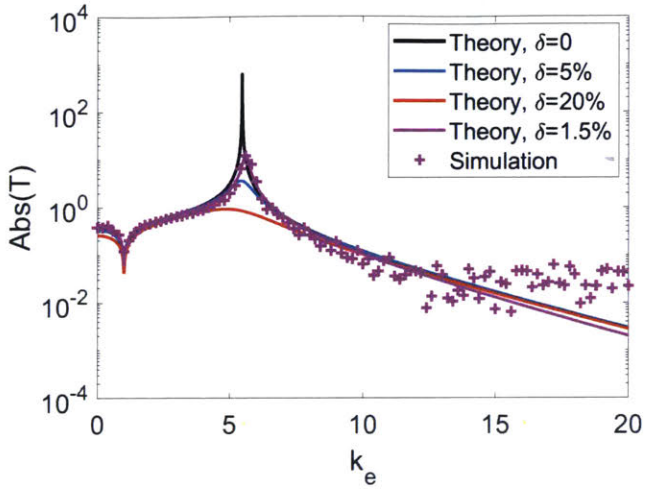

Figure 5-2: Transmission coefficients when $d = 0.05\lambda$, $c_e = 200$ m/s, $\rho_e = 1000$ kg/m^3, and medium 1 and medium 2 are both water.

In the calculation, we add thermal viscous loss to the slab by adding imaginary parts to the sound velocity and the density. So the expression for sound speed is $c_e' = c_e(1 + \delta i)$, and the expresison for density is $\rho_e' = \rho_e(1 - \delta i)$, where δ is defined as the damping coefficient. The transmission curves $T(k_e)$ when $\delta = 0$, 5%, and 20% are plotted in Fig. 5-2. We can clearly see the resonance peak at $k_e = 5.46$ and the gigantic transmission enhancement for wave vectors in the range around the resonance peak when $\delta = 0$. Those wave vectors correspond to evanescent waves in water. The resonance is induced by multiple reflections inside the slab. When increasing δ, the peak becomes lower and broader. Even when δ is as high as 20%, we still get transmission coefficient as high as 1 around $k_e = 5.46$, which is much larger than off resonance locations. Thus the slab of slow sound material works as a spatial filter for evanescent spatial components.

Next, we study the transmission enhancement when changing the slab thickness (d) and refractive index (nr) inside the slab. The T as a function of k_e and d is plotted in Fig. 5-3(a) when $\delta = 0$ and in Fig. 5-3(b) when $\delta = 5\%$. In those two plots, the refractive index of the slab is $nr = 7.5$. In the damping-free case shown in Fig. 5-3(a), the bright trajectories indicate the locations of resonance. When $k_e > nr = 7.5$, the wave inside the slab is also evanescent thus cannot generate any resonance in the

transmission. So there is no peak in the region $k_e > nr = 7.5$. For larger d, the T has resonance peaks at more locations of k_e. When there is damping, increasing d results in more loss in the transmitted energy. The transmission amplitudes drop to below unit value for $d > 0.6\lambda$ (as shown in Fig. 5-3(b) when $\delta = 5\%$). We also see that the trajectory of the resonance peaks are broadened. The T as a function of k_e and nr is plotted in Fig. 5-3(c) when $\delta = 0$ and in Fig. 5-3(d) when $\delta = 5\%$. In those two plots, the slab thickness is $d = 0.05\lambda$. Different nr values of the slab result in different k_e locations of the resonance peaks. When $nr < 1$, there is no enhancement for the evanescent field, because all the evanescent field in water is also evanescent in the slab if $nr < 1$.

5.4 Water/air interface

In this section, we consider the case when medium 1 is water and medium 2 is air ($\rho_1 = \rho_{water} = 1000$ kg/m^3, $\rho_2 = \rho_{air} = 1.29$ kg/m^3, $c_1 = c_{water} = 1500$ m/s, $c_2 = c_{air} = 1500$ m/s). The density of the slab is again assumed to be the same as water, $\rho_e = 1000$ kg/m^3. The wave incidents from the water side. The acoustic wave transmission through the water/air interface is known to be difficult due to the extreme impedance mismatch. By introducing a slab of material with sound speed slower than water, some of the evanescent components will be able to transmit through the water/air interface because of the multiple reflections between the two interfaces of the slab.

Transmission coefficient T as a function of the incident normalized transverse wave vector k_e is calculated for the same slab as in the previous water/water case ($c_e = 200$m/s and $d = 0.05\lambda$) for different damping factors $\delta = 0$, 5%, and 20% (Fig. 5-2). The transmission coefficient is below -30 dB for $k_e < 1$, because of the extreme impedance mismatch. There are two resonance peaks for evanescent wave $k_e > 1$. One is at $k_e = 3.64$, which is due to the multiple reflections inside the slab. Another one is at $k_e = 4.4$, which equals to c_{water}/c_{air}. This peak corresponds to the wave number for a plane wave propagating in air. Increasing the damping factor δ

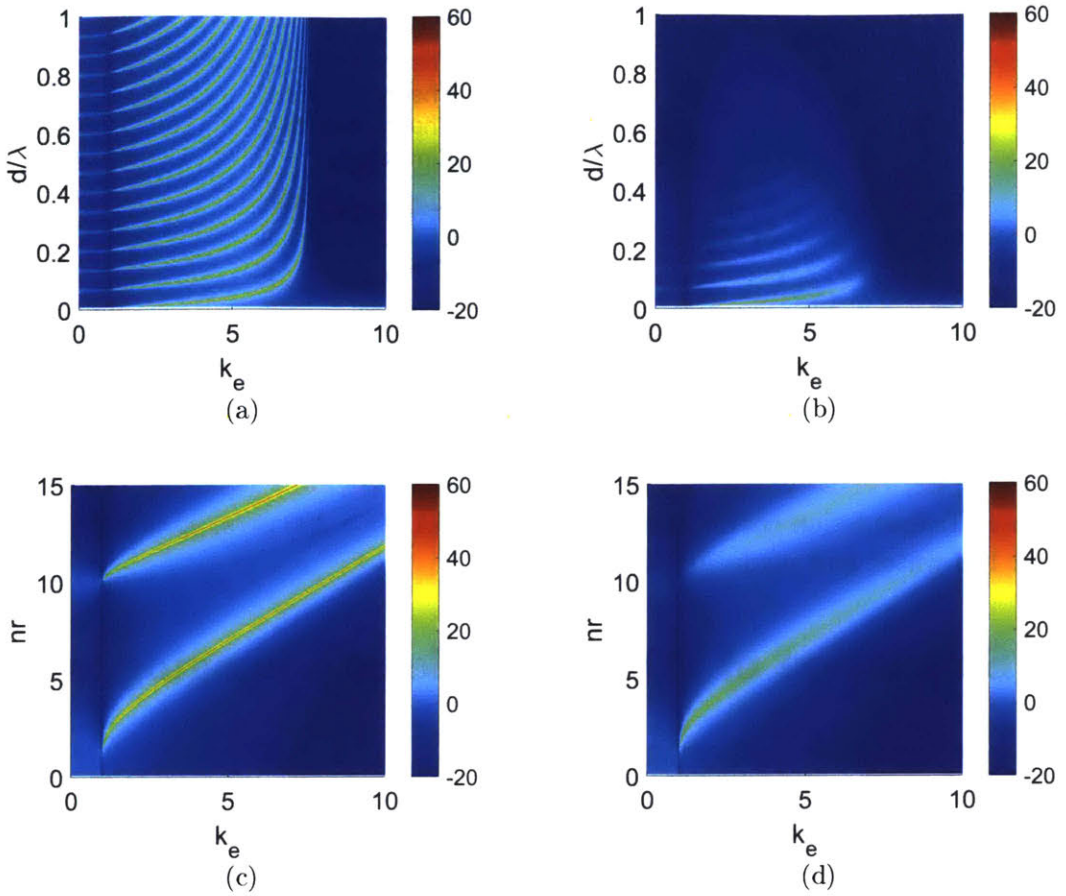

Figure 5-3: Transmission coefficient T as functions of different parameters when both medium 1 and medium 2 are water. (a-b) T as a function of incident transverse wave number k_e and slab thickness d when damping factor $\delta = 0$ (a) and $\delta = 5\%$ (b). (c-d) T as a function of incident transverse wave number k_e and slab refractive index nr when damping factor $\delta = 0$ (c) and $\delta = 5\%$ (d).

has more influence on the peak from multiple reflections. Although the transmission coefficient at resonance is still small, it is much larger than off resonance locations. Thus the slab of slow sound material can still work as a spatial filter.

The T as functions of k_e, d/λ, and nr at two different damping factors are plotted in Fig. 5-5 in the same way as in the previous section for water/water interface. The change of T when changing those parameters follows similar trend as in the previous case, except for the fact that there is a resonance peak at $k_e = c_{water}/c_{air} = 4.4$ that does not move when changing d/λ and nr.

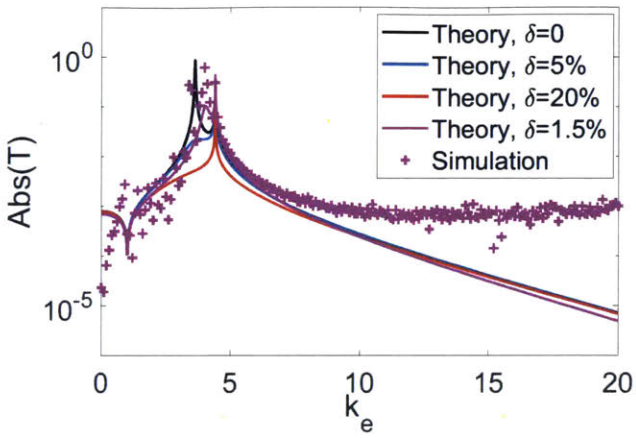

Figure 5-4: Transmission coefficients when $d = 0.05\lambda$, $c_e = 200$ m/s, $\rho_e = 1000$ kg/m^3. Medium 1 is water and medium 2 is air.

5.5 Simulation of 2D subwavelength imaging at water/water interface

Since the slow-speed slab can enhance certain band of evanescent wave, it can be used for subwavelength imaging. In this section, we simulated the subwavelengh imaging process with the same slab as the one used in the transmission coefficient calculation in the previous sections ($c_e = 200$ m/s ($nr = 7.5$), $\rho_e = 1000$ kg/m^3, $d = 0.05lambda$). The simulation is implemented with COMSOL. The material slab is put inside water, so medium 1 and medium 2 are both water. As shown in Fig. 5-6(a), the scattering object is put close to one side of the slab. The acoustic plane wave with frequency $f = 40$ KHz incident onto the object. The image plane is at the other side of the slab. The scattering object we want to image here is composed of two subwavelength beams, each with height of 5 mm and length of 20 mm, as shown in Fig. 5-6(b). The distance between the two beams is 5 mm.

The 2D transmission coefficient for different spatial frequency components (k_x and k_y) is plotted in Fig. 5-7. Since the 2D slab is isotropic in x-y plane, the 2D transmission coefficient is the rotation of 1D transmission coefficient shown in Fig. 5-2 around to the point $[k_x, k_y = [0, 0]$. The 2D transmission coefficient has a circular

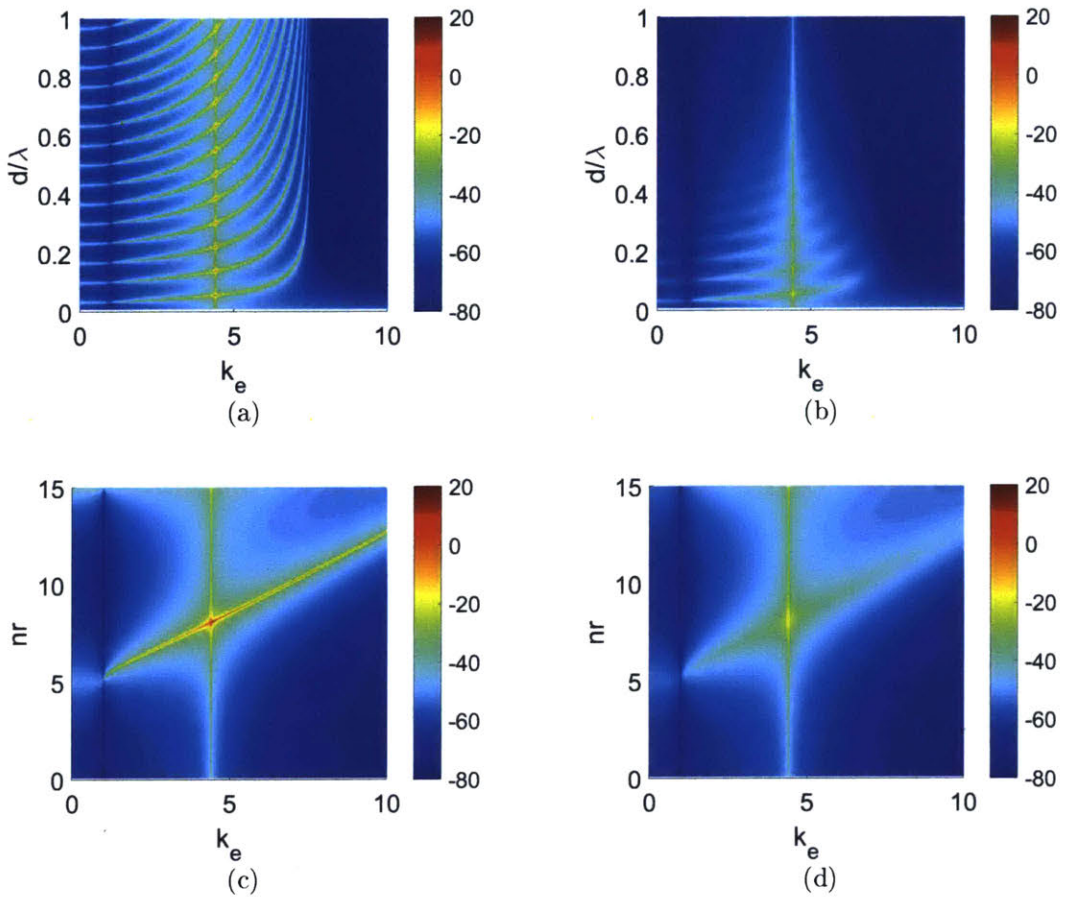

Figure 5-5: Transmission coefficient T as functions of different parameters when medium 1 is water and medium 2 is air. (a-b) T as a function of incident transverse wave number k_e and slab thickness d when damping factor $\delta = 0$ (a) and $\delta = 5\%$ (b). (c-d) T as a function of incident transverse wave number k_e and slab refractive index nr when damping factor $\delta = 0$ (c) and $\delta = 5\%$ (d).

peak at $\sqrt{k_x^2 + k_y^2} = 5.46$.

The subwavelength imaging process is shown in Fig. 5-8. When the slab is removed, the field distribution at the image plane is a blurred image only having the low spatial frequency information, as shown in Fig. 5-8(a). When the slab is put between the object and the imaging plane, the field distribution on the image plane is shown in Fig. 5-8(b). The high spatial frequency is transmitted through the slab. However, since different spatial components k_x and k_y undergo different phase delays, the output image is distorted. By compensating the different phase delays for different frequency components using the phase component in the theoretically derived

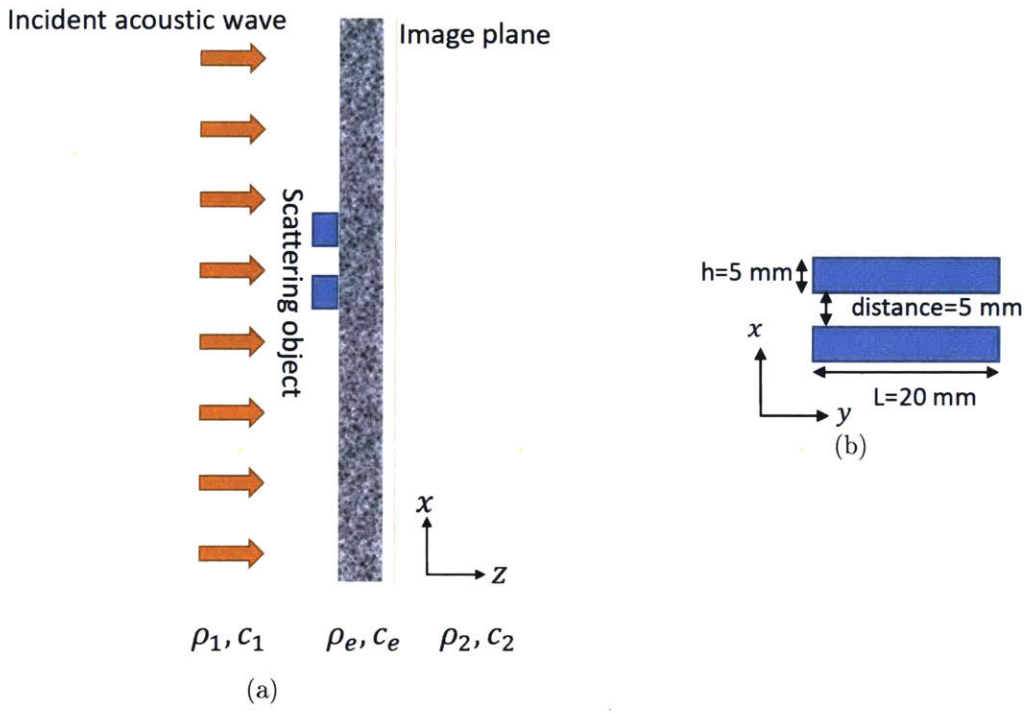

Figure 5-6: System schematics for simulation of subwavelength imaging. (a) System schematics. (b) Imaging object.

expression of T, we obtained the corrected field distribution on the image plane as shown in Fig. 5-8(c), which gives us recovered subwavelength image.

5.6 Summary

In summary, in this chapter, we developed the theoretical basis for the subwavelength spatial band filtering and enhancement using a slab of material with slow sound speed. The influence of parameters such as refractive index of the slab, the thickness of the slab, as well as the damping factor are studied systematically. We also apply the material slab to realize nearfield subwavelength imaging by combining the slab with a phase correction method based on the theoretical derivation of the transmission coefficient. Simulation results prove the effectiveness of the proposed subwavelength imaging method. The material slab with deep subwavelength thickness and slow sound speed can be used as the near-field spatial filtering component in future imaging systems, as well as replacing the filter layer developed in the previous chapter about

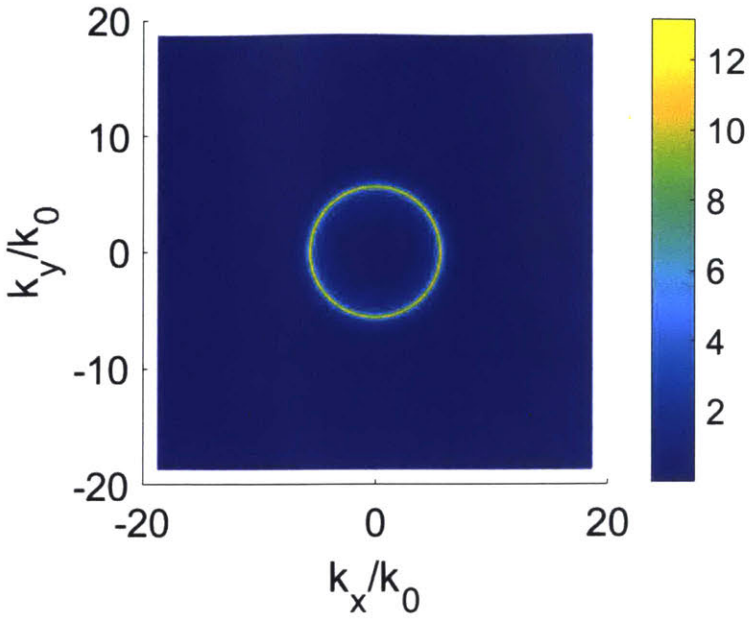

Figure 5-7: 2D Transmission coefficient when $d = 0.05\lambda$, $c_e = 200$ m/s, $\rho_e = 1000$ kg/m^3, and medium 1 and medium 2 are both water.

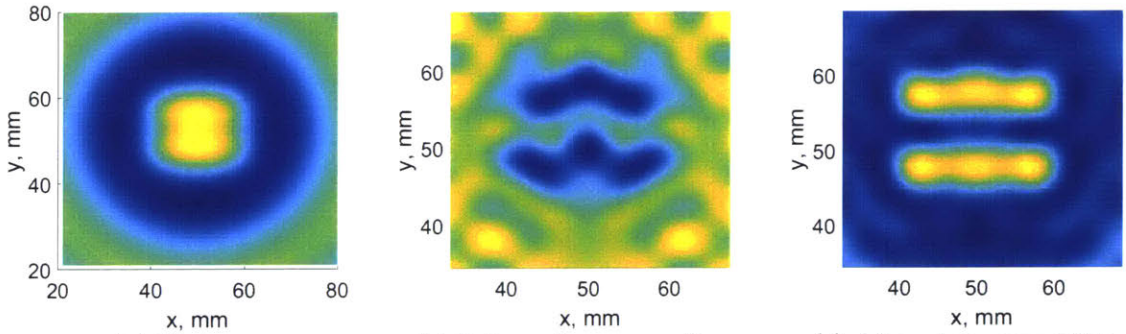

(a) No lens (b) Before phase correction (c) After phase correction

Figure 5-8: Subwavelength imaging process for an object composed of two beams with 20 mm length, 5 mm width, and 5 mm distance. (a) Image without the slab. (b) Image with slab before phase correction. (c) Image with slab after phase correction.

far-field subwavelength imaging system. The next step of this work is to find or fabricate materials that demonstrate slow sound speed. Potential candidates of such materials or structures could be polymers that demonstrate low sound speed, or porous structures such as sand and silicone rubber foam.

Chapter 6

Acoustic direction-selective transmission based on acoustic binary phase gratings

6.1 Introduction

Direction-selective transmission, or angular-selective transmission, is useful in applications such as directional sensing, energy harvesting, noise control, etc. The transmission of acoustic wave is angular dependent. Only waves in certain direction or directions are allowed to transmit through the structure, while waves in other directions are reflected or attenuated. Angular dependence of acoustic transmission can be observed when the wave is propagating through a slab of material that have different acoustic impedance from the surrounding background environment. At any given frequency, the impedance matching condition is satisfied only when the incident wave is at certain angle [146, 147]. However, this direction is frequency dependent. When frequency changes, the angle that wave transmits through the structure also changes. It is difficult to decouple the frequency dependence and angle dependence of wave transmission, and further realize broadband angle selection. In optics, there is an angle called Brewster's angle, at which light with a particular polarization

is perfectly transmitted through the interface between two materials, regardless of frequency. The concept of Brewster angle is utilized in both optics and acoustics to realize frequency-independent angle selection [52, 148, 149]. However, in those demonstrations, in addition to the Brewster angle, there are extended modes in other propagation directions. So the frequency dependence for angular selection still exists. In [150], the authors utilize the overlapping of bandgaps of photonic crystals to remove all the extended modes and experimentally demonstrated broadband angular selection in optics. The angular dependence and the frequency dependence of the wave transmission are successfully decoupled. The disadvantage of this work is that it requires hundreds of layers of different materials. In optics, since the wavelengths are relatively small, the total thickness of the structure is still tolerable. In acoustics, especially in low frequency range, the wavelength is relatively large. So the total thickness of the system is too big for fabrication and applications. Besides, once the structure is fabricated, it is difficult to tune the selected angle.

In this work, we propose a new way to realize broadband direction selection. Our system is composed of two layers of the binary phase gratings that can realize the frequency filtering and direction selection at the same time. The proposed double-grating structure removes the frequency dependence of the selected direction. Then the broadband direction selection can be achieved by stacking multiple layers of the double-grating structure. The direction of transmission can be tuned to anywhere in the range of $[0, 90°]$ by simply adjusting the distance between phase shifters in one of the gratings.

6.2 Direction-selective transmission based on wave number conversion

The direction-selective transmission is achieved with two layers of the previously designed acoustic binary phase gratings with different periods. The system utilizes the fact that evanescent wave does not carry any energy from one grating to another

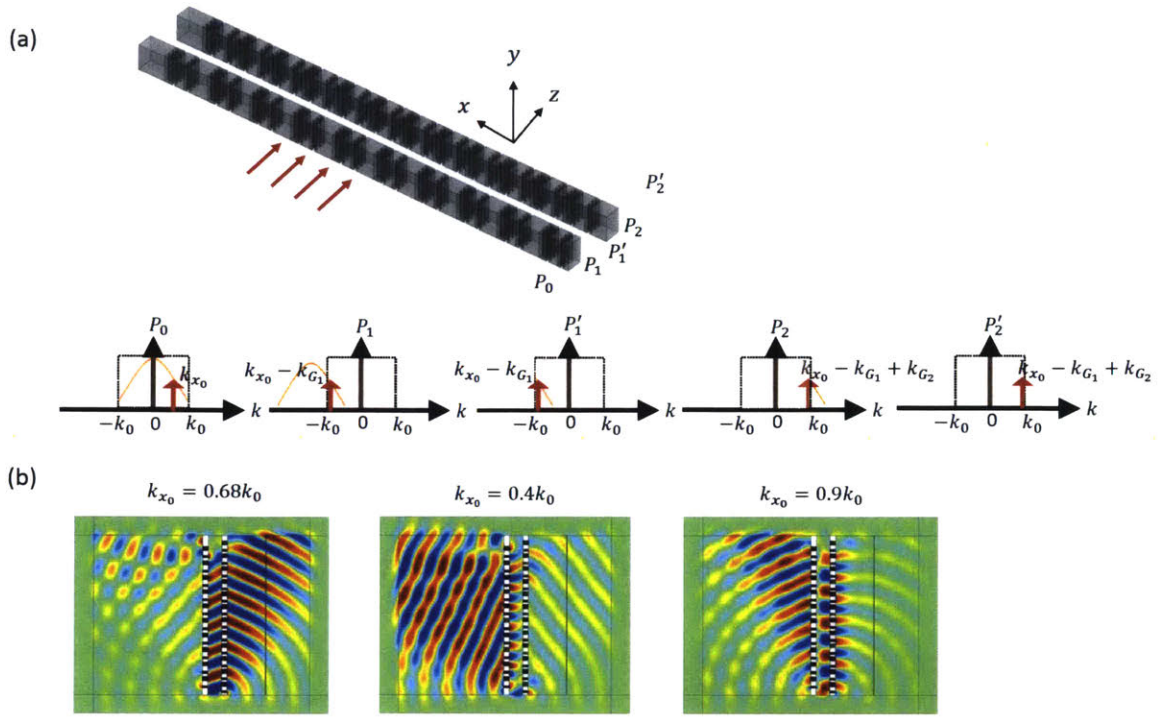

Figure 6-1: Direction-selected sound transmission with two layers of gratings. (a) System model and illustration of wave number conversion process for achieving direction-selection. P_0 is the incident pressure. P_1 is the pressure right after the first grating. P_1' is the pressure before the second grating. P_2 is the pressure right after the second grating. P_2' is the pressure at 20mm away from the second grating. (b) COMSOL simulated scattered pressure field for grating that selectively transmits the incident wave number range $[0.55k0, 0.75k_0]$ ($k_{G_1} = 1.6k_0$). The incident wave numbers are $k_{x_0} = 0.68k_0, 0.4k_0$, and $0.9k_0$, respectively.

or to the far-field. As shown in Fig. 6-1a, the first layer of phase grating will convert the input wave P_0 with wave vector k_{x_0} to P_1 with $k_{x_1} = k_{x_0} - k_{G_1}$, where $k_{G_1} = 2\pi/d_1$. The wave P_1' with $|k_{x_1}| < k_0$ can propagate to the second grating that is distance D away from the first grating, while the wave with $|k_{x_1}| > k_0$ will decay. The distance D is flexible as long as it is large enough to let the evanescent wave decay. In our simulation and experiment, D is set as 38.5mm, which is half wavelength. The second grating has grating period $d_2 = \lambda_0/1.9$, corresponding to $k_{G_2} = 1.9k_0$, and will convert P_1' to P_2 through -1st diffraction. Only those waves P_2' with $k_{x_1} \in (0.9k_0, k_0)$ ($k_{x_1} \in (-k_0, -0.9k_0)$) will be converted to $k_{x_2} \in (-k_0, -0.9k_0)$ ($k_{x_2} \in (0.9k_0, k_0)$) that are propagative in the receiving side of the system. Considering the combination of

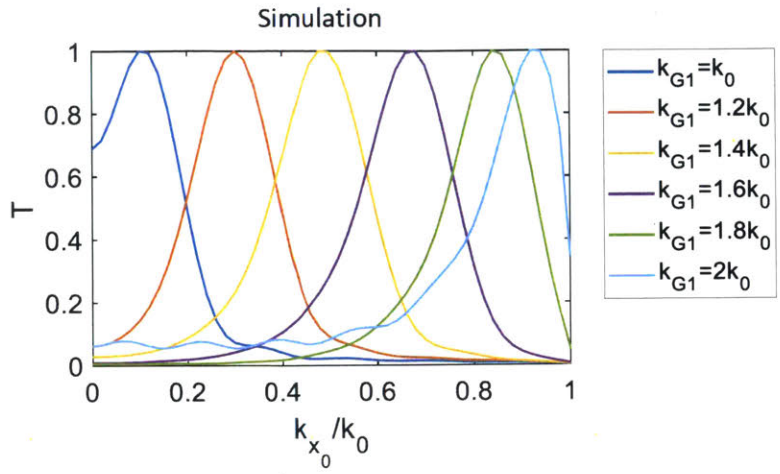

Figure 6-2: Simulation of normalized transmission coefficients for gratings configured for transmitting sound from different directions by changing $k_{G_1} = 2\pi/d_1$.

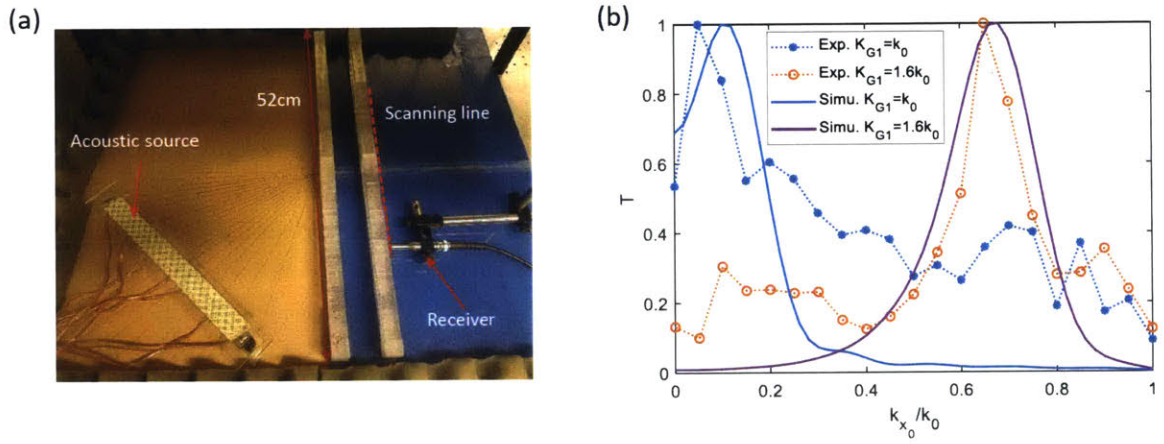

Figure 6-3: Experimental setup and results for direction selection with double grating. (a) Experimental setup. (b) Experimental results (dashed lines) of normalized transmission coefficients for two configurations of k_{G_1}, $k_{G_1} = 1.6k_0$ and $k_{G_1} = k_0$ compared with simulation results (solid lines).

the two layers, only the incident waves with $|k_{x_0}| \in (k_{G_1} - k_0, k_{G_1} - 0.9k_0)$ will transmit through the system, where $k_{G_1} > k_0$. By adjusting k_{G_1} in the range of $[k_0, 2k_0]$, the transmission direction can be tuned to cover $[0, 90°]$.

We performed simulation for sound transmission through two layer of phase grating in COMSOL. The incident waves are plane waves with different incident horizontal wave numbers $k_{x_0}/k_0 \in [0, k_0]$. The two gratings have finite length (520 mm) in the horizontal direction (x-direction), as in the simulation of the single layer. The dis-

tance between two gratings is $D = \lambda_0/2$. When $d_1 = \lambda_0/1.6$, the simulated sound pressure distribution at $k_{x_0}/k_0 = 0.68$, $k_{x_0}/k_0 = 0.4$ and $k_{x_0}/k_0 = 0.9$ are plotted in Fig. 6-1b. When $k_{x_0}/k_0 = 0.68$, almost all the incident energy is transmitted through the double-grating structure. When $k_{x_0}/k_0 = 0.4$, the wave becomes evanescent wave after passing the first grating. Thus little energy is transmitted through. When $k_{x_0}/k_0 = 0.9$, the wave becomes evanescent wave after passing through the second grating. Again, little energy is transmitted through.

The transmission coefficient for each incident k_{x_0} is taken as the average value of $|P(x)|^2$ along a line at 20cm away from the second grating at the transmission side of the system. The peak value of each transmission coefficient curve is normalized to one. In Fig. 6-2, we plot the normalized sound transmission coefficient calculated from simulation for different grating periods d_1 of the first grating. We can see that the double-grating structure only select a narrow range of k_{x_0} that can transmitt through. The full width at half maximum (FWHM) of each transmission peak is around $0.2k_0$. The selected k_{x_0} is tuned to different locations by changing k_{G_1}.

In order to further verify the direction selection behavior of the designed double-grating structure, we fabricated two sets of double grating structures that select two different directions at frequency $f = 4500$ Hz. The second grating layers in both sets of the double-grating structures are the same, with grating constant $k_{G_2} = 1.9k_0$. The first grating layer in one set has grating constant $k_{G_1} = 1.6k_0$, and that in the other set has grating constant $k_{G_1} = k_0$. Each double grating set is put in a 2D waveguide as shown in Fig. 6-3a. An acoustic line source is composed of seven transducers, each having diameter of 2 cm. The incident plane waves in different directions are generated by tilting the line source to different angles. The receiver scans a line of 20 cm close to the exit of the second grating layer in the double grating set. The receiver will capture both propagating wave and evanescent wave that transmit through the double-grating structure. The measured transmission coefficient is calculated as the total energy in the propagating band ($k_{x_0} < k_0$) by spatial Fourier transform.

The measured acoustic transmission coefficients as function of the incident direction (k_{x_0}/k_0) for the two double grating sets are plotted in Fig. 6-3b as the dashed

curves. The direction k_{x_0}/k_0 takes discrete values from 0 to 1 with a step of 0.05. The solid lines are the corresponding simulation results with direction step of 0.02. Each curve is normalized by its maximum value. For each configuration, experimental result shows that the double grating set selects the wave in the designed direction range with FWHM of around $0.1k_0$, which is smaller than that of the simulation result (FWHM of around $0.2k_0$). However we notice that the ratio of highest transmission to lowest transmission (signal to noise ratio) in experiment is lower than that in simulation. This is mainly due to the influence of the thermal viscous loss and noise from the reflection of multiple boundaries.

6.3 Decoupling of frequency dependence and direction dependence

We mentioned in introduction that most of the existing direction selecting structures have highly frequency-dependent behaviors. Here we propose a way to decouple the frequency dependence and direction dependence.

In the previous section, we achieved direction-selected sound transmission for a single frequency ($f_0 = 4500$ Hz). Since we maximize the energy transmission by exciting Fabry-Perot resonance inside the channels, and Fabry-perot resonance is highly frequency dependent, we expect that the double-grating structure we designed demonstrates large transmission only at the designed frequency and its harmonics. In order to verify this hypothesis, we use COMSOL simulation to obtain the acoustic transmission coefficient of the double grating structure as a function of both direction and frequency, and put the results in a 2D plot of the frequency-direction space. Fig. 6-4d shows the results for the double grating designed for $f_0 = 4500$ Hz. We find that the acoustic transmission not only localized in direction, it also localized in frequency. It filters both the designed direction and frequency at the same time, which is not common in existing acoustic filters in literature. By changing h_1 and h_2, we can tune the working frequency to other regions without influencing the direction selection.

For example, in Fig. 6-4a-c, we plot the acoustic transmission in frequency-direction space for three different combinations of h_1 and h_2, each selectively transmitting a different frequency range from 4500 Hz to 5500 Hz at the direction $k_{x_0}/k_0 = 0.6$. Similarly, by changing the grating period, we can tune the selected direction without influencing the frequency filtering. In this way, we decouples the direction dependence and frequency dependence of acoustic transmission.

Taking one step further, if we stack three different double grating layers together, as shown in Fig. 6-5a-b, we can get the broadband direction selection as shown in Fig. 6-5c. At each frequency, only one double grating layer is transmitting most of the energy through since the frequency is closest to its resonance frequency. The FWHM of the direction selection (k_{x_0}/k_0) is around 0.2. Current simulation gives us a bandwidth of from 4500 Hz to 5500 Hz. By stacking more layers of double-grating structure, we can expand the frequency range. The largest frequency bandwidth we can obtain using this method is from f_{min} to $2f_{min}$, where f_{min} is the smallest frequency in the working frequency band. Because the second harmonic of f_{min} will interfere with higher frequencies. There is another limiting factor for the number of layers we can stack. The more layers we stack, the less the energy will be transmitted by each layer. The energy efficiency of the designed system will drop with increased bandwidth.

6.4 Summary

In summary, we proposed a new way to realize acoustic direction selective transmission based on the previously developed acoustic binary phase gratings. The combination of two binary phase gratings with different periods can block most of the incoming wave except for the wave in one particular direction range, by utilizing the fact that evanescent wave decays as it leaves one of the gratings. The selected direction can be tuned by changing the period of the first grating in the double grating combination. We showed that the proposed structure can select both a narrow direction range and a narrow frequency band at the same time, thus decouple the frequency dependence and

direction dependence of the acoustic transmission through it. We further demonstrate the broadband direction selection using simulation by stacking multiple layers of the double-grating structures, each layer designed to work for a single frequency. The stacked structure can select one narrow range of incident wave direction over frequencies in one octave.

Currently, the binary phase gratings are formed by narrow waveguide channels, which has relatively large thermal viscous loss. The energy that can pass through the double grating structure at the selected direction is only around 10% of the incident energy. In the future, this percentage of energy transmission, or efficiency of the system, can be improved by designing new way to realize the two phase shift values in the binary phase grating.

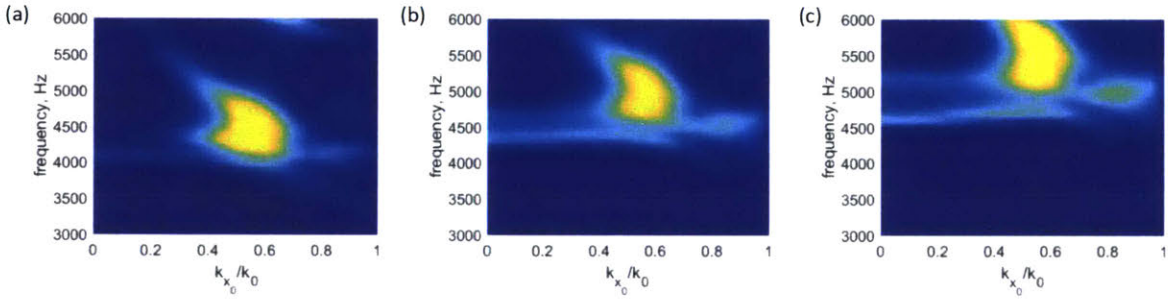

Figure 6-4: Simulated acoustic transmission as a function of incident direction and frequency for double grating structures with different h_1 and h_2. (a) $h_1 = 5.6$ mm, $h_2 = 12$ mm. (b) $h_1 = 5$ mm, $h_2 = 10.7$ mm. (c) $h_1 = 4.5$ mm, $h_2 = 9.7$ mm.

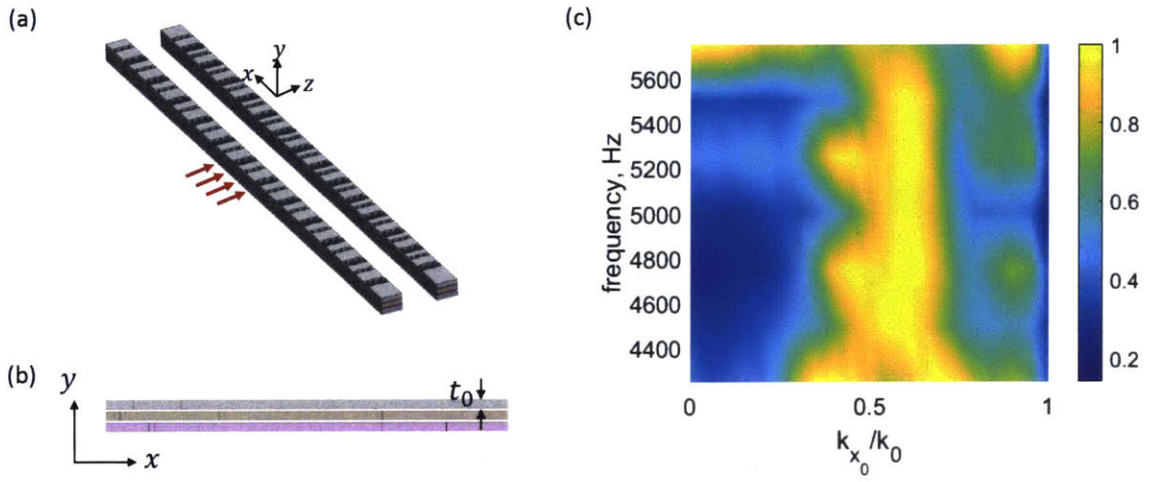

Figure 6-5: Broadband direction selection by stacking double grating layers. (a-b) the system model for stacking. Each layer works for a localized frequency region at a fixed incident direction. $t_0 = 10$ mm. Different layers stack in y direction. The wave incidents in z direction. (c) Simulated broadband acoustic transmission as a function of direction (k_{x_0}/k_0) and frequency from 4500 Hz to 5500 Hz.

Chapter 7

Summary and outlook

7.1 Summary

My PhD work is dedicated to exploring acoustic metamaterials and their applications in acoustic sensing.

Two types of phase shifters are designed, one with constant time delay and the other with constant phase shift as the frequency changes. Acoustic metamaterials are designed based on the two types of acoustic phase shifters. Acoustic binary phase grating, which is composed with only two discrete phase shift values generated by curved waveguide channels (constant time delay), is designed to realize highly efficient wave steering with much less complex structure compared to previous metasurfaces for similar functions. The combination of two acoustic binary phase gratings with different period demonstrates direction selection for a single frequency. The same double-grating combination structure selects the frequency at the same time. This is to our knowledge the first structure that selects direction and frequency at the same time. By stacking multiple double-grating combinations, broadband direction selection is demonstrated in simulation. This is to our knowledge the first method to realize broadband direction selection in acoustics. Acoustic flat lenses for wave focusing and steering, as well as broadband acoustic transmission and reflection control, are designed based on phase shifters with constant differential phase shift over a broad frequency range. Most of the metasurfaces designed previously are based

on the phase shifters that has constant time delay. Our acoustic flat lenses are the first demonstration of acoustic metasurfaces based on unit cells that have constant differential phase delay over a broad frequency range. The direct consequence of this type of phase shifters is that the steering angles or the focusing locations of waves having different frequencies are different. The proposed acoustic phase shifters, flat lenses, and binary phase gratings are new devices for acoustic wave control that will benefit future applications in acoustic sensing problems.

An acoustic subwavelength imaging and edge detection system is designed and experimentally demonstrated. The whole system is composed of a transmitter in the near field of the object and a receiver in the far-field. The transmitter and the receiver are identical, each composed with the acoustic binary phase gratings and additional filter layers formed by acoustic Helmholtz resonator arrays. The system can select and project a narrow band of subwavelength spatial frequency information from the near field to the far-field. Subwavelength imaging and edge detection for 1D slit objects is demonstrated experimentally with 3D printed prototypes. In our system, the travel distance of evanescent wave is greatly expanded compared to previously existing subwavelength imaging systems. Resolution in far-field imaging is largely improved. What's more, an alternative method to realize the filter layer using homogeneous material slab with subwavelength thickness and slow sound speed is proposed and explored in theoretical modeling and numerical simulation. The filter layers in the subwavelength imaging and edge detection systems and the proposed alternative here are the first explorations for near-field spatial filtering in acoustics. Our effort in subwavelength imaging systems will benefit the fields of biomedical imaging, non-destructive test, and acoustic communication in the future.

Soft tunable acoustic metamaterials based on hydrogel are proposed and demonstrated by creating 1D channels in hydrogel. When the channels are filled with water, the acoustic energy is nearly perfectly transmitted. When the channels are filled with air, the acoustic energy is nearly perfectly reflected. Other transmission values can be obtained by changing the filling materials (water/air/liquid metal) or filling ratios.The propose hydrogel based acoustic metamaterial is a new approach and material sys-

tem to achieve tunable acoustic properties over air-water-solid ranges and broadband frequencies, which is inaccessible in existing acoustic materials.

7.2 Outlook

The work in the dissertation leads to several potential future research directions.

For the subwavelength imaging and edge detection system, currently the lenses is 1D line type structure. In order to obtain 2D image, the 1D lenses need to move and scan in another dimension. In the future, 2D lenses can be designed to capture 2D image without moving the lenses. Currently, multiple lenses are needed in order to capture different subwavelength spatial frequency bands. In the future, the fixed lenses can be made tunable so that a single lense can capture all the bands at demand. Such tunable lenses can be applied to imaging applications that requires dynamic configuration of the imaging resolution.

For the isotropic thin slab with slow sound speed for near field spatial filtering and enhancement, the key is to find materials that have slow sound speed. Porous materials are good candidates for slow sound speed material. However, they usually have large sound absorption rate due to thermal viscous loss when wave travels inside it. Finding materials that have slow sound speed and low viscous damping at the same time is an important direction for future research.

For the acoustic binary phase grating for sound steering and the double phase grating for direction selection, the major issue of current design is high thermal viscous loss due to the narrow waveguide channels, especially when wave needs to pass through two gratings. New realization for the phase grating is needed to increase the energy efficiency.

For the hydrogel based acoustic metamaterials, currently we realized a thin sheet with tunable acoustic impedance. The next step would be stacking multiple thin layers to create tunable phase gradient for broadband impedance matching. 2D patterns can also be create for applications requires dynamic masks or structured acoustic illumination, as shown in some preliminary work in Appendix D. Other mechanisms

for tuning the material properties may be explored, such as the swelling, chemical tuning, mechanical tuning, etc.

In general, the frequency ranges of currently designed metamaterials are in the KHz range for airborne experiment and in 100KHz range for underwater experiments. Those ranges are chosen for the convenience of fabrication and test in the lab. For future applications in biomedical ultrasonic imaging or underwater acoustics, the sizes of the system needs to be scaled so that the designed systems work for the corresponding new frequency range. For example for the biomedical ultrasonic imaging field, the working frequencies are usually at MHz range. Thus the features in current systems need to be scaled to micrometer sizes. This puts high demand for advanced manufacturing techniques such as 3D printing or metal casting. More study on the influence of factors such as thermal viscous loss, geometry defects, nonlinearity, noise, and so on during this scaling process is also needed.

Appendix A

Acoustic subwavelength edge detection in sand

Chapter 4 introduced the theoretical modeling, simulation and experimental demonstration of an acoustic subwavelength imaging and edge detection system. In the experiments in Chapter 4, the fabricated lenses are placed in air and performed edge detection for objects in air. In this chapter, I place the same set of lenses in a sandbox and demonstrate edge detection in sand. This example demonstrate the potential to apply the edge detection technique to oil detections in sand.

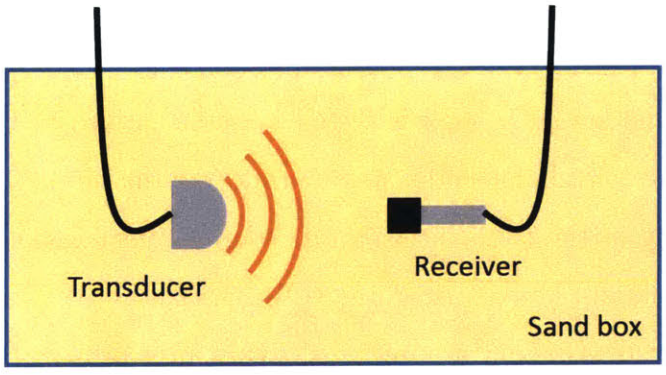

Figure A-1: System schematic for sound speed measurement in sand.

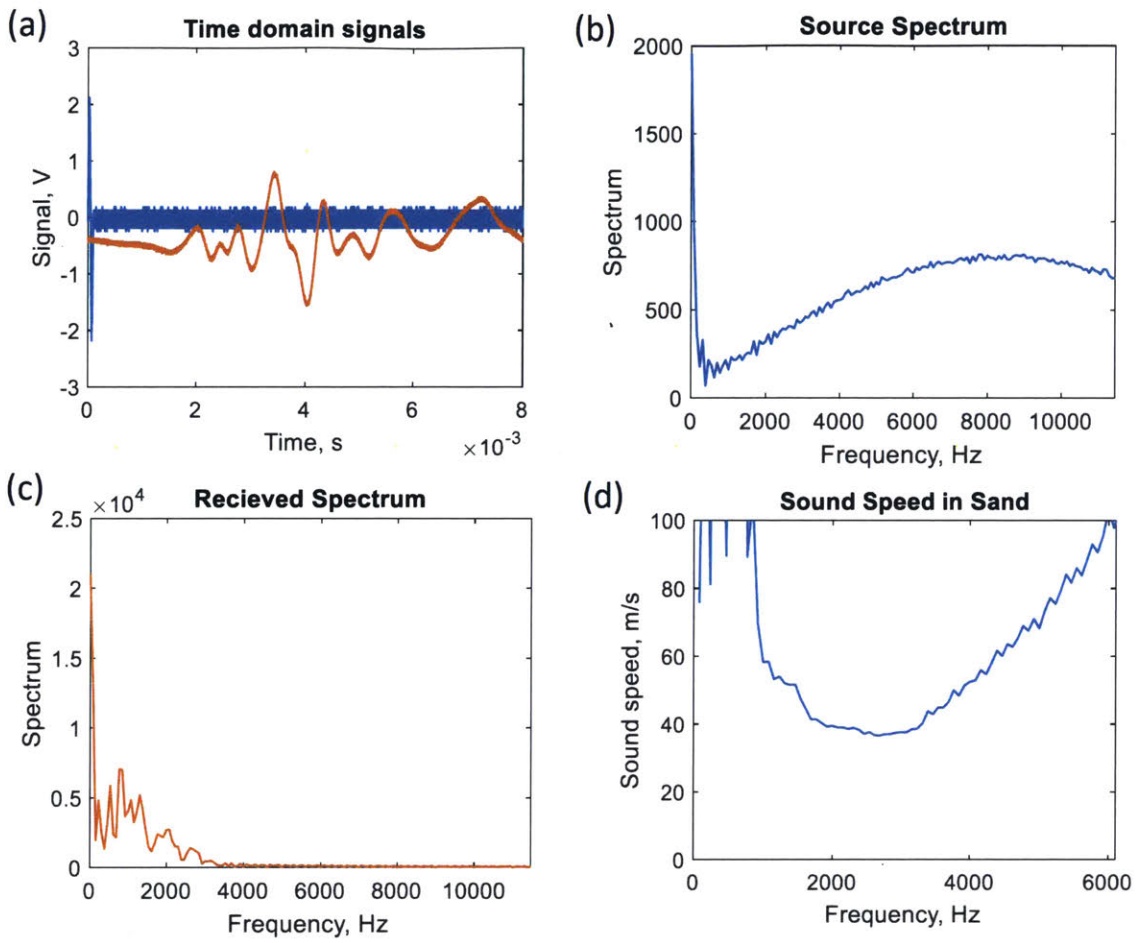

Figure A-2: Sound speed measurement results for 10 cm propagation distance in sand. (a) The source signal and the received signal after propagating 10 cm in sand. (b-c) Frequency spectrums of the source signal (b) and the received signal (c). (d) Measured sound speed in sand as a function of frequency.

A.1 Sound speed in sand

First of all, the sound speed in sand is tested with the setup shown in Fig. A-1. A pulse signal with one period of 9000 Hz wave is sent into the sand. A receiver is put at different distances from the transducer to test sound transmission through different distances. The results in Fig. A-2 are obtained when the distance is 10 cm. Fig. A-2a plots the sound source signal and the received signal after propagating in sand for 10 cm. Fig. A-2b and Fig. A-2c plots the frequency spectrum of the source signal and the received signal. We find that almost all the energy above 3500 Hz is attenuated during the propagation in sand. Measurements in other distances show that sound

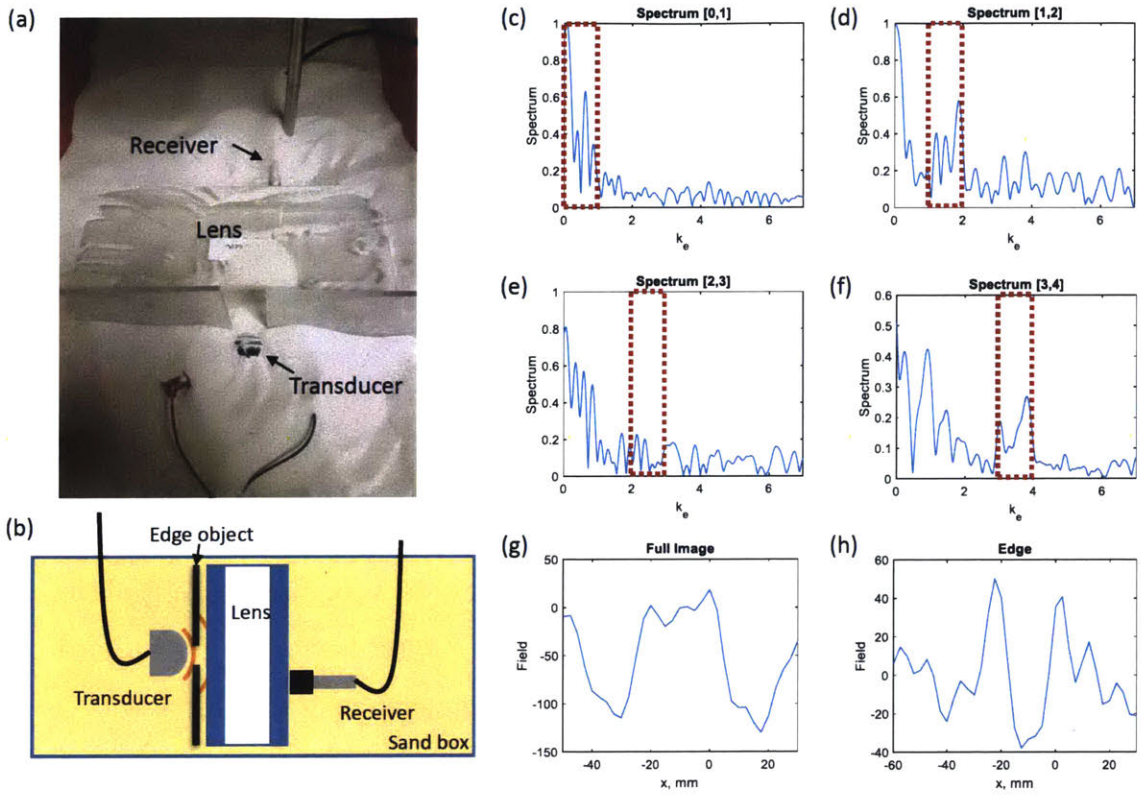

Figure A-3: Experimental setup for edge detection in sand and the edge detection result for a 25 mm slit. (a) Photo of the experimental system in sand box. (b) System schematic for edge detection. (c-f) The received signal from the empty waveguide and lens1, lens2, lens3. (g) Full image of the 25 mm slit. (h) Edges of teh 25 mm slit.

wave with frequency larger than 3500 Hz cannot travel more than 2cm in sand, using current 4 ohm mini transducer with 20v-pp driving voltage. Sound speed in sand is measured by comparing the phase delays at each frequency in the received signal after propagating different distances in sand. The obtained sound speed is shown in Fig. A-2d. Measured sound speed for wave in frequency range from 1500Hz to 3500Hz is between 40m/s to 50m/s. This is much smaller than the sound speed in air (340 m/s).

A.2 Edge detection in sand

Then we performed edge detection in sand. The lenses, transducer, and receiver are sealed by plastic membranes and buried in sand (Fig. A-3a-b). The previously

fabricated far-field lenses work at 9000Hz. At 9000Hz, wave cannot propagate in sand for more than 2 cm. So in the current setup in sand box, the transducer is put close to the slit, and the slit is put in contact with the lenses, in order to minimize the sound propagating distance in sand and further prevent strong attenuation. The decaying nature of sound wave in sand makes the sand very good absorbing boundary layers. Now continuous wave at frequency of 9000 Hz is used as the source signal, which is different from the experiment in air that uses time-windowed sound (several periods of 9000 Hz sound) as the source signal.

The edge detection result for a 25 mm acrylic plastic slit buried in sand is shown in Fig. A-3c-h. The empty waveguide and the three lenses transmit the corresponding spatial frequency bands from one side to the other side. The full image is obtained by adding all four spatial frequency bands, and the edges of the slit is obtained by adding the three high spatial frequency bands. The membranes that are used to seal the lenses and transducers as well as the small amount of sand between transducers and lenses greatly reduce the signal to noise ratio and distort the phase response. In the future, if we modify the lenses so that they can work at frequency below 3500 Hz, or use transducer with higher power, we can achieve better signal to noise ratio in subwavelength imaging and edge detection in sand.

Appendix B

Sound speed measurement for different soft materials

In this part I will introduce the experimental method to measure the sound speed of different soft materials in water. We measure the speed of sound in the PAAm-alginate hydrogel [113] and elastomers over three different frequencies (i.e., 40 kHz, 200 kHz and 1 MHz), representing the frequencies used in various applications. For instance, the low-frequency ultrasound (from 10 KHz to 50 kHz) is frequently used for long-range sonar or oceanic animal communications while the mid-frequency ultrasound (from 100 KHz to 300 kHz) is usually used for high-resolution sonar or by some animals (e.g., dolphins) [151]. For medical diagnostic ultrasound, higher frequencies (1 5 MHz) are usually adopted [113, 152].

In order to measure the speed of sound of the hydrogels and elastomers, the transmission ultrasound signals at three different frequencies (i.e., 40 kHz, 200 kHz and 1 MHz) were used. All measurements were conducted in the water tank using the samples with size of 120 mm in width, 120 mm in length and 50 mm in thickness (Fig. B-1). A pulse of central frequency (i.e., 40 kHz, 200 kHz and 1 MHz) was generated by a signal generator (Tektronix) and sent to the transducer (CTG Model ITC-1042 for 40 kHz, Olympus NDT ultrasonic transducers for 200 kHz and 1 MHz). The signal passed through the sample and the transmitted signal was collected by the hydrophone (CTG Model ITC-1089D for 40 kHz, Olympus NDT ultrasonic transduc-

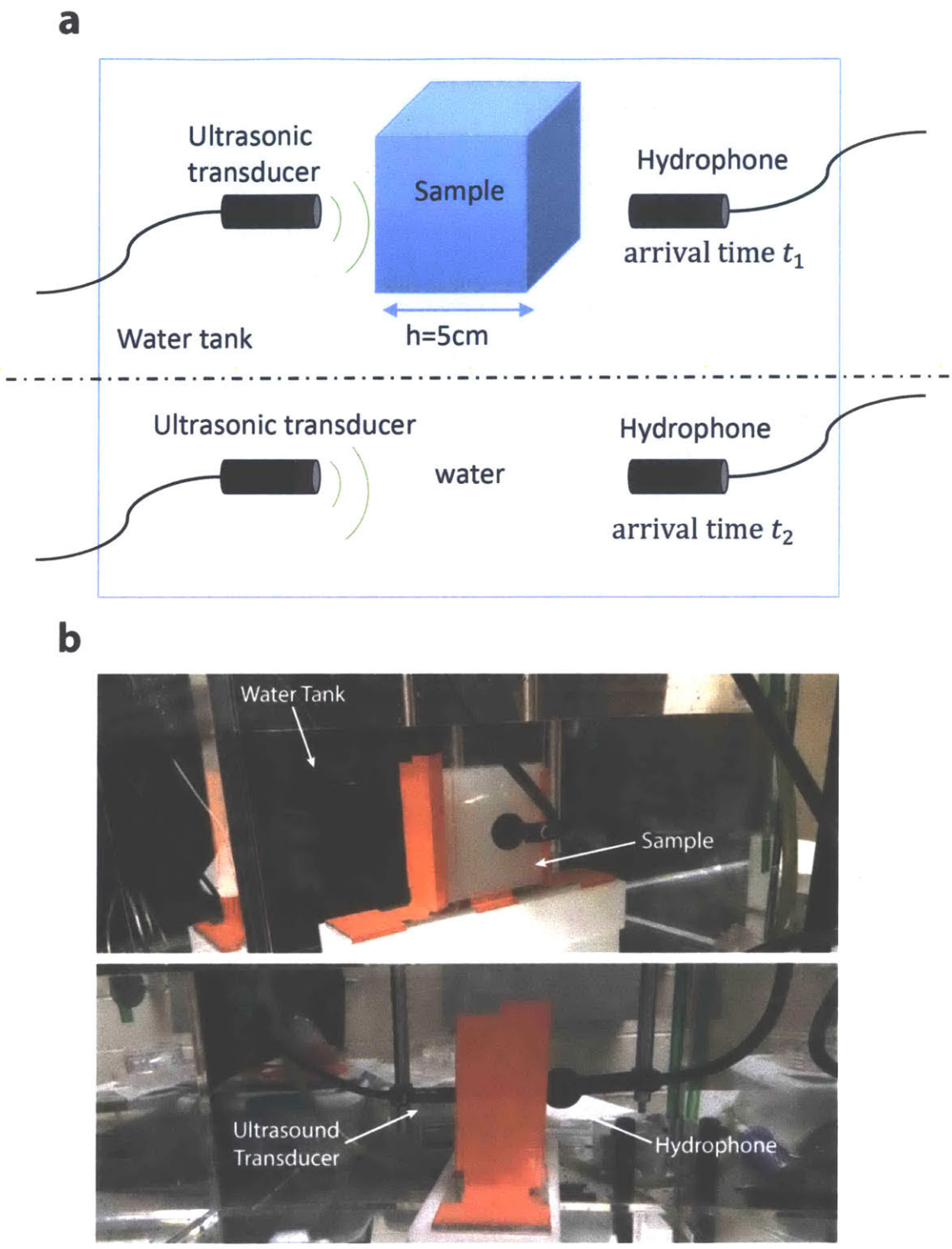

Figure B-1: Experimental setup for underwater sound speed measurement (a) Schematics (b) Photos of the experimental system in water tank.

ers for 200 kHz and 1 MHz). The measured signals were sent to the computer through the connected oscilloscope (Agilent) and the data were processed by MATLAB. The data were plotted in the travel time vs. the measured signal amplitude curves (Fig. B-2). The t = 0 corresponded to the time at which the ultrasound signal was sent from the transducer and the signal amplitudes were measured by the hydrophone upon the arrival of the transmitted ultrasound signals through the samples. The ultrasound signals sent at each frequency had the same amplitude while the attenuation varied among sample materials due to different acoustic impedance and viscous effect of each material. At each frequency, the speed of sound in pure water was measured as a control parameter. The arrival time difference, $\delta t = t_2 - t_1$ of the received pulse after passing through the sample and through pure water was obtained and the speed of sound in the sample was calculated as

$$t_2 - t_1 = \frac{h}{c_{\text{water}}} - \frac{h}{c_{\text{sample}}}, \tag{B.1}$$

where $h = 5$ cm represents the thickness of the sample, c_{water} represents the speed of sound in pure water and c_{sample} represents the speed of sound in the sample. The acoustic impedance, z_{sample} of the hydrogels and elastomers were calculated from the definition of the acoustic impedance as

$$z_{\text{sample}} = \rho_{\text{sample}} c_{\text{sample}} \tag{B.2}$$

where ρ_{sample} represents the known density of materials, and c_{sample} represents the measured speed of sound of materials. The acoustical reflection coefficient, R, at the interface between water and the sample material can be calculated from the acoustic impedances of materials by

$$R = \frac{z_{\text{water}} - z_{\text{sample}}}{z_{\text{water}} + z_{\text{sample}}} \tag{B.3}$$

where z_{water} is the acoustic impedance of water, and z_{sample} is the acoustic impedance of the sample material.

Tthe measured speed of sound is identical over these selected frequencies without

dispersion for all sample materials. We have $c_{\text{hydrogel}} = 1485.7$ m/s, $c_{\text{ecoflex}} = 983.4$ m/s, $c_{\text{elastosil}} = 979.6$ m/s, $c_{\text{sylgard}} = 1022.4$ m/s. We found that the PAAm-alginate hydrogel shows acoustic impedance, $z_{\text{hydrogel}} = 1.487 \times 10^6$ Pa*s/m, which is only around 1% different from the acoustic impedance of pure water (i.e., $z_{\text{water}} = 1.448 \times 10^6$ Pa*s/m) as the speed of sound inside the hydrogel and pure water and their density are nearly identical. As a result, the acoustic reflection coefficient between water and the hydrogel is as low as $R = 0.013$. In contrast, elastomers have much lower characteristic acoustic impedances than water (i.e., $z_{\text{ecoflex}} = 1.052 \times 10^6$ Pa*s/m for Ecoflex, $z_{\text{elastosil}} = 1.058 \times 10^6$ Pa*s/m for Elastosil and $z_{\text{sylgard}} = 1.053 \times 10^6$ Pa*s/m for Sylgard 184) regardless of their optical properties leading to much higher acoustic reflection coefficients against water than hydrogels (i.e., $R = 0.158$ for Ecoflex, $R = 0.156$ for Elastosil and $R = 0.158$ for Sylgard 184).

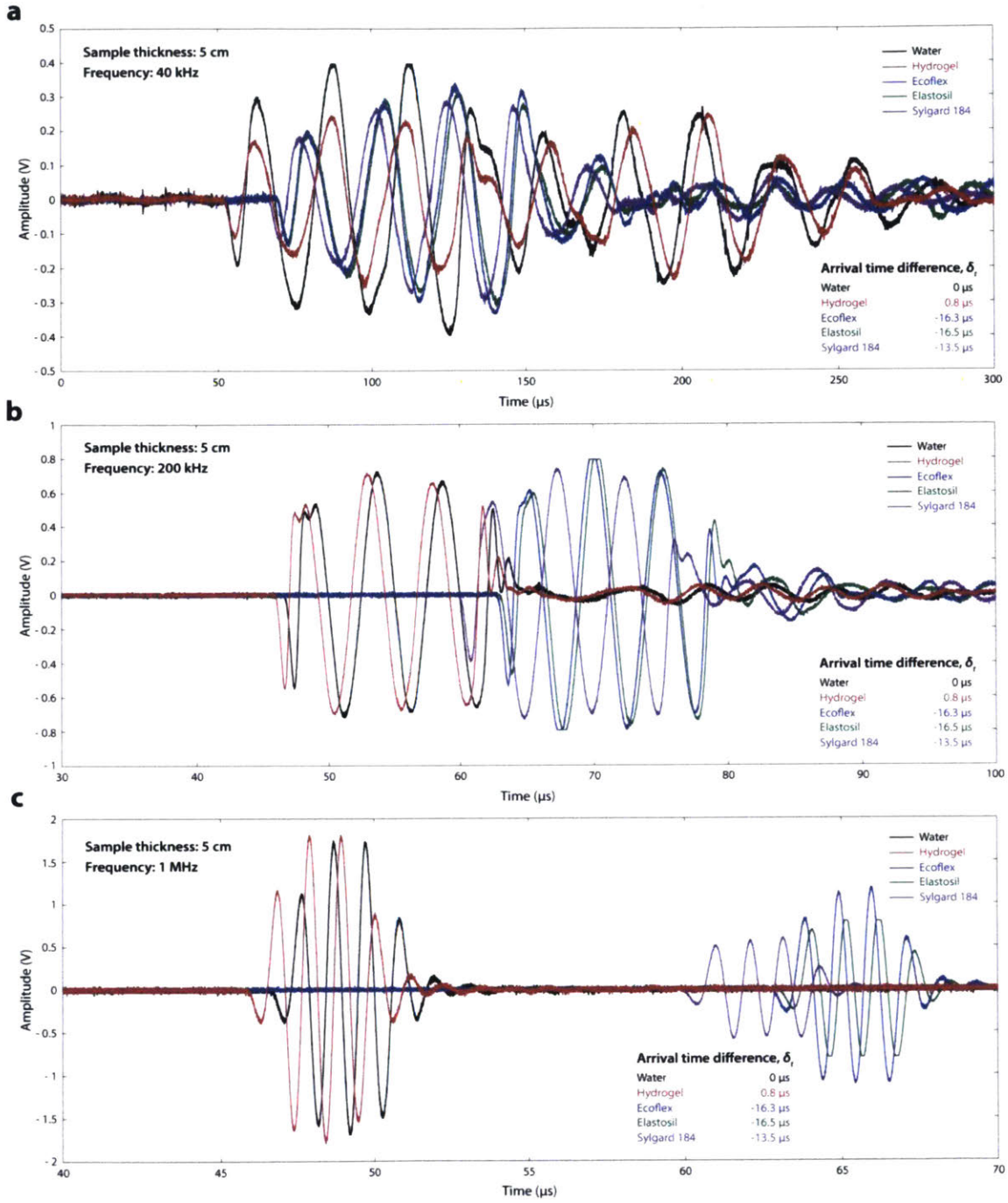

Figure B-2: Speed of sound measurements for pure water, PAAm-alginate hydrogel, Ecoflex, Elastosil and Sylgard 184 [113]. The curves indicate the ultrasound signals travel through the samples from the transducer to the hydrophone with the source frequency of 40 kHz (a), 200 kHz (b) and 1 MHz (c). The t = 0 corresponded to the time at which the ultrasound signal was sent from the transducer and the signal amplitudes were measured by the hydrophone upon the arrival of the transmitted ultrasound signals through the samples. The ultrasound signals sent at each frequency had the same amplitude while the attenuation varied among sample materials due to different acoustic impedance and viscous effect of each material.

Appendix C

Acoustic Willis materials design, fabrication, and testing

C.1 Introduction

Acoustic Willis material is a type of materials that couple pressure and momentum to both strain and velocity. The Willis coupling gives an extra degree of freedom to parameter space, which will benefit the applications such as impedance matching to reactive loads, non-reciprocal devices, and metasurfaces with tailored reflected phase response [70, 153, 154, 155]. Currently, large-scale fabrication of Willis material is difficult because of the asymmetric details. Experimental demonstrations of Willis coupling still lack. The goal of this work is to: 1) expanding the fabrication capability of Willis material, 2) conduct simulation and experimental study of Willis material to find better structure, better material choice, and more applications.

C.2 Governing equation derived from the mass-spring model

The Governing equation for Willis coupling can be derived from an effective mass-spring model, as shown in Fig. C-1. Here, m_1 and m_2 are the masses of two particles

connected with a spring with spring constant k. Forces F_L and F_R are implemented on m_1 and m_2 respectively. δ_1 and δ_2 are damping coefficients associated with m_1 and m_2.

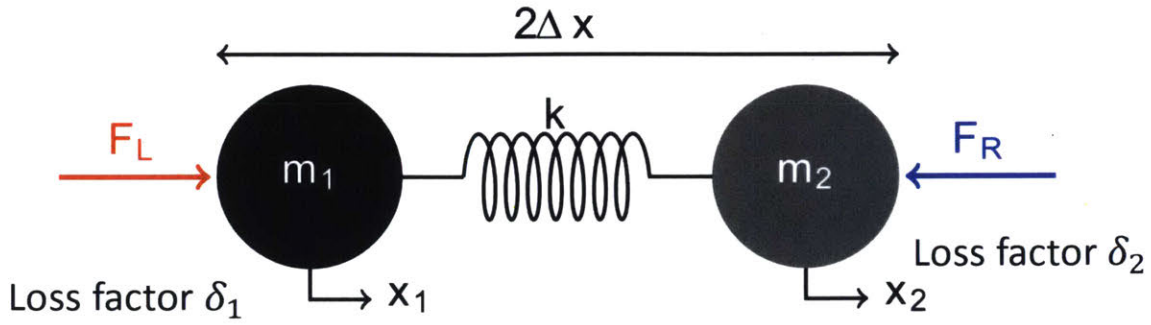

Figure C-1: Mass-spring model for acoustic Willis materials.

The equations of motion for m_1 and m_2 can be expressed as:

$$m_1\ddot{x}_1 + \delta_1\dot{x}_1 = F_L - k(x_1 - x_2), \tag{C.1}$$

$$m_2\ddot{x}_2 + \delta_2\dot{x}_2 = -F_R + k(x_1 - x_2), \tag{C.2}$$

where x_1 and x_2 are the displacements of m_1 and m_2.

We define another four parameters. Volume strain is defined as $\varepsilon = \frac{x_1 - x_2}{2\Delta x}$. Net displacement is defined as $\xi = \frac{x_1 + x_2}{2}$. Net force is defined as $\mu = \frac{F_L - F_R}{2\Delta x}$. Pressure is defined as $\frac{F_L + F_R}{2}$. Then the equations of motion become:

$$-p \approx \frac{m_2 - m_1}{2}\ddot{\xi} + \frac{\delta_2 - \delta_1}{2}\dot{\xi} + k\Delta x\varepsilon = (\phi\ddot{\xi} + \phi'\dot{\xi}) + \kappa\varepsilon = \psi\dot{\xi} + \kappa\varepsilon \tag{C.3}$$

$$\begin{aligned} F_L - F_R &= (m_1 + m_2)\ddot{\xi} + (\delta_2 + \delta_1)\dot{\xi} + (m_2 - m_1)\Delta x\ddot{\varepsilon} + (\delta_2 - \delta_1)\Delta x\dot{\varepsilon} \\ &= 2\Delta x(\gamma\ddot{\xi} + \gamma'\dot{\xi} + \phi\ddot{\xi} + \phi\ddot{\varepsilon} + \phi'\dot{\varepsilon})) \\ &= 2\Delta x(\rho\dot{\xi} + \psi\dot{\varepsilon}) \end{aligned} \tag{C.4}$$

In Eq. C.3 and Eq. C.4, $\psi = \phi' + j\omega\phi$ and $\rho = \gamma' + j\omega\gamma$, where $\phi' = \frac{\delta_2 - \delta_1}{2}$, $\phi = \frac{m_2 - m_1}{2}$, $\gamma' = \frac{\delta_2 + \delta_1}{2\Delta x}$, $\gamma = \frac{m_2 + m_1}{2\Delta x}$.

As a result, we have the governing equations as:

$$-p = \psi\dot{\xi} + \kappa\varepsilon \tag{C.5}$$

$$\mu = \rho\dot{\xi} + \psi\dot{\varepsilon} \tag{C.6}$$

ψ is called Willis coupling coefficient. It contains both real part and imaginary part. The real part is determined by the non-homogeneous distribution of loss in system, and the imaginary part is determined by the non-homogeneous distribution of mass. When $m_1 = m_2$ and $\delta_1 = \delta_2$, $\psi = 0$. The governing equations become the ordinary governing equation for homogeneous materials:

$$-p = \kappa\varepsilon \tag{C.7}$$

$$\mu = \rho\dot{\xi} \tag{C.8}$$

From governing equations Eq. C.5 and Eq. C.6, we can derive the effective impedance as $Z\pm = Z_0(\pm 1 + iW)$, where $Z_0 = \sqrt{\rho\kappa}$, and $W = \frac{\omega\psi}{Z_0}$. There is no '$\pm$' before the Willis coupling term jW in the expression for effective impedance, which means that Willis coupling will induce different behavior for wave incident from different directions.

C.3 Fabrication of acoustic Willis materials

The Willis coupling originates from asymmetric distribution of density/modulus/damping. We developed three different ways to fabricate asymmetric structures that could demonstrate Willis coupling. The first way is Willis material composed with asymmetric air inclusions in PDMS matrix, as shown in Fig. C-2. The structure is fabricated by curing PDMS on 3D printed template layer by layer and stack multiple layers together to form a cube. The air inclusion has an asymmetric donut shape. The outer diameter of the donut shape is 2mm and the inner diameter is 1mm with an offset of 0.5mm. The background PDMS and the air inclusion can be replaced with other

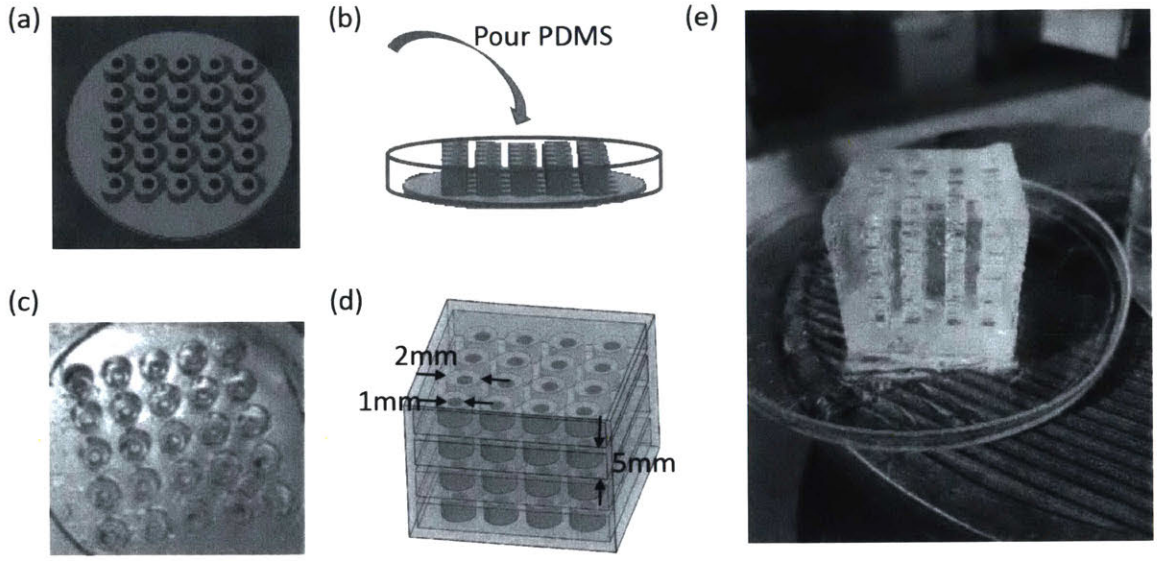

Figure C-2: Fabrication of Willis material based on PDMS with asymmetric air inclusions. (a) 3D printed template. (b) Put the 3D printed template in a container, pour liquid PDMS into the container and cure to form one layer of Willis material. (c) A picture of one layer of Willis material. (d) Willis material block formed by stacking multiple layers. (e) A picture of the fabricated Willis material block.

materials such as water, elastomer or hydrogel. The second way is Willis material composed with hydrogel and asymmetric cylinder arrays, as shown in Fig. C-3. The asymmetric cylinder arrays provide the asymmetric distribution of density and compliance for generating Willis coupling. The hydrogel matrix has exact same impedance with water so does not generate extra scattering of the sound wave in water. This type of structure has the potential to be used as underwater Willis material. The third way is Willis material with rigid cavity and asymmetrically located scatter, as shown in Fig. C-4a. This type of structure is fabricated by 3D printing techniques using acrylic resin. The center cylinder is moved away from the center of the cavity in order to create asymmetric distribution of density, compliance, and damping.

C.4 Simulation and experimental measurement

We performed simulation and experimental measurements to get the effective Wills coupling parameters for the 3D printed Willis structure shown in Fig. C-4a. Simula-

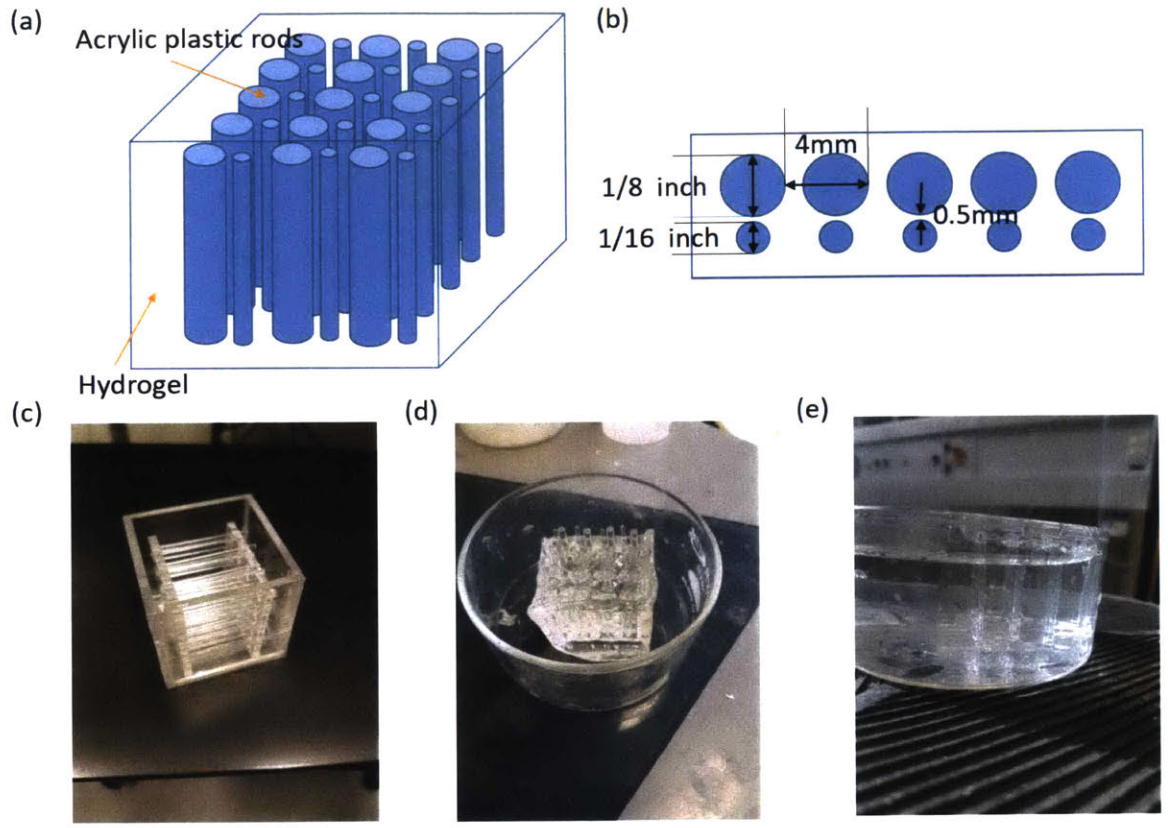

Figure C-3: Fabrication of Willis material based on hydrogel and asymmetric acrylic plastic rod arrays. (a) Side view of the system model. (b) Top view of the system model. (c) Acrylic rod arrays composed of one array with larger diameter and one array with smaller diameter. (d-e) A picture of the fabricated Willis material in air (d) and in water (e).

tion is performed with COMSOL. The structure is put inside a waveguide as shown in Fig. C-4b. Narrow region acoustics feature is applied to the simulation model to capture the influence of damping. The wave incidents from left to the right. From Fig. C-4b we observe that the field amplitudes inside the cavity are different when the wave incidents from different sides of the cavity. The S parameters (S_{11}, S_{22}, S_{12} and S_{22}) are obtained in the COMSOl simulation. Then the Willis coupling factor is calculated as

$$W = \frac{S_{22} - S_{11}}{ir}, \tag{C.9}$$

where $r = \sqrt{(1 - S_{11}S_{22} + S_{12}^2)^2 - 2S_{12}^2}$. In experiments, the 3D printed structure is put inside the acoustic impedance tube (Scantek BSWA SW series Impedance Tubes,

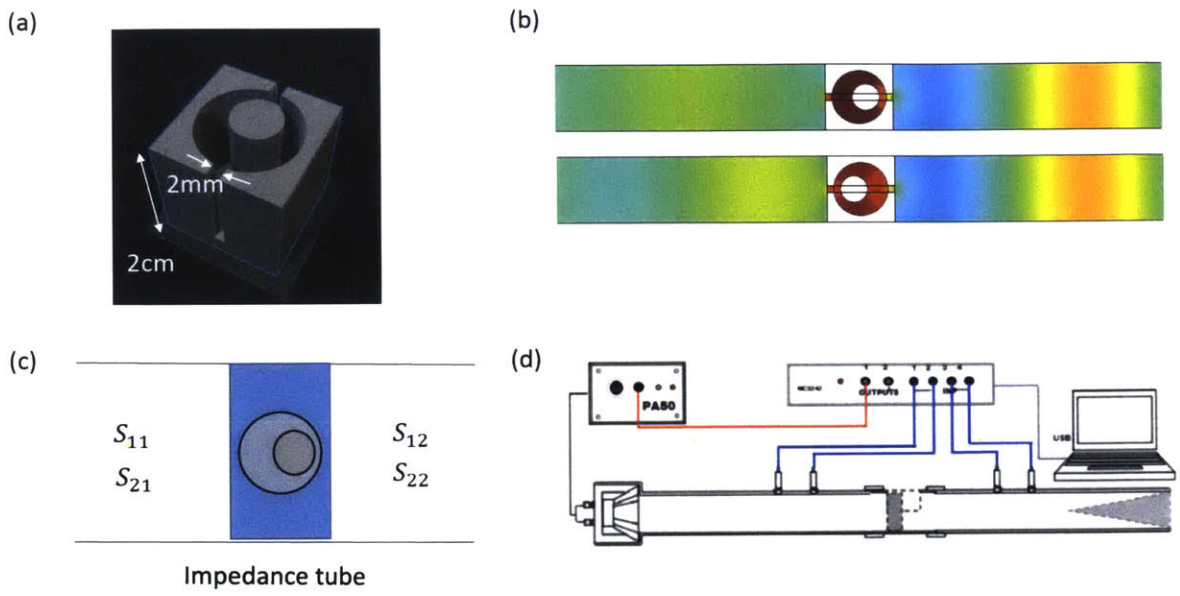

Figure C-4: 3D printed Willis material with rigid cavity and asymmetrically located scatter. (a) Geometric model (b) Comsol simulation of wave propagation through the Willis material unit cell from two different directions. (c) Impedance tube measurement model (d) Acoustic impedance tube.

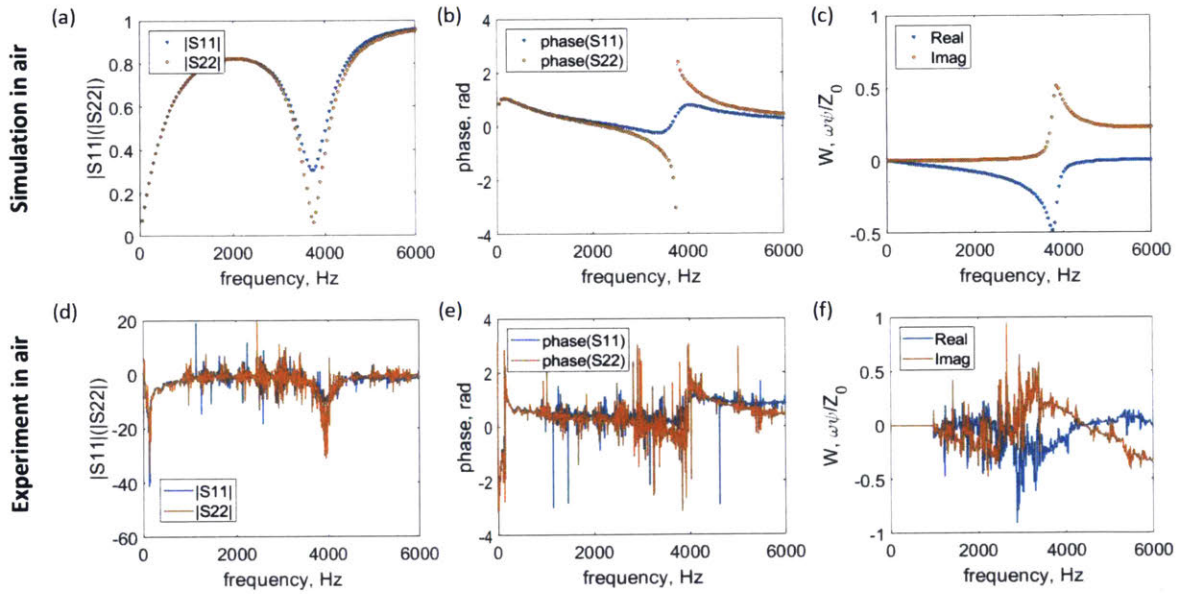

Figure C-5: Simulation and experimental results when the 3D printed Willis structure is put in air. (a-b) Amplitude (a) and phase (b) of the simulated S_{11} and S_{22} parameters. (c) Real and imaginary part of the simulated Willis factor. (d-e) Amplitude (d) and phase (e) of the experimental S_{11} and S_{22} parameters from impedance tube. (c) Real and imaginary part of the experimental Willis factor.

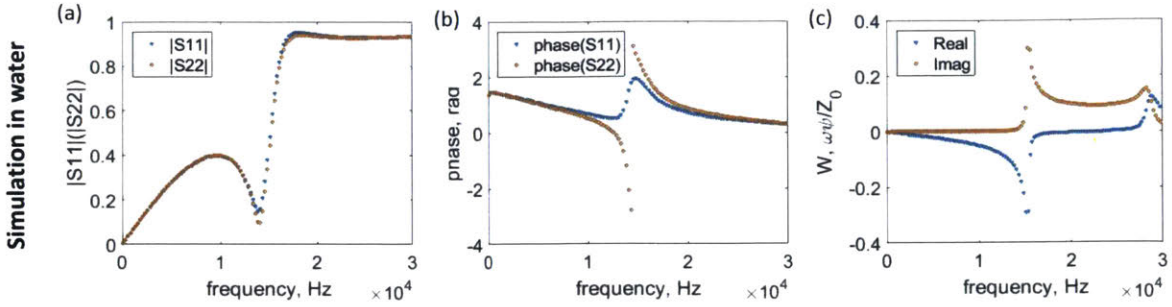

Figure C-6: Simulation and experimental results when the 3D printed Willis structure is put in water. (a-b) Amplitude (a) and phase (b) of the simulated S_{11} and S_{22} parameters. (c) Real and imaginary part of the simulated Willis factor.

Fig. C-4c-d) to measure the S parameters, and the Willis coupling factor is extracted using the same way as in the simulation.

The simulated and measured amplitudes and phases of S_{11} and S_{22} are plotted in Fig. C-5a-b (simulation) and Fig. C-5d-e (experiment). The corresponding Willis coupling factors are plotted in Fig. C-5c (simulation) and Fig. C-5f (experiment). the simulation and experimental results match very well. The asymmetric distribution of mass, compliance and damping in the cavity results in the amplitude and phase difference in S_{11} and S_{22}. The Willis coupling factor is the largest near the resonance frequency.

C.5 Discussion

The same structure can demonstrate Willis coupling both in water and in air. Fig. C-6 shows the simulation results when we put the same structure in water. Rigid boundary is assumed for the structure. Similar behavior is observed for S_{11} and S_{22} parameters as well as the Willis coupling factor. Because the sound speed in water is much larger than that in air, the frequencies shift to a higher range in underwater simulation compared to simulation in air. For future underwater experiments, the structure can be metal casted with aluminum, which has relatively large impedance mismatch with water.

Our structure has good rotating symmetry. If we rotate the direction of the two

narrow openings and the asymmetry of the cylinder location, we can change the Willis coupling direction. In the future, this direction can be explored to design tunable Willis coupling material for impedance matching, metasurface, cloaking, etc.

Appendix D

2D water/air patterns inside 1D hydrogel channels

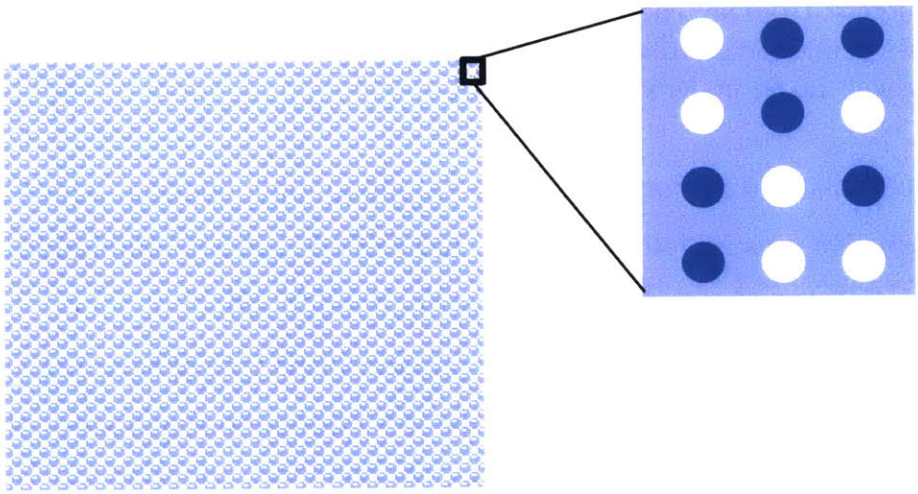

Figure D-1: Schematics for spatial sound modulator

There is a commonly used component in optics called spatial light modulator [156, 157, 158]. It is composed with micrometer-sized tunable unit cells that control light transmission intensity and phase, thus generates some form of spatially varying modulation on a beam of light. Spatial light modulators are widely applied to projectors, holograms, and other applications that need structured light illumination [159, 160, 161, 162]. In acoustics, there are also needs for generating structured

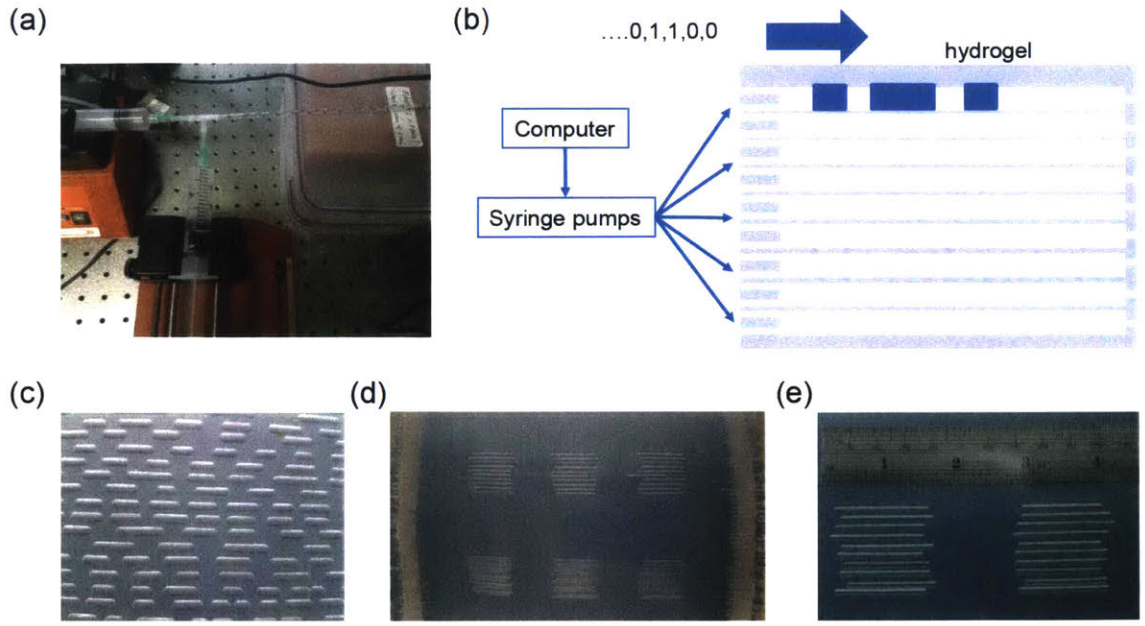

Figure D-2: Genertate 2D water/air patterns in 1D hydrogel channels. (a) Two syringe pumps controlled by computer that are used to inject air or water packets into the 1D channels. (b) The schematics for the method to generate preprogrammed water/air series inside the hydrogel channels. (c-e) Pictures of the 2d patterns generated inside hydrogel, taken underwater.

acoustic field distribution for applications in holographic imaging, acoustic levitation, compressive sensing, etc. However, most of the acoustic amplitude or phase modulators demonstrated so far are fixed structures [72, 73].

To fill this blank space in acoustics, we propose a new type of device called spatial sound modulator. The spatial sound modulator is based on the hydrogel with embedded 1D channels introduced in the previous chapter. The schematics of the spatial sound modulator is shown in Fig. D-1. It is composed on micro-structures or inclusions embedded in hydrogel matrix. The acoustic properties of the micro-structures or inclusions can be tuned individually.

In order to realize the proposed spatial sound modulator, we create 2D patterns inside the previously fabricated 1D channels embedded inside hydroge. We use two computer controlled syringe pumps (New Era NE1000) to fill programed series of water and air into each channel (Fig. D-2a-b). One of the syringe pump is loaded with syringe that is filled with water, and the other one is loaded with syringe filled

with air. The two syringe pumps operate alternatively at designed time period to generate the preprogrammed series of water and air. In side the hydrogel channels, the locations filled with water have transmission of 1, while the locations filled with air have transmission of 0.

Fig. D-1c-e show 2D patterns we have created. Currently, the resolution of 2D pattern is limited to centimeter. The pattern resolution can be increased by creating finer channel size and by optimizing the control of air and water flow inside the channels. This part can benefit from advanced manufacturing techniques for hydrogel and the flow control techniques in microfluidics.

Bibliography

[1] Engineering Toolbox. https://www.engineeringtoolbox.com/.

[2] Lawrence E Kinsler, Austin R Frey, Alan B Coppens, and James V Sanders. Fundamentals of acoustics. *Fundamentals of Acoustics, 4th Edition, by Lawrence E. Kinsler, Austin R. Frey, Alan B. Coppens, James V. Sanders, pp. 560. ISBN 0-471-84789-5. Wiley-VCH, December 1999.*, page 560, 1999.

[3] Andrew Webb and George C Kagadis. Introduction to biomedical imaging. *Medical Physics*, 30(8):2267–2267, 2003.

[4] Peter NT Wells. Ultrasonic imaging of the human body. *Reports on progress in physics*, 62(5):671, 1999.

[5] GS Cargill III. Ultrasonic imaging in scanning electron microscopy. *Nature*, 286(5774):691, 1980.

[6] Aaron Fenster, Donal B Downey, and H Neale Cardinal. Three-dimensional ultrasound imaging. *Physics in medicine & biology*, 46(5):R67, 2001.

[7] W Terence Coakley, David W Bardsley, Martin A Grundy, Freidoun Zamani, and David J Clarke. Cell manipulation in ultrasonic standing wave fields. *Journal of Chemical Technology & Biotechnology*, 44(1):43–62, 1989.

[8] Albrecht Haake, Adrian Neild, Deok-Ho Kim, Jong-Eun Ihm, Yu Sun, Jürg Dual, and Byeong-Kwon Ju. Manipulation of cells using an ultrasonic pressure field. *Ultrasound in medicine & biology*, 31(6):857–864, 2005.

[9] T Douglas Mast, Inder Raj S Makin, Waseem Faidi, Megan M Runk, Peter G Barthe, and Michael H Slayton. Bulk ablation of soft tissue with intense ultrasound: Modeling and experiments. *The Journal of the Acoustical Society of America*, 118(4):2715–2724, 2005.

[10] Brendan J O'Daly, Edmund Morris, Graham P Gavin, John M O'Byrne, and Garrett B McGuinness. High-power low-frequency ultrasound: A review of tissue dissection and ablation in medicine and surgery. *Journal of materials processing technology*, 200(1-3):38–58, 2008.

[11] Peter M Corry, Barthel Barlogie, Eugene J Tilchen, and Elwood P Armour. Ultrasound-induced hyperthermia for the treatment of human superficial tumors. *International Journal of Radiation Oncology* Biology* Physics*, 8(7):1225–1229, 1982.

[12] Samir Mitragotri. Healing sound: the use of ultrasound in drug delivery and other therapeutic applications. *Nature reviews Drug discovery*, 4(3):255, 2005.

[13] Michael D Menz, Ömer Oralkan, Pierre T Khuri-Yakub, and Stephen A Baccus. Precise neural stimulation in the retina using focused ultrasound. *Journal of Neuroscience*, 33(10):4550–4560, 2013.

[14] Alexander Bertrand. Applications and trends in wireless acoustic sensor networks: A signal processing perspective. In *2011 18th IEEE symposium on communications and vehicular technology in the Benelux (SCVT)*, pages 1–6. IEEE, 2011.

[15] Ian F Akyildiz, Dario Pompili, and Tommaso Melodia. Underwater acoustic sensor networks: research challenges. *Ad hoc networks*, 3(3):257–279, 2005.

[16] Hao Ge, Ming-Hui Lu, Yan-Feng Chen, Min Yang, Ping Sheng, Chu Ma, and Nicholas Fang. Breaking the barriers: advances in acoustic functional materials. *National Science Review*, 5(2):159–182, 12 2017.

[17] Steven A Cummer, Johan Christensen, and Andrea Alù. Controlling sound with acoustic metamaterials. *Nature Reviews Materials*, 1(3):16001, 2016.

[18] Guancong Ma and Ping Sheng. Acoustic metamaterials: From local resonances to broad horizons. *Science advances*, 2(2):e1501595, 2016.

[19] Zi Jing Wong, Yuan Wang, Kevin O'Brien, Junsuk Rho, Xiaobo Yin, Shuang Zhang, Nicholas Fang, Ta-Jen Yen, and Xiang Zhang. Optical and acoustic metamaterials: superlens, negative refractive index and invisibility cloak. *Journal of Optics*, 19(8):084007, 2017.

[20] Ming-Hui Lu, Liang Feng, and Yan-Feng Chen. Phononic crystals and acoustic metamaterials. *Materials today*, 12(12):34–42, 2009.

[21] Zhengyou Liu, Xixiang Zhang, Yiwei Mao, YY Zhu, Zhiyu Yang, Che Ting Chan, and Ping Sheng. Locally resonant sonic materials. *science*, 289(5485):1734–1736, 2000.

[22] Zhengyou Liu, Che Ting Chan, and Ping Sheng. Analytic model of phononic crystals with local resonances. *Physical Review B*, 71(1):014103, 2005.

[23] Sam Hyeon Lee, Choon Mahn Park, Yong Mun Seo, Zhi Guo Wang, and Chul Koo Kim. Acoustic metamaterial with negative density. *Physics letters A*, 373(48):4464–4469, 2009.

[24] Ni Sui, Xiang Yan, Tai-Yun Huang, Jun Xu, Fuh-Gwo Yuan, and Yun Jing. A lightweight yet sound-proof honeycomb acoustic metamaterial. *Applied Physics Letters*, 106(17):171905, 2015.

[25] Jensen Li and Che Ting Chan. Double-negative acoustic metamaterial. *Physical Review E*, 70(5):055602, 2004.

[26] Nicholas Fang, Dongjuan Xi, Jianyi Xu, Muralidhar Ambati, Werayut Srituravanich, Cheng Sun, and Xiang Zhang. Ultrasonic metamaterials with negative modulus. *Nature materials*, 5(6):452, 2006.

[27] Sam Hyeon Lee, Choon Mahn Park, Yong Mun Seo, Zhi Guo Wang, and Chul Koo Kim. Composite acoustic medium with simultaneously negative density and modulus. *Physical review letters*, 104(5):054301, 2010.

[28] Thomas Brunet, Aurore Merlin, Benoit Mascaro, Kevin Zimny, Jacques Leng, Olivier Poncelet, Christophe Aristégui, and Olivier Mondain-Monval. Soft 3d acoustic metamaterial with negative index. *Nature materials*, 14(4):384, 2015.

[29] Min Yang, Guancong Ma, Zhiyu Yang, and Ping Sheng. Coupled membranes with doubly negative mass density and bulk modulus. *Physical review letters*, 110(13):134301, 2013.

[30] Yangbo Xie, Bogdan-Ioan Popa, Lucian Zigoneanu, and Steven A Cummer. Measurement of a broadband negative index with space-coiling acoustic metamaterials. *Physical review letters*, 110(17):175501, 2013.

[31] Yong Li, Bin Liang, Zhong-ming Gu, Xin-ye Zou, and Jian-chun Cheng. Reflected wavefront manipulation based on ultrathin planar acoustic metasurfaces. *Scientific reports*, 3:2546, 2013.

[32] Yong Li, Xue Jiang, Rui-qi Li, Bin Liang, Xin-ye Zou, Lei-lei Yin, and Jian-chun Cheng. Experimental realization of full control of reflected waves with subwavelength acoustic metasurfaces. *Physical Review Applied*, 2(6):064002, 2014.

[33] Yangbo Xie, Wenqi Wang, Huanyang Chen, Adam Konneker, Bogdan-Ioan Popa, and Steven A Cummer. Wavefront modulation and subwavelength diffractive acoustics with an acoustic metasurface. *Nature communications*, 5:5553, 2014.

[34] Guancong Ma, Min Yang, Songwen Xiao, Zhiyu Yang, and Ping Sheng. Acoustic metasurface with hybrid resonances. *Nature materials*, 13(9):873, 2014.

[35] Y Cheng, C Zhou, BG Yuan, DJ Wu, Q Wei, and XJ Liu. Ultra-sparse metasurface for high reflection of low-frequency sound based on artificial mie resonances. *Nature materials*, 14(10):1013, 2015.

[36] Yong Li, Chen Shen, Yangbo Xie, Junfei Li, Wenqi Wang, Steven A Cummer, and Yun Jing. Tunable asymmetric transmission via lossy acoustic metasurfaces. *Physical review letters*, 119(3):035501, 2017.

[37] Boyang Xie, Kun Tang, Hua Cheng, Zhengyou Liu, Shuqi Chen, and Jianguo Tian. Coding acoustic metasurfaces. *Advanced Materials*, 29(6):1603507, 2017.

[38] John Brian Pendry. Negative refraction makes a perfect lens. *Physical review letters*, 85(18):3966, 2000.

[39] Xiang Zhang and Zhaowei Liu. Superlenses to overcome the diffraction limit. *Nature materials*, 7(6):435, 2008.

[40] Shu Zhang, Leilei Yin, and Nicholas Fang. Focusing ultrasound with an acoustic metamaterial network. *Physical review letters*, 102(19):194301, 2009.

[41] Nadège Kaina, Fabrice Lemoult, Mathias Fink, and Geoffroy Lerosey. Negative refractive index and acoustic superlens from multiple scattering in single negative metamaterials. *Nature*, 525(7567):77, 2015.

[42] Jong Jin Park, Choon Mahn Park, KJB Lee, and Sam H Lee. Acoustic superlens using membrane-based metamaterials. *Applied Physics Letters*, 106(5):051901, 2015.

[43] Muralidhar Ambati, Nicholas Fang, Cheng Sun, and Xiang Zhang. Surface resonant states and superlensing in acoustic metamaterials. *Physical Review B*, 75(19):195447, 2007.

[44] Choon Mahn Park, Jong Jin Park, Seung Hwan Lee, Yong Mun Seo, Chul Koo Kim, and Sam H Lee. Amplification of acoustic evanescent waves using metamaterial slabs. *Physical review letters*, 107(19):194301, 2011.

[45] Jie Zhu, Johan Christensen, Jesper Jung, Luis Martin-Moreno, X Yin, Lee Fok, Xiang Zhang, and FJ Garcia-Vidal. A holey-structured metamaterial for acoustic deep-subwavelength imaging. *Nature physics*, 7(1):52, 2011.

[46] Miguel Molerón and Chiara Daraio. Acoustic metamaterial for subwavelength edge detection. *Nature communications*, 6:8037, 2015.

[47] Jensen Li, Lee Fok, Xiaobo Yin, Guy Bartal, and Xiang Zhang. Experimental demonstration of an acoustic magnifying hyperlens. *Nature materials*, 8(12):931, 2009.

[48] Victor M García-Chocano, Johan Christensen, and José Sánchez-Dehesa. Negative refraction and energy funneling by hyperbolic materials: An experimental demonstration in acoustics. *Physical review letters*, 112(14):144301, 2014.

[49] Chen Shen, Yangbo Xie, Ni Sui, Wenqi Wang, Steven A Cummer, and Yun Jing. Broadband acoustic hyperbolic metamaterial. *Physical review letters*, 115(25):254301, 2015.

[50] Fabrice Lemoult, Mathias Fink, and Geoffroy Lerosey. Acoustic resonators for far-field control of sound on a subwavelength scale. *Physical Review Letters*, 107(6):064301, 2011.

[51] Yangbo Xie, Adam Konneker, Bogdan-Ioan Popa, and Steven A Cummer. Tapered labyrinthine acoustic metamaterials for broadband impedance matching. *Applied Physics Letters*, 103(20):201906, 2013.

[52] G D'Aguanno, KQ Le, R Trimm, A Alu, N Mattiucci, AD Mathias, N Aközbek, and MJ Bloemer. Broadband metamaterial for nonresonant matching of acoustic waves. *Scientific reports*, 2:340, 2012.

[53] Eun Bok, Jong Jin Park, Haejin Choi, Chung Kyu Han, Oliver B Wright, and Sam H Lee. Metasurface for water-to-air sound transmission. *Physical review letters*, 120(4):044302, 2018.

[54] Huanyang Chen and Che Ting Chan. Acoustic cloaking and transformation acoustics. *Journal of Physics D: Applied Physics*, 43(11):113001, 2010.

[55] Shu Zhang, Chunguang Xia, and Nicholas Fang. Broadband acoustic cloak for ultrasound waves. *Physical Review Letters*, 106(2):024301, 2011.

[56] Jun Mei, Guancong Ma, Min Yang, Zhiyu Yang, Weijia Wen, and Ping Sheng. Dark acoustic metamaterials as super absorbers for low-frequency sound. *Nature communications*, 3:756, 2012.

[57] Min Yang, Shuyu Chen, Caixing Fu, and Ping Sheng. Optimal sound-absorbing structures. *Materials Horizons*, 4(4):673–680, 2017.

[58] Min Yang, Chong Meng, Caixing Fu, Yong Li, Zhiyu Yang, and Ping Sheng. Subwavelength total acoustic absorption with degenerate resonators. *Applied Physics Letters*, 107(10):104104, 2015.

[59] Xuefeng Zhu, Hamidreza Ramezani, Chengzhi Shi, Jie Zhu, and Xiang Zhang. P t-symmetric acoustics. *Physical Review X*, 4(3):031042, 2014.

[60] Chengzhi Shi, Marc Dubois, Yun Chen, Lei Cheng, Hamidreza Ramezani, Yuan Wang, and Xiang Zhang. Accessing the exceptional points of parity-time symmetric acoustics. *Nature communications*, 7:11110, 2016.

[61] Romain Fleury, Dimitrios Sounas, and Andrea Alu. An invisible acoustic sensor based on parity-time symmetry. *Nature communications*, 6:5905, 2015.

[62] Carl Pfeiffer and Anthony Grbic. Metamaterial huygens' surfaces: tailoring wave fronts with reflectionless sheets. *Physical review letters*, 110(19):197401, 2013.

[63] Peng Zhang, Tongcang Li, Jie Zhu, Xuefeng Zhu, Sui Yang, Yuan Wang, Xiaobo Yin, and Xiang Zhang. Generation of acoustic self-bending and bottle beams by phase engineering. *Nature communications*, 5:4316, 2014.

[64] Chengzhi Shi, Marc Dubois, Yuan Wang, and Xiang Zhang. High-speed acoustic communication by multiplexing orbital angular momentum. *Proceedings of the National Academy of Sciences*, 114(28):7250–7253, 2017.

[65] Asier Marzo, Sue Ann Seah, Bruce W Drinkwater, Deepak Ranjan Sahoo, Benjamin Long, and Sriram Subramanian. Holographic acoustic elements for manipulation of levitated objects. *Nature communications*, 6:8661, 2015.

[66] Zixian Liang and Jensen Li. Extreme acoustic metamaterial by coiling up space. *Physical review letters*, 108(11):114301, 2012.

[67] Yong Li, Xue Jiang, Bin Liang, Jian-chun Cheng, and Likun Zhang. Metascreen-based acoustic passive phased array. *Physical Review Applied*, 4(2):024003, 2015.

[68] Xue Jiang, Yong Li, Bin Liang, Jian-chun Cheng, and Likun Zhang. Convert acoustic resonances to orbital angular momentum. *Physical review letters*, 117(3):034301, 2016.

[69] Yifan Zhu, Jie Hu, Xudong Fan, Jing Yang, Bin Liang, Xuefeng Zhu, and Jianchun Cheng. Fine manipulation of sound via lossy metamaterials with independent and arbitrary reflection amplitude and phase. *Nature communications*, 9(1):1632, 2018.

[70] Junfei Li, Chen Shen, Ana Díaz-Rubio, Sergei A Tretyakov, and Steven A Cummer. Systematic design and experimental demonstration of bianisotropic metasurfaces for scattering-free manipulation of acoustic wavefronts. *Nature communications*, 9(1):1342, 2018.

[71] Kun Tang, Chunyin Qiu, Manzhu Ke, Jiuyang Lu, Yangtao Ye, and Zhengyou Liu. Anomalous refraction of airborne sound through ultrathin metasurfaces. *Scientific reports*, 4:6517, 2014.

[72] Kai Melde, Andrew G Mark, Tian Qiu, and Peer Fischer. Holograms for acoustics. *Nature*, 537(7621):518, 2016.

[73] Yangbo Xie, Chen Shen, Wenqi Wang, Junfei Li, Dingjie Suo, Bogdan-Ioan Popa, Yun Jing, and Steven A Cummer. Acoustic holographic rendering with two-dimensional metamaterial-based passive phased array. *Scientific reports*, 6:35437, 2016.

[74] Ernst Abbe. Beiträge zur theorie des mikroskops und der mikroskopischen wahrnehmung. *Archiv für mikroskopische Anatomie*, 9(1):413–418, 1873.

[75] P Günther, U Ch Fischer, and K Dransfeld. Scanning near-field acoustic microscopy. *Applied Physics B*, 48(1):89–92, 1989.

[76] Geoffroy Lerosey, Julien De Rosny, Arnaud Tourin, and Mathias Fink. Focusing beyond the diffraction limit with far-field time reversal. *Science*, 315(5815):1120–1122, 2007.

[77] Julien de Rosny and Mathias Fink. Overcoming the diffraction limit in wave physics using a time-reversal mirror and a novel acoustic sink. *Physical review letters*, 89(12):124301, 2002.

[78] Chu Ma, Seok Kim, and Nicholas X Fang. Far-field acoustic subwavelength imaging and edge detection based on spatial filtering and wave vector conversion. *Nature communications*, 10(1):204, 2019.

[79] Nikolay I Zheludev and Yuri S Kivshar. From metamaterials to metadevices. *Nature materials*, 11(11):917, 2012.

[80] Hou-Tong Chen, Antoinette J Taylor, and Nanfang Yu. A review of metasurfaces: physics and applications. *Reports on Progress in Physics*, 79(7):076401, 2016.

[81] Stanislav B Glybovski, Sergei A Tretyakov, Pavel A Belov, Yuri S Kivshar, and Constantin R Simovski. Metasurfaces: From microwaves to visible. *Physics Reports*, 634:1–72, 2016.

[82] Shulin Sun, Qiong He, Shiyi Xiao, Qin Xu, Xin Li, and Lei Zhou. Gradient-index meta-surfaces as a bridge linking propagating waves and surface waves. *Nature materials*, 11(5):426, 2012.

[83] Nanfang Yu, Patrice Genevet, Mikhail A Kats, Francesco Aieta, Jean-Philippe Tetienne, Federico Capasso, and Zeno Gaburro. Light propagation with phase discontinuities: generalized laws of reflection and refraction. *science*, page 1210713, 2011.

[84] Alexander V Kildishev, Alexandra Boltasseva, and Vladimir M Shalaev. Planar photonics with metasurfaces. *Science*, 339(6125):1232009, 2013.

[85] Xuefeng Zhu, Kun Li, Peng Zhang, Jie Zhu, Jintao Zhang, Chao Tian, and Shengchun Liu. Implementation of dispersion-free slow acoustic wave propagation and phase engineering with helical-structured metamaterials. *Nature communications*, 7:11731, 2016.

[86] Jiajun Zhao, Baowen Li, Zhining Chen, and Cheng-Wei Qiu. Manipulating acoustic wavefront by inhomogeneous impedance and steerable extraordinary reflection. *Scientific reports*, 3:2537, 2013.

[87] Wenqi Wang, Yangbo Xie, Bogdan-Ioan Popa, and Steven A Cummer. Subwavelength diffractive acoustics and wavefront manipulation with a reflective acoustic metasurface. *Journal of Applied Physics*, 120(19):195103, 2016.

[88] Junfei Li, Wenqi Wang, Yangbo Xie, Bogdan-Ioan Popa, and Steven A Cummer. A sound absorbing metasurface with coupled resonators. *Applied Physics Letters*, 109(9):091908, 2016.

[89] Jing Zhang, Zhong Lei Mei, Wan Ru Zhang, Fan Yang, and Tie Jun Cui. An ultrathin directional carpet cloak based on generalized snell's law. *Applied Physics Letters*, 103(15):151115, 2013.

[90] Hussein Esfahlani, Sami Karkar, Herve Lissek, and Juan R Mosig. Acoustic carpet cloak based on an ultrathin metasurface. *Physical Review B*, 94(1):014302, 2016.

[91] Donald C O'Shea, Thomas J Suleski, Alan D Kathman, and Dennis W Prather. *Diffractive optics: design, fabrication, and test*, volume 62. Spie Press Bellingham, WA, 2004.

[92] Alex MH Wong and George V Eleftheriades. Perfect anomalous reflection with a bipartite huygens' metasurface. *Physical Review X*, 8(1):011036, 2018.

[93] JL Ramos Quirarte and J Piotr Starski. Novel schiffman phase shifters. *IEEE transactions on microwave theory and techniques*, 41(1):9–14, 1993.

[94] Yong-Xin Guo, Zhen-Yu Zhang, and Ling Chuen Ong. Improved wide-band schiffman phase shifter. *IEEE Transactions on Microwave Theory and Techniques*, 54(3):1196–1200, 2006.

[95] Z. Zhang, Y. C. Jiao, S. F. Cao, X. M. Wang, and F. S. Zhang. Modified broadband schiffman phase shifter using dentate microstrip and patterned ground plane. *Progress In Electromagnetics Research*, 24:9–16, 2011.

[96] Leo L. Beranek. *Acoustics*. New York: Acoust. Soc. Am, 1954.

[97] Johan Christensen, Luis Martin-Moreno, and Francisco Jose Garcia-Vidal. Theory of resonant acoustic transmission through subwavelength apertures. *Physical review letters*, 101(1):014301, 2008.

[98] Allard P Mosk, Ad Lagendijk, Geoffroy Lerosey, and Mathias Fink. Controlling waves in space and time for imaging and focusing in complex media. *Nature photonics*, 6(5):283, 2012.

[99] Xiaoshi Su, Andrew N Norris, Colby W Cushing, Michael R Haberman, and Preston S Wilson. Broadband focusing of underwater sound using a transparent pentamode lens. *The Journal of the Acoustical Society of America*, 141(6):4408–4417, 2017.

[100] Alexey S Titovich, Andrew N Norris, and Michael R Haberman. A high transmission broadband gradient index lens using elastic shell acoustic metamaterial elements. *The Journal of the Acoustical Society of America*, 139(6):3357–3364, 2016.

[101] Yi Chen, Mingye Zheng, Xiaoning Liu, Yafeng Bi, Zhaoyong Sun, Ping Xiang, Jun Yang, and Gengkai Hu. Broadband solid cloak for underwater acoustics. *Physical Review B*, 95(18):180104, 2017.

[102] Heng Jiang, Yuren Wang, Milin Zhang, Yanping Hu, Ding Lan, Yinmin Zhang, and Bingchen Wei. Locally resonant phononic woodpile: A wide band anomalous underwater acoustic absorbing material. *Applied Physics Letters*, 95(10):104101, 2009.

[103] Christina J Naify, Theodore P Martin, Christopher N Layman, Michael Nicholas, Abel L Thangawng, David C Calvo, and Gregory J Orris. Underwater acoustic omnidirectional absorber. *Applied Physics Letters*, 104(7):073505, 2014.

[104] Claudia Errico, Juliette Pierre, Sophie Pezet, Yann Desailly, Zsolt Lenkei, Olivier Couture, and Mickael Tanter. Ultrafast ultrasound localization microscopy for deep super-resolution vascular imaging. *Nature*, 527(7579):499, 2015.

[105] Lihong V Wang and Song Hu. Photoacoustic tomography: in vivo imaging from organelles to organs. *science*, 335(6075):1458–1462, 2012.

[106] Xavier Lurton. *An introduction to underwater acoustics: principles and applications*. Springer Science & Business Media, 2002.

[107] L Airoldi and M Ruzzene. Design of tunable acoustic metamaterials through periodic arrays of resonant shunted piezos. *New Journal of Physics*, 13(11):113010, 2011.

[108] Bogdan-Ioan Popa and Steven A Cummer. Non-reciprocal and highly nonlinear active acoustic metamaterials. *Nature communications*, 5:3398, 2014.

[109] Ziwei Wang, Quan Zhang, Kai Zhang, and Gengkai Hu. Tunable digital metamaterial for broadband vibration isolation at low frequency. *Advanced materials*, 28(44):9857–9861, 2016.

[110] Filippo Casadei, Tommaso Delpero, Andrea Bergamini, Paolo Ermanni, and Massimo Ruzzene. Piezoelectric resonator arrays for tunable acoustic waveguides and metamaterials. *Journal of Applied Physics*, 112(6):064902, 2012.

[111] Pai Wang, Filippo Casadei, Sicong Shan, James C Weaver, and Katia Bertoldi. Harnessing buckling to design tunable locally resonant acoustic metamaterials. *Physical review letters*, 113(1):014301, 2014.

[112] Sahab Babaee, Johannes TB Overvelde, Elizabeth R Chen, Vincent Tournat, and Katia Bertoldi. Reconfigurable origami-inspired acoustic waveguides. *Science Advances*, 2(11):e1601019, 2016.

[113] Hyunwoo Yuk, Shaoting Lin, Chu Ma, Mahdi Takaffoli, Nicolas X Fang, and Xuanhe Zhao. Hydraulic hydrogel actuators and robots optically and sonically camouflaged in water. *Nature communications*, 8:14230, 2017.

[114] Jian Ping Gong, Yoshinori Katsuyama, Takayuki Kurokawa, and Yoshihito Osada. Double-network hydrogels with extremely high mechanical strength. *Advanced materials*, 15(14):1155–1158, 2003.

[115] Jeong-Yun Sun, Xuanhe Zhao, Widusha RK Illeperuma, Ovijit Chaudhuri, Kyu Hwan Oh, David J Mooney, Joost J Vlassak, and Zhigang Suo. Highly stretchable and tough hydrogels. *Nature*, 489(7414):133, 2012.

[116] Xuanhe Zhao. Multi-scale multi-mechanism design of tough hydrogels: building dissipation into stretchy networks. *Soft Matter*, 10(5):672–687, 2014.

[117] M Kafesaki and Eleftherios N Economou. Multiple-scattering theory for three-dimensional periodic acoustic composites. *Physical review B*, 60(17):11993, 1999.

[118] Malcolm J Crocker. *Handbook of acoustics*. John Wiley & Sons, 1998.

[119] Vladimir Fokin, Muralidhar Ambati, Cheng Sun, and Xiang Zhang. Method for retrieving effective properties of locally resonant acoustic metamaterials. *Physical review B*, 76(14):144302, 2007.

[120] Daniel Torrent and José Sánchez-Dehesa. Effective parameters of clusters of cylinders embedded in a nonviscous fluid or gas. *Physical Review B*, 74(22):224305, 2006.

[121] Teng Zhang, Shaoting Lin, Hyunwoo Yuk, and Xuanhe Zhao. Predicting fracture energies and crack-tip fields of soft tough materials. *Extreme Mechanics Letters*, 4:1–8, 2015.

[122] S Ayrinhac, M Gauthier, G Le Marchand, M Morand, F Bergame, and F Decremps. Thermodynamic properties of liquid gallium from picosecond acoustic velocity measurements. *Journal of Physics: Condensed Matter*, 27(27):275103, 2015.

[123] Jack Blitz and Geoff Simpson. *Ultrasonic methods of non-destructive testing*, volume 2. Springer Science & Business Media, 1995.

[124] Jerry L Sutton. Underwater acoustic imaging. *Proceedings of the IEEE*, 67(4):554–566, 1979.

[125] Woon Siong Gan. *Acoustical Imaging: Techniques and Applications for Engineers*. John Wiley & Sons, 2012.

[126] D Rugar. Resolution beyond the diffraction limit in the acoustic microscope: A nonlinear effect. *Journal of applied physics*, 56(5):1338–1346, 1984.

[127] Donald B Conkey, Antonio M Caravaca-Aguirre, Jake D Dove, Hengyi Ju, Todd W Murray, and Rafael Piestun. Super-resolution photoacoustic imaging through a scattering wall. *Nature communications*, 6:7902, 2015.

[128] Stéphane Durant, Zhaowei Liu, Jennifer M Steele, and Xiang Zhang. Theory of the transmission properties of an optical far-field superlens for imaging beyond the diffraction limit. *JOSA B*, 23(11):2383–2392, 2006.

[129] Zhaowei Liu, Stéphane Durant, Hyesog Lee, Yuri Pikus, Nicolas Fang, Yi Xiong, Cheng Sun, and Xiang Zhang. Far-field optical superlens. *Nano Letters*, 7(2):403–408, 2007.

[130] Joseph Goodman. Introduction to fourier optics. 2008.

[131] Markus Gudmundsson, Essam A El-Kwae, and Mansur R Kabuka. Edge detection in medical images using a genetic algorithm. *IEEE transactions on medical imaging*, 17(3):469–474, 1998.

[132] Julian Guerrero, Septimiu E Salcudean, James A McEwen, Bassam A Masri, and Savvakis Nicolaou. Real-time vessel segmentation and tracking for ultrasound imaging applications. *IEEE transactions on medical imaging*, 26(8):1079–1090, 2007.

[133] MAGDALENA Rucka and KRZYSZTOF Wilde. Application of continuous wavelet transform in vibration based damage detection method for beams and plates. *Journal of Sound and Vibration*, 297(3-5):536–550, 2006.

[134] Sunil K Sinha and Paul W Fieguth. Automated detection of cracks in buried concrete pipe images. *Automation in Construction*, 15(1):58–72, 2006.

[135] Pablo Arbelaez, Michael Maire, Charless Fowlkes, and Jitendra Malik. Contour detection and hierarchical image segmentation. *IEEE transactions on pattern analysis and machine intelligence*, 33(5):898–916, 2011.

[136] Xiangdong Zhang and Zhengyou Liu. Negative refraction of acoustic waves in two-dimensional phononic crystals. *Applied Physics Letters*, 85(2):341–343, 2004.

[137] Suxia Yang, John H Page, Zhengyou Liu, Michael L Cowan, Che Ting Chan, and Ping Sheng. Focusing of sound in a 3d phononic crystal. *Physical review letters*, 93(2):024301, 2004.

[138] K Imamura and S Tamura. Negative refraction of phonons and acoustic lensing effect of a crystalline slab. *Physical Review B*, 70(17):174308, 2004.

[139] Chunyin Qiu, Xiangdong Zhang, and Zhengyou Liu. Far-field imaging of acoustic waves by a two-dimensional sonic crystal. *Physical Review B*, 71(5):054302, 2005.

[140] Liang Feng, Xiao-Ping Liu, Yan-Bin Chen, Zhi-Peng Huang, Yi-Wei Mao, Yan-Feng Chen, Jian Zi, and Yong-Yuan Zhu. Negative refraction of acoustic waves in two-dimensional sonic crystals. *Physical Review B*, 72(3):033108, 2005.

[141] Liang Feng, Xiao-Ping Liu, Ming-Hui Lu, Yan-Bin Chen, Yan-Feng Chen, Yi-Wei Mao, Jian Zi, Yong-Yuan Zhu, Shi-Ning Zhu, and Nai-Ben Ming. Acoustic backward-wave negative refractions in the second band of a sonic crystal. *Physical review letters*, 96(1):014301, 2006.

[142] Ming-Hui Lu, Chao Zhang, Liang Feng, Jun Zhao, Yan-Feng Chen, Yi-Wei Mao, Jian Zi, Yong-Yuan Zhu, Shi-Ning Zhu, and Nai-Ben Ming. Negative birefraction of acoustic waves in a sonic crystal. *Nature materials*, 6(10):744, 2007.

[143] Zhiyu Yang, Jun Mei, Min Yang, NH Chan, and Ping Sheng. Membrane-type acoustic metamaterial with negative dynamic mass. *Physical review letters*, 101(20):204301, 2008.

[144] Dylan Lu and Zhaowei Liu. Hyperlenses and metalenses for far-field super-resolution imaging. *Nature communications*, 3:1205, 2012.

[145] Johan Christensen and Francisco Javier García de Abajo. Acoustic field enhancement and subwavelength imaging by coupling to slab waveguide modes. *Applied Physics Letters*, 97(16):164103, 2010.

[146] Matthew D Shaw. On the measurement of angular dependent sound transmission through airborne supercritical plates. 2011.

[147] Reza Ghaffarivardavagh, Jacob Nikolajczyk, Stephan Anderson, and Xin Zhang. Ultra-open acoustic metamaterial silencer based on fano-like interference. *Physical Review B*, 99(2):024302, 2019.

[148] Andrea Alu, Giuseppe D'Aguanno, Nadia Mattiucci, and Mark J Bloemer. Plasmonic brewster angle: broadband extraordinary transmission through optical gratings. *Physical review letters*, 106(12):123902, 2011.

[149] N Aközbek, N Mattiucci, D De Ceglia, R Trimm, A Alù, G D'Aguanno, MA Vincenti, M Scalora, and MJ Bloemer. Experimental demonstration of plasmonic brewster angle extraordinary transmission through extreme subwavelength slit arrays in the microwave. *Physical Review B*, 85(20):205430, 2012.

[150] Yichen Shen, Dexin Ye, Ivan Celanovic, Steven G Johnson, John D Joannopoulos, and Marin Soljačić. Optical broadband angular selectivity. *Science*, 343(6178):1499–1501, 2014.

[151] PL Tyack. Acoustic communication under the sea. In *Animal acoustic communication*, pages 163–220. Springer, 1998.

[152] Thomas L Szabo. *Diagnostic ultrasound imaging: inside out.* Academic Press, 2004.

[153] Caleb F Sieck, Andrea Alù, and Michael R Haberman. Origins of willis coupling and acoustic bianisotropy in acoustic metamaterials through source-driven homogenization. *Physical Review B*, 96(10):104303, 2017.

[154] Sukmo Koo, Choonlae Cho, Jun-ho Jeong, and Namkyoo Park. Acoustic omni meta-atom for decoupled access to all octants of a wave parameter space. *Nature communications*, 7:13012, 2016.

[155] Michael B Muhlestein, Caleb F Sieck, Preston S Wilson, and Michael R Haberman. Experimental evidence of willis coupling in a one-dimensional effective material element. *Nature communications*, 8:15625, 2017.

[156] Demetri Psaltis, Eung G Paek, and Santosh S Venkatesh. Optical image correlation with a binary spatial light modulator. *Optical engineering*, 23(6):236698, 1984.

[157] Uzi Efron. *Spatial light modulator technology: materials, devices, and applications*, volume 47. CRC press, 1994.

[158] Wai Lam Chan, Hou-Tong Chen, Antoinette J Taylor, Igal Brener, Michael J Cich, and Daniel M Mittleman. A spatial light modulator for terahertz beams. *Applied Physics Letters*, 94(21):213511, 2009.

[159] Fai Mok, Joseph Diep, Hua-Kuang Liu, and Demetri Psaltis. Real-time computer-generated hologram by means of liquid-crystal television spatial light modulator. *Optics Letters*, 11(11):748–750, 1986.

[160] Jennifer E Curtis, Brian A Koss, and David G Grier. Dynamic holographic optical tweezers. *Optics communications*, 207(1-6):169–175, 2002.

[161] Joonku Hahn, Hwi Kim, Yongjun Lim, Gilbae Park, and Byoungho Lee. Wide viewing angle dynamic holographic stereogram with a curved array of spatial light modulators. *Optics express*, 16(16):12372–12386, 2008.

[162] Maurice Stanley, Mark AG Smith, Allan P Smith, Philip J Watson, Stuart D Coomber, Colin D Cameron, Christopher W Slinger, and Andrew Wood. 3d electronic holography display system using a 100 mega-pixel spatial light modulator. In *Optical Design and Engineering*, volume 5249, pages 297–309. International Society for Optics and Photonics, 2004.